

Channelized Epishelf Lake Drainage Beneath the Milne Ice Shelf, Ellesmere Island,
Nunavut

By
Jill Sophia Thomas Rajewicz

A thesis submitted to the Faculty of Graduate and Postdoctoral Affairs in partial
fulfillment of the requirements for the degree of

Master of Science

In

Geography

Carleton University
Ottawa, Ontario

©2017, Jill Sophia Thomas Rajewicz

Abstract

A depression running across the outer Milne Ice Shelf was hypothesized to overlie a basal channel incised by outflow from the Milne Fiord epishelf lake, a thick layer of freshwater impounded in the fiord by the ice shelf. Ice thickness mapping using ice-penetrating radar revealed the presence of a channel with incision heights of 39 to 45 m (70-80% of mean ice shelf thickness), basal widths of 57-86 m, and mean sidewall slopes of $\sim 40^\circ$ upward from horizontal. Profiles of salinity, temperature and current speed with depth showed there was a fast flowing jet of epishelf lake water in the channel, with velocities up to 60 cm s^{-1} , confirming the channel is a drainage outlet for the epishelf lake. The presence of the channel represents a significant structural weakness along which future breakup of the ice shelf is likely to occur.

Acknowledgements

This thesis has benefitted from many kinds and sources of support, for which I am extremely grateful.

Support for this project was provided by a Natural Sciences and Engineering Research Council of Canada (NSERC) Alexander Graham Bell Canada Graduate Scholarship, a W. Garfield Weston Award for Northern Research from the Garfield Weston Foundation, the Ontario Graduate Scholarship from the Ontario Ministry of Training, Colleges and Universities and scholarships from Carleton University. Research funding also came from grants from the Northern Scientific Training Program, NSERC, the Polar Continental Shelf Project, the Canada Foundation for Innovation and ArcticNet.

I owe many, many, many thanks to my supervisor, Dr. Derek Mueller. Derek, thank you for your patience, guidance, excellent feedback, and sense of humour throughout this process. I am inspired by your endless curiosity about the world and passion for the work you do, and I have learned so much about how to do science from you. I am also very grateful for having had the tremendous opportunity to hone my skills as a field scientist in one of the most spectacular places on this planet, the northern coast of Ellesmere Island.

I also owe big thanks to Andrew Hamilton for all his help and advice over the last three years, not to mention tremendous field ingenuity!

I have had the pleasure of having many excellent field adventures and strange fieldwork meals with many folks over three field seasons: Kelly Graves, Sam Brenner, Adam Garbo, Kevin Xu and Greg Crocker, thank you for all your help and for the good times. Nat Wilson provided advice on ice penetrating radar data interpretation and analysis. Dr. Chris Burn, my committee member, has given me great advice and support throughout my whole degree and I appreciate his time and thoughtful comments. My colleagues in the Water and Ice Research Lab and in the Department of Geography and Environmental Studies and my wonderful community of friends have also been invaluable sources of wisdom and support, and have kept me sane and happy!

And last, but most definitely not least, my family have been the best cheerleaders a person could ask for. Your encouragement and belief in me buoys me and fortifies me. Thank you for your unflagging love and support, mom, dad, Craig, Lise and Grandma. Thank you also for inspiring in me a love of learning and a deep appreciation for the natural world.

Table of Contents

1	Introduction.....	1
1.1	Description of problem.....	1
1.2	Research objectives	8
1.3	Significance.....	8
1.4	Thesis structure	9
2	Literature Review.....	10
2.1	Ellesmere Island ice shelves.....	10
2.2	Epishelf lakes	11
2.3	Ice shelf change.....	13
2.4	Consequences of ice shelf breakup	16
2.5	Causes of ice shelf breakup.....	16
2.6	Basal channels.....	18
2.6.1	Basal channel formation	18
2.6.2	Channel morphology.....	20
2.6.3	Impacts of channelization	22
2.6.4	Detection and characterization of ice shelf basal channels.....	22
2.7	Ice penetrating radar.....	23
2.7.1	Physical principles of ice penetrating radar	23
2.7.2	Considerations for IPR data collection and analysis.....	28
3	Methods.....	31
3.1	Study area.....	31
3.2	Field campaign overview	34
3.3	Characterization of feature morphology	35
3.3.1	Ice thickness surveys.....	35
3.3.2	Data processing.....	40
3.3.3	Cross-sectional form characterization, measurement and analysis.....	42
3.4	Ice thickness error estimation.....	45
3.5	Hydrography.....	48
3.5.1	Conductivity-temperature-depth profiling	48
3.5.2	CTD profile data processing.....	50

3.5.3	Current velocities	50
3.5.4	Estimation of discharge.....	52
4	Results.....	55
4.1	Ice thickness survey overview.....	55
4.2	Channel morphology	59
4.3	Comparison of fracture and channel morphology.....	65
4.4	Additional ice thickness measurements	65
4.5	Characterization of snow cover.....	68
4.6	Hydrography.....	68
4.6.1	Temperature and salinity profiles	68
4.6.2	Current measurements	71
4.6.3	Estimation of discharge.....	74
5	Discussion.....	80
5.1	Morphological evidence for channelization.....	80
5.2	Controls on channel surface and basal morphology.....	81
5.3	Properties of flow through the channel	87
5.4	Discharge.....	91
5.5	Fracture hydrography and morphology.....	93
5.6	Sources of error	96
5.7	Implications of channelization for ice shelf stability	98
6	Conclusion	100
7	References.....	105
	Appendix A: Cross-sectional ice thickness profiles from IPR survey grids.....	116

List of Tables

Table 2.1 Typical values for the electrical properties of common earth materials. Adapted from Hubbard and Glasser (2005).	26
Table 3.1 Antenna frequencies and settings for ice penetrating radar surveys of the channel (grids A-D) and the fracture (grid E).....	39
Table 3.2 Summary statistics for a cross-point analysis conducted to assess picking error in IPR survey data.	46
Table 4.1 Total number of IPR traces recorded and number of traces where the ice-water reflector could be identified, by survey grid.	58
Table 4.2 Basal and surface morphology metrics calculated from all complete ice penetrating radar cross-sectional profiles across the channel (grids A to D) and fracture (grid E).....	61
Table 4.3 Ice thickness and ice draft measurements made through natural cracks and steam-drilled boreholes in the channel.	67
Table 4.4 Area, water velocity and discharge for each 1 m depth segment over the estimated depth of flow in the channel at site 1. Discharge is summed across all segments for total discharge.	77
Table 4.5 Area, water velocity and discharge for each 1 m depth segment over the estimated depth of flow in the channel at site 2. Discharge is summed across all segments for total discharge.	78

List of Figures

- Figure 1.1** Maps of the locations and historic and present-day extents of ice shelves in the Canadian Arctic. Ice shelves are found only along the northwestern coast of Ellesmere Island, in the Canadian Arctic Archipelago (red box, panel A). Panel B shows the ice shelf extent as of 2015 in black, and the red arrow indicates the Milne Ice Shelf, located at the mouth of Milne Fiord. Green shows the greater maximum ice shelf extent in 1959, when the ice shelves were first mapped. The approximate extent of the ~8900 km² ‘Ellesmere Ice Shelf’, reconstructed from observations in the late 1800s/early 1900s, is shown in blue. White areas are ocean or sea ice; dark grey indicates glaciated areas (Figure adapted from Mueller et al., 2017a). 2
- Figure 1.2** Schematics of an epishelf lake/ice shelf system (not drawn to scale) in plan view (A) and side view (B). The floating ice shelf dams terrestrial meltwater in the fiord, creating a density-stratified epishelf lake wherein freshwater floats on marine water. When the freshwater layer deepens beyond the minimum draft of the ice shelf, epishelf lake water flows out beneath the ice shelf to the Arctic Ocean. 4
- Figure 1.3** RADARSAT-2 Fine Quad image from July 2015 of the outer Milne Ice Shelf (A) showing the location of the E-W surface depression hypothesized to overlie a basal channel (red arrow). The blue arrow denotes a fracture formed in 2009 used in this study to compare morphology and hydrography of a channel and fracture. An older fracture that dates to at least 1950 can be seen intersecting the E-W depression. Panel B is a photo of the surface appearance of the fracture. Panel C shows the curvilinear E-W surface depression with longitudinal crevassing along the margins. Meltwater pools and snow can be seen in the depression, as well as in surrounding low spots on the ice shelf. An aerial photo shows the depression in plan view (D); the depression cross-cuts the characteristic rolling topography of the ice shelf. 6
- Figure 1.4** Map of modelled ice drafts for the Milne Ice Shelf and Milne Glacier tongue. The grey area is the epishelf lake with ice thicknesses ~1 m. The black line indicates the 35 m contour interval. Thin ice (<10 m) can be seen along the depression that runs E-W across the outer ice shelf, indicating it was a likely path for outflow from the epishelf lake. Adapted from Hamilton (2016). 7

Figure 2.1 Ice shelf basal melt and channelization driven by (A) a buoyant freshwater plume originating from sub-glacial discharge and basal melt of an ice shelf and (B) channelized outflow of warm epishelf lake beneath an ice shelf. For a thick ice shelf exposed to warm water, typical of ice shelves in the Antarctic and Greenland, meltwater is generated at depth and may be supplemented by fresh subglacial discharge across the grounding line. The buoyant freshwater rises along the sloped base of the ice shelf in a buoyant plume, entraining warm water from below. Heat supplied by entrained ocean water is used to melt the ice shelf base. In the Canadian Arctic, the source of heat to melt and incise ice shelves is the freshwater impounded by an ice shelf. Epishelf lakes stay above 0°C year round; outflow beneath an ice shelf occurs when the epishelf lake thickens beyond the minimum draft of the ice shelf. Adapted from Jenkins, 2011 (A) and Hamilton et al., 2017 (B). 19

Figure 2.2 Ice penetrating radar (IPR) set up: the transmitting antenna sends a pulse of electromagnetic energy into the ice. When the pulse hits a boundary between materials with different electrical properties, some of the transmitted energy is reflected back to the surface. Some of the energy is absorbed and some transmitted into the underlying substrate. The amplitude and two-way travel time of the reflected pulse is recorded by the receiver antenna. Two-way travel time can be converted to distance to the reflector, using the velocity of the radar wave in ice. 24

Figure 2.3 Configuration of a common-offset survey (A) and the resulting series of radar traces (B). Pulses are sent and received at regular intervals moving along the direction of travel. The associated traces show the amplitude and polarity of the transmitted pulse (airwave and ground wave combined) and the reflected pulse (bed wave). Red dashed lines indicate the location of the wavelet ‘first break’, which is the first increase in energy. Two-way travel time to the reflector is calculated using the position of the airwave first break and bed wave first break. Adapted from Cassidy (2009)..... 29

Figure 3.1 Map of Milne Fiord on the northern coast of Ellesmere Island, overlaid on an ASTER image from July 2016. The ice shelf is outlined in black, the epishelf lake is in orange and a portion of the floating tongue of the Milne Glacier is outlined in green. Triangles denote the locations of field camps occupied over the years of this study. The surface depression hypothesized to mark a basal channel is shown with a dashed red line.

A fracture formed between 2008 and 2009 is outlined with a solid blue line. The hydrography and morphology of the channel and fracture were compared in this study. Dark blue meltwater ponds can be seen between the rolls on the ice shelf. There are several other linear features on the outer ice shelf, including a rehealed fracture dating to at least 1950 that can be seen running N-S from Cape Egerton to intersect the hypothesized channel. 32

Figure 3.2 Panel A shows the field-ruggedized ice penetrating radar unit (IPR) used in this study. The transmitter and receiver were ski-mounted, in an in-line, common-offset survey configuration. The distance between antennae was adjusted as appropriate for the frequency used for a given survey. A Topcon Hiper V Dual-Frequency GPS receiver unit was mounted in front of the receiver and recorded precise horizontal positions and surface elevations along each transect. Panel B shows a survey in progress, with the front worker pulling the IPR unit and an additional person acting as a brake if required. 36

Figure 3.3 Ice penetrating radar survey grids along the channel (A, B, C and D) and the fracture (E). Each black line is an IPR transect line. Light green circles indicate the locations of ice thickness measurements taken in the channel or fracture through natural cracks or steam-drilled boreholes. Red dashed lines indicate the boundaries between survey grids. The left and right banks of the channel and fracture show the orientation of cross channel lines normalized to zero, where zero is the centerline of the feature. Locations to the left of the centerline have negative values for distance, while locations to the right of the feature centerline have positive distance values. 38

Figure 3.4 Schematics of an idealized channel ice thickness cross-section (A) and an idealized fracture ice thickness cross-section (B) showing the geometric variables measured in this study (not to scale). Slope breakpoints indicating the margins of the feature at the surface and at the ice shelf base are indicated by red dashed lines. For channel cross-sections, basal incision ('h'), basal and surface width ('w'), and the mean slope angle of each sidewall from horizontal (θ) was calculated. In addition, the thickness ('t') of the ice on the left and right banks was measured, as well as the minimum thickness of the ice at the crest of the channel. For each fracture cross-section, the fracture penetration depth ('d'), minimum thickness of ice within the fracture, width of the fracture, and slope of the sidewalls up from horizontal was measured. 44

Figure 3.5 Locations of hydrographic measurements in this study. Pink circles indicate conductivity-temperature-depth (CTD) profiles. CTD profiling was done every year of the study in the epishelf lake, as well as in three different locations offshore of the northern edge of the ice shelf. CTD profiling, as well as current measurements were done at two sites in the channel and at one site in the fracture. Site 1 was at the seaward edge of the channel; site 2 was further up channel. Current measurements were done with a point current meter in the channel and an Acoustic Doppler Current Profiler (ADCP) in the fracture. The ‘u’ axis of the ADCP was oriented along the channel, with positive ‘u’ pointed northeast. The ‘v’ axis was oriented across the fracture, with positive ‘v’ pointed northwest. 49

Figure 3.6 Schematic showing how channel cross-sectional geometry was used to calculate discharge, using the cross section and depth of flow for site 2. The channel was divided into 1 m horizontal segments over the depth where current measurements were available. The area of each segment was computed by parameterizing the segment as a trapezoid. Discharge was calculated for each segment and then summed to get total discharge through the channel. 53

Figure 4.1 Map of point surface elevation measurements along IPR transect grids from a Dual Frequency GNSS receiver unit post-corrected with Precise Point Positioning. Data are overlaid on a July 2016 ASTER image of the Milne Ice Shelf. Grids are labelled by letter on the map and inset boxes, black dashed lines indicate boundaries between grids. 56

Figure 4.2 Map of ice thicknesses measured along IPR transect grids. Data are overlaid on a July 2016 ASTER image of the Milne Ice Shelf from July. Grids are labelled by letter on map and inset boxes; black dashed lines indicate boundaries between grids. 57

Figure 4.3 A radargram from a cross-channel profile in grid D. Multiple radar traces are aligned side by side in a radargram, in order to show variation in the subsurface over horizontal space. The continuous black line just below 600 ns is the ice surface. The bright reflector at 1400 ns is the ice shelf-ocean interface. The channel can be seen in the ice shelf from trace 45 to 90. On the sides of the channel, there are places where no reflector can be seen or where identifying the correct reflector was not possible, due to multiple reflections due to off-nadir reflections from the angled sidewall. 60

Figure 4.4 Two representative cross-sectional ice thickness profiles (one plotted in green, one in black) from cross-channel (grids A to D) and cross-fracture (grid E) transects. Channel profiles run from the left (negative) to right (positive) where the left is defined in the downstream direction and zero corresponds to the centerline defined along the channel at the surface of the ice shelf. Fracture profiles run from north (negative) to south (positive) across the fracture; zero corresponds to the fracture centerline. Plots of channel and fracture cross-sections not shown here are provided in Appendix A..... 62

Figure 4.5 Boxplots showing variability in mean sidewall slope angle up from horizontal, calculated for each of the left and right sides of each cross-section, by grid. The right side of the channel is substantially steeper at grid C, whereas there is no significant difference in slope angle between the left and right sides for any other grid. The plot for grid E shows that sidewall slope angles on both sides of the fracture are consistently much steeper than those of the channel. 64

Figure 4.6 Boxplots showing variability in ice thicknesses measured with ice penetrating radar within the channel (grids A, B, C and D) and within the fracture (E). 66

Figure 4.7 Plots illustrating variability in snow depths measured along grid D IPR transects. A boxplot of snow depths (A) shows that median snow depth was 0.25 m, with a minimum of 0.00 and maximum of 2.60 m. A plot of snow depth (B) against distance from the channel centerline shows that snow depths were most variable in the depression overlying the channel; peak values were also located in the channel. 69

Figure 4.8 Temperature and salinity with depth for four locations in an along-channel CTD transect done in 2015 and 2016. Only the upper water column, to 50 m depth, is shown. Measurements taken within ice were removed from the top of the profiles and the downcasts isolated. The solid black line indicates the profile taken offshore of the ice shelf through a lead in the sea ice; the dashed line is the profile from sampling site 1 at the seaward edge of the channel; the dotted line is the profile from sampling site 2 located roughly mid-channel and the solid grey line is the epishelf lake profile for each year. ... 70

Figure 4.9 Salinity and temperature profiles for 2014, 2015 and 2016 showing profiles from the fracture, plotted against profiles from the epishelf lake and the channel for the same year for comparison. The channel was not profiled in 2014. For each profile, measurements taken in ice were removed, and the downcast isolated. The epishelf lake

profile is shown with a solid line, the fracture with a dashed line and the channel profile with a dotted line..... 72

Figure 4.10 Mean water speed with depth at the seaward edge of the channel (site 1), and approximately mid-way along the channel (site 2). Water speed was measured for 2 minutes at each depth, and the mean of the middle 80% of the recorded values taken. Mean speed (in m s^{-1}) is plotted in red; points indicate the depths at which water speed measurements were recorded. The dashed grey lines indicate one standard deviation from the mean. Salinity with depth at each location is plotted in blue..... 73

Figure 4.11 Photos of a weighted line lowered through a natural hole in the ice overlying the channel. Panel A shows the line before the weight reached the depth of fast flowing water: the line hung straight down into the water from the hand. Panel B shows the line when it has been taken up by the fast flowing near-surface current. The line was pulled downstream (left side of crack in the photo) and thus, angled away from vertical. The red dashed line marks the vertical from the hand for comparison. 75

Figure 4.12 Time-averaged velocities with depth in the water column at the fracture. The 'u' axis is along the fracture, with positive u running NE, toward the intersection of the fracture and channel. The 'v' axis is oriented roughly along-fiord, with positive v being toward the ocean. Grey dashed lines indicated one standard deviation from the mean for each depth. Depth bins are 1.5 m, with the center of the first bin at 2.33 m depth. 76

List of Appendices

Appendix A Cross-sectional ice thickness profiles from IPR survey grids

1 Introduction

1.1 Description of problem

The Milne Ice Shelf is one of the few remaining ice shelves in the Canadian Arctic, a remnant of the vast ‘Ellesmere Ice Shelf’ that once stretched along some 500 km of the northern coast of Ellesmere Island, Nunavut (Figure 1.1). These ice shelves, thick (>20 m) floating masses of ice attached to land, formed during a period of climatic cooling 4000 – 5500 years ago (England *et al.* 2008; Antoniadou *et al.*, 2011). The course of the 20th century, however, saw a greater than 90% reduction in ice shelf area; recent years (since ~2000) in particular have seen accelerated loss as massive calving events and in-situ fracturing occurred in short succession (Mueller *et al.*, 2003; Copland *et al.*, 2007; Vincent *et al.*, 2011; Mueller *et al.*, 2017a). Ice shelf decline is understood as a response to climate change: ice shelf loss is linked with periods of sustained above-average air temperatures, and a reduction in sea ice coverage along the seaward edge of ice shelves (e.g. Vincent *et al.*, 2001; Copland *et al.*, 2007; White *et al.*, 2015). Crucial to understanding past, present and future ice shelf loss, however, is an improved understanding of the specific mechanisms and processes that link climate warming and ice shelf break-up.

Studies from Greenland and Antarctica suggest that the nature of the sub-ice shelf hydrological system plays an important role in ice shelf stability. Basal melt channels formed by concentrated subglacial outflow plumes or melt-driven cavity circulation have been identified under many ice shelves and floating glacier tongues in Greenland and Antarctica (e.g. Rignot and Steffen, 2008; Le Brocq *et al.*, 2013; Langley *et al.*, 2014; Alley *et al.* 2016). The presence of basal channels can impact the strength and stability of

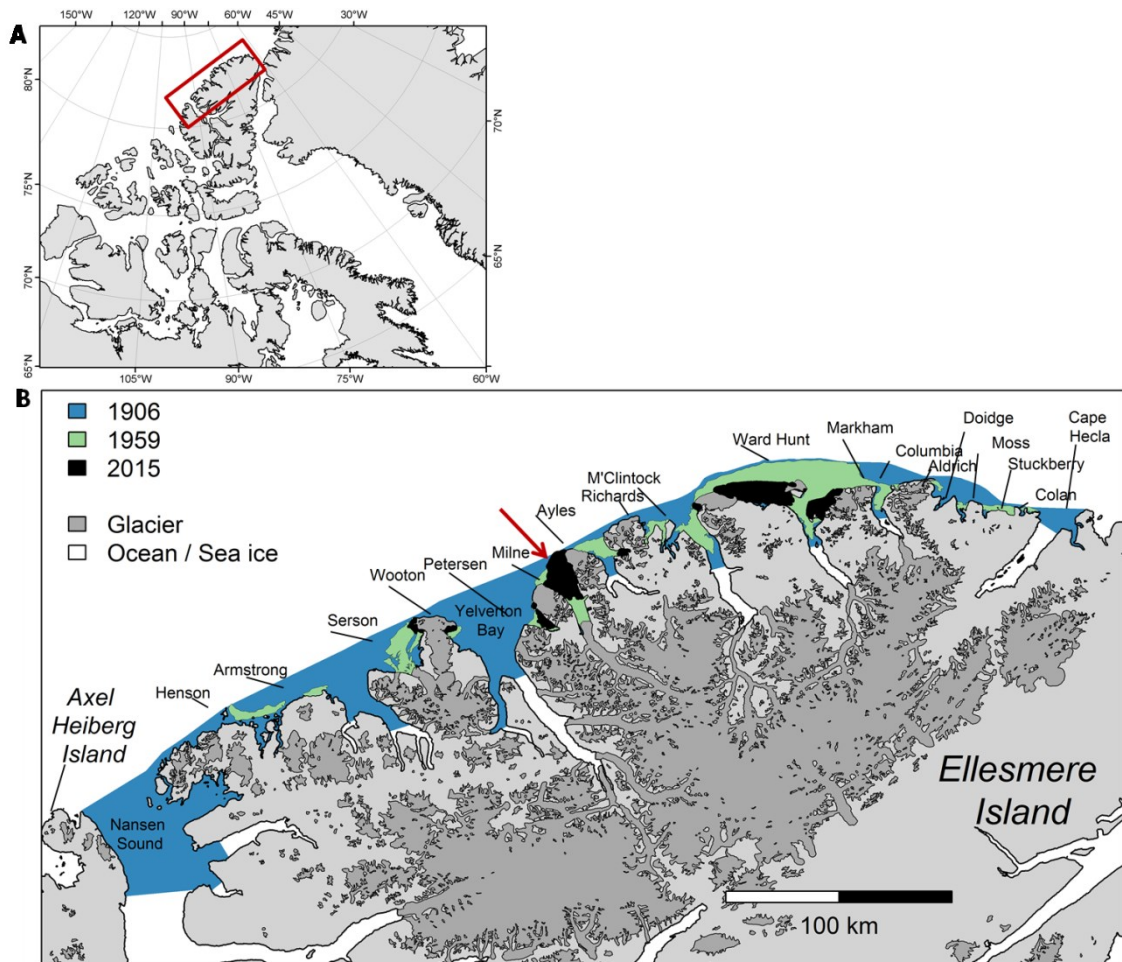


Figure 1.1 Maps of the locations and historic and present-day extents of ice shelves in the Canadian Arctic. Ice shelves are found only along the northwestern coast of Ellesmere Island, in the Canadian Arctic Archipelago (red box, panel A). Panel B shows the ice shelf extent as of 2015 in black, and the red arrow indicates the Milne Ice Shelf, located at the mouth of Milne Fiord. Green shows the greater maximum ice shelf extent in 1959, when the ice shelves were first mapped. The approximate extent of the ~8900 km² ‘Ellesmere Ice Shelf’, reconstructed from observations in the late 1800s/early 1900s, is shown in blue. White areas are ocean or sea ice; dark grey indicates glaciated areas (Figure adapted from Mueller et al., 2017a).

an ice shelf and may eventually lead to ice shelf break-up (Rignot and Steffen, 2008; Vaughan *et al.*, 2012).

Mueller *et al.* (2003) suggested that the 2001-2002 breakup of the Ward Hunt Ice Shelf, located in Disraeli Fiord on the northern coast of Ellesmere Island, occurred along a basal channel. The proposed mechanism of channel formation in the Canadian Arctic is the channelization of sub-ice outflow of relatively warm freshwater from ice-shelf dammed 'epishelf lakes'. Epishelf lakes are formed when an ice shelf completely blocks the mouth of a fiord, impounding snow and glacier meltwater that flows in to the fiord from its catchment, resulting in a perennial layer of freshwater that floats on denser seawater (Figure 1.2). So long as the thickness of the freshwater layer is less than the minimum draft of the ice shelf, the freshwater remains trapped behind the floating ice shelf dam. However, as the freshwater layer deepens beyond the minimum draft of the ice shelf, freshwater is exported out of the fiord to the ocean beneath the shelf base.

Epishelf lake outflow has generally been discussed in the literature as occurring in a thin layer distributed along the width of the ice shelf dam (Keys, 1978; Jeffries *et al.*, 1988). Vincent *et al.* (2001), however, suggested that drainage of the Disraeli Fiord epishelf lake might have been preferentially directed through a channel at the base of the Ward Hunt Ice Shelf. Melt along the channel may have thinned and weakened the ice shelf, eventually resulting in rifting through the entire thickness. The presence of basal melt channels beneath Ellesmere Island ice shelves has not yet, however, been explicitly investigated.

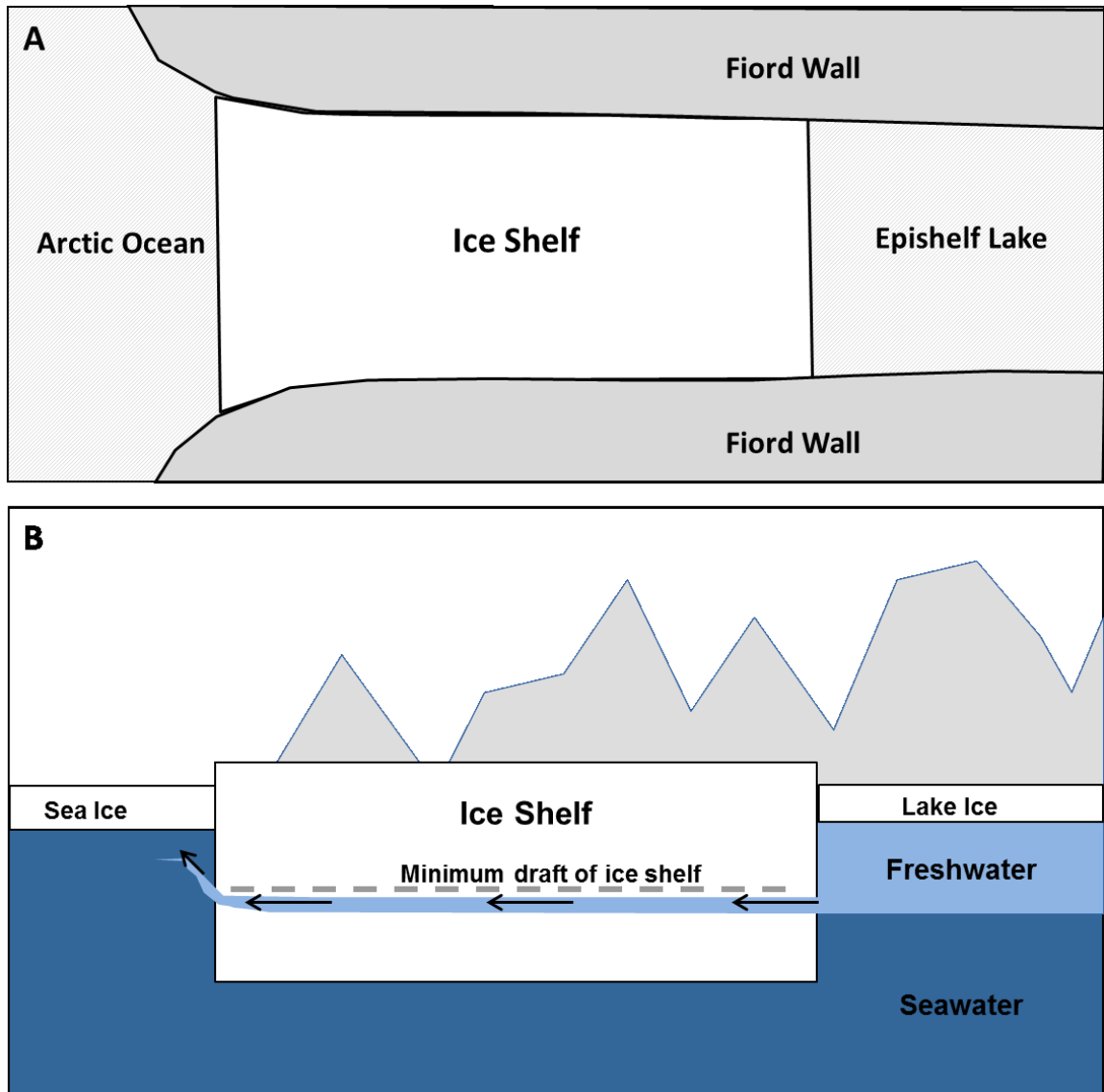


Figure 1.2 Schematics of an epishelf lake/ice shelf system (not drawn to scale) in plan view (A) and side view (B). The floating ice shelf dams terrestrial meltwater in the fiord, creating a density-stratified epishelf lake wherein freshwater floats on marine water. When the freshwater layer deepens beyond the minimum draft of the ice shelf, epishelf lake water flows out beneath the ice shelf to the Arctic Ocean.

This study aims to determine whether epishelf lake outflow is channelized beneath the Milne Ice Shelf. There is a curvilinear surface depression that runs E-W across the surface of the outer Milne Ice Shelf for 11 km, terminating at the seaward edge of the ice shelf (Figure 1.3, Panels A, C and D). This feature can be seen in aerial photos dating to as early as 1950 (Jeffries, 1986). There is evidence to suggest there is a basal channel incised into the base of the ice shelf beneath this E-W feature.

Previous ice thickness mapping of the ice shelf indicated that ice thicknesses in the vicinity of the depression were notably less than for other regions of the ice shelf, and that the most likely path for outflow would therefore be along this E-W feature (Narod *et al.*, 1988; Mortimer *et al.*, 2012; Hamilton *et al.*, 2017, Figure 1.4). Repeat ice thickness measurements at one location within the depression showed that ice thickness there decreased from ~40 m in 1981 to <10 m in 2008/2009 (Mortimer, 2011), which is broadly consistent with upward incision and the removal of mass from the ice shelf base. In addition, two cross-sectional profiles of ice thickness across the feature collected during previous surveys of the ice shelf were suggestive of channelization (Mortimer *et al.*, 2012; Hamilton, 2016).

The presence of a topographic low on the ice shelf surface is also consistent with channelization (Luckman *et al.*, 2012; Mankoff *et al.*, 2012); unsupported ice would deform downward as mass is preferentially removed by channelization. Longitudinal crevasses were also noted along the margins of the depression (Panel C, Figure 1.3). Crevassing is consistent with extensional stresses expected where the ice surface sags downward; similar crevassing is seen as a result of channelization of the Pine Island Glacier ice shelf in Antarctica (Vaughan *et al.*, 2012).

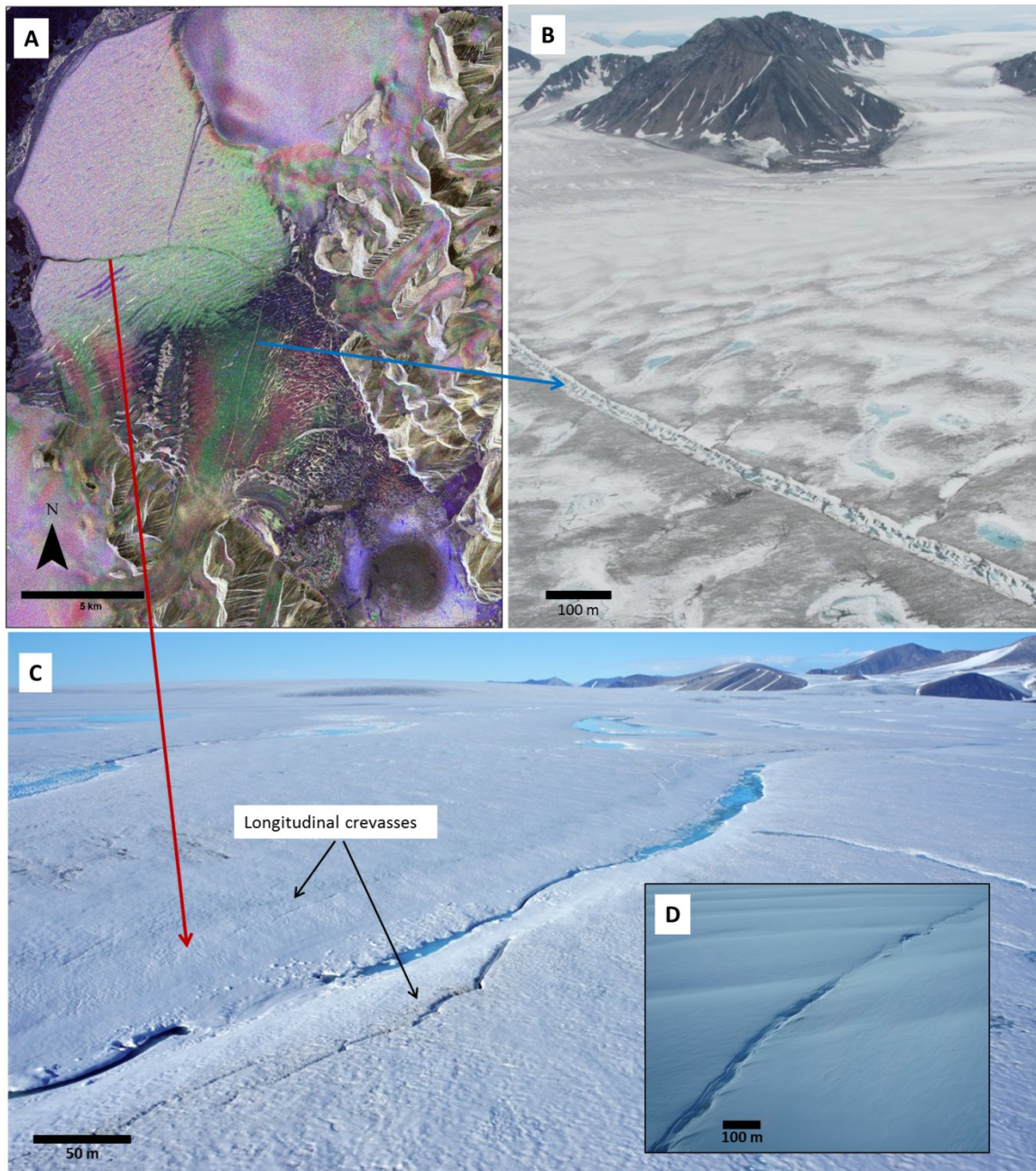


Figure 1.3 RADARSAT-2 Fine Quad image from July 2015 of the outer Milne Ice Shelf (A) showing the location of the E-W surface depression hypothesized to overlie a basal channel (red arrow). The blue arrow denotes a fracture formed in 2009 used in this study to compare morphology and hydrography of a channel and fracture. An older fracture that dates to at least 1950 can be seen intersecting the E-W depression. Panel B is a photo of the surface appearance of the fracture. Panel C shows the curvilinear E-W surface depression with longitudinal crevassing along the margins. Meltwater pools and snow can be seen in the depression, as well as in surrounding low spots on the ice shelf. An aerial photo shows the depression in plan view (D); the depression cross-cuts the characteristic rolling topography of the ice shelf.

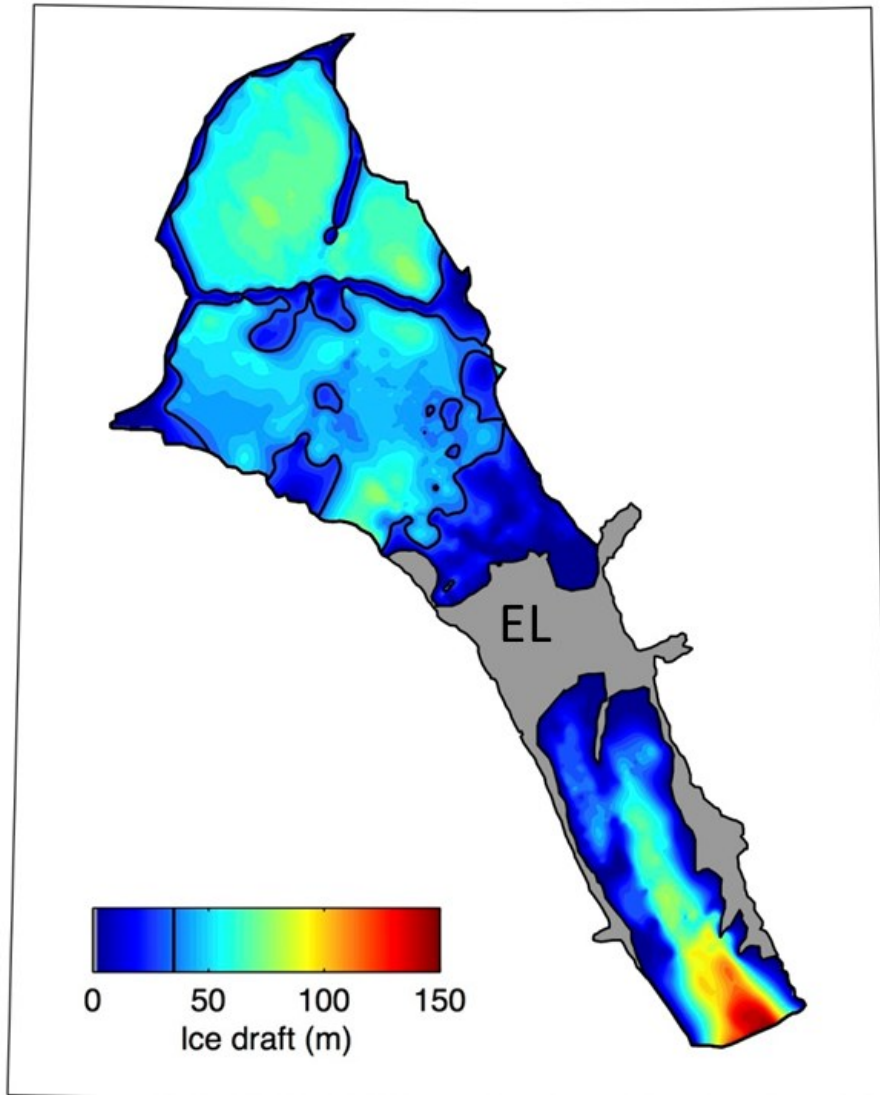


Figure 1.4 Map of modelled ice drafts for the Milne Ice Shelf and Milne Glacier tongue. The grey area is the epishelf lake with ice thicknesses ~ 1 m. The black line indicates the 35 m contour interval. Thin ice (< 10 m) can be seen along the depression that runs E-W across the outer ice shelf, indicating it was a likely path for outflow from the epishelf lake. Adapted from Hamilton (2016).

1.2 Research objectives

This study evaluates the hypothesis that the E-W surface depression on the outer Milne Ice Shelf overlies a basal channel incised into the ice shelf by outflow from the Milne Fiord epishelf lake. Accordingly, this study had the following objectives:

1. Characterize the basal morphology of the ice shelf beneath the surface depression, and compare it to that of a stress fracture that appeared on the ice shelf between 2008 and 2009 (Figure 1.3, panel B). The morphology of a channel incised by flowing water will differ from that of a stress fracture due to their different mechanisms of formation. A channel is expected to have an inverted 'v' shape, with sides that slope away from vertical. A fracture will be straight-sided, with sides closer to vertical.

2. Profile the temperature, salinity and water velocity in the water column below the feature, and compare these profiles to profiles taken in the epishelf lake, the fracture, and offshore of the ice shelf, to determine if water properties are consistent with sub ice-shelf channelized outflow of the epishelf lake water from the fiord.

3. Calculate discharge through the hypothesized drainage channel to determine whether it might be the primary drainage pathway for the Milne Fiord epishelf lake, thus gaining a better understanding of the sub-ice shelf hydrology.

1.3 Significance

As a result of ongoing ice shelf break-up along the northern coast of Ellesmere Island, Milne Ice Shelf dams what is likely the last remaining epishelf lake in the Northern Hemisphere (Veillette *et al.*, 2008). This work therefore represents the final opportunity to investigate the presence of basal channels and gain insight into how epishelf lake drainage may influence ice shelf mass balance and impact ice shelf stability in the

Canadian Arctic. Field measurements and observations from this study contribute to our knowledge of possible mechanisms that determine where, when, and how fractures form and breakup occurs. An understanding of mechanisms driving present deglaciation also provides insight into how past deglaciation may have occurred. The applicability of this study, however, is not limited to the Canadian Arctic. This work in Milne Fiord may also provide insight into deglaciation in Greenland and Antarctica, as Milne Fiord may represent a ‘future state’ of ice shelf systems for Greenland and Antarctica. In a warming climate, it is conceivable that epishelf lakes could develop in the Greenlandic and Antarctic contexts, if floating ice shelves or glacier tongues become separated from their glacial trunks but remain attached to the coast.

1.4 Thesis structure

This thesis follows a traditional thesis format. **Chapter 2** provides a review of relevant literature on Ellesmere Island ice shelves and epishelf lakes, ice shelf basal channels, and ice penetrating radar. The study area and the methods used in this study are described in **Chapter 3**. Study results are provided in **Chapter 4** followed by a discussion of the significance of these findings in **Chapter 5**. Finally, **Chapter 6** summarizes the main conclusions and outlines directions for future work building on this study.

2 Literature Review

2.1 Ellesmere Island ice shelves

Ice shelves are best known from Antarctica, where they cover ~40% of the Antarctic coastline (Drewry *et al.*, 1982). However, ice shelves also occur in northern Greenland, the Russian High Arctic (Dowdeswell, 2017), and in the Canadian High Arctic in protected bays and fiords along the northern coast of Ellesmere Island. Where Antarctic, Greenland and Russian ice shelves are the floating extensions of continental ice, ice shelves in the Canadian Arctic are both glacial and marine in origin. Ice shelf formation occurred through *in situ* surface snow accumulation and basal ice accretion onto multiyear landfast sea ice (MLSI) and/or glacier ice (Jeffries, 2002). As a result, Ellesmere Island ice shelves may be classified as sea-ice ice shelves (primarily marine in origin, e.g. the Ward Hunt Ice Shelf), glacier ice shelves (an ice shelf that has been, or is still, nourished directly by a glacier, e.g. the Milne Ice Shelf) or composite ice shelves, having both significant sea ice and glacier ice components (e.g. the Serson Ice Shelf) (Lemmen *et al.*, 1988). The addition of mass to an ice shelf can also occur via the accretion of sea ice along the seaward edge of the ice shelf after calving (a ‘reentrant’, Jeffries, 1986).

Ellesmere Island ice shelves range in thickness from ~20 m to ~100 m (Jeffries, 2002; Mortimer *et al.*, 2012; White *et al.*, 2015). They have a characteristic undulating surface topography of alternating ridges and troughs (‘rolls’), thought to be formed by the pattern of snow distribution and elongation of meltwater ponds by the prevailing winds (Crary, 1960; Jeffries, 1992). Ice shelf mass loss occurs through surface melt and calving (Jeffries, 2002). Estimates of ice shelf thinning and surface mass balance indicate that

basal melt is also likely an important contributor to ice shelf mass loss, but this has not yet been verified through direct measurements (Braun *et al.*, 2004; Mortimer *et al.*, 2012). Calving from ice shelves is characterized by the intermittent sudden detachment of one or more tabular icebergs ('ice islands') with an area of many times the ice thickness (Lazarra *et al.*, 1999). Calving of an ice island is preceded by the formation, propagation and intersection of fractures that penetrate the entire thickness of the ice shelf (Lazzara *et al.*, 1999). Calving can occur both at the front of an ice shelf (seaward edge), as well as at the rear of an ice shelf, into the fiord (c.f. Mortimer *et al.*, 2012). Ice shelves were formed during a much cooler climatic period and there is no evidence they can reform under current climatic conditions (Copland *et al.*, 2007).

2.2 Epishelf lakes

Epishelf lakes are formed when terrestrial freshwater is dammed behind a floating ice shelf. Two types of epishelf lakes have been identified, distinguished by the nature of their connection with the marine environment (Gibson and Andersen, 2002). The first is one where the freshwater lake is located on land, and exchange between the freshwater and ocean occurs indirectly, through a conduit beneath the ice shelf at the ice-land interface or through cracks in the ice shelf (Gibson and Andersen, 2002). In the second, the freshwater layer floats directly on seawater and the thickness of the freshwater layer is controlled by the thickness of the ice shelf dam. It is this type of epishelf lake that has been identified along the coast of Ellesmere Island, where ice shelves span the mouth of a fiord or bay (Veillette *et al.*, 2008; Jungblut *et al.*, 2017).

Arctic epishelf lakes are highly stratified, with a well-mixed layer of relatively warm, fresh to slightly brackish water (absolute salinities of $<1.5 \text{ g kg}^{-1}$, temperatures just

above zero to $\sim 4^{\circ}\text{C}$) overlying seawater ($\sim 30 \text{ g kg}^{-1}$, $< -1^{\circ}\text{C}$) separated by a steep salinity and temperature gradient (the halocline and thermocline, respectively) (Keys, 1978; Veillette *et al.*, 2008; Hamilton *et al.*, 2017). The strong and persistent density stratification is due to a perennial freshwater ice cover on the epishelf lake, which precludes wind mixing (Keys, 1978; Veillette *et al.*, 2008; Hamilton *et al.*, 2017). Since there is no physical barrier between the fresh and marine waters, epishelf lakes experience some tidal exchange. However, the tidal ranges along the coast of Ellesmere Island are very small (typically $< 0.20 \text{ m}$ between high and low tides, Copland *et al.*, 2017), so mixing from below is also limited (Veillette *et al.*, 2008). The freshwater layer is warm because the meltwater runoff that enters the fiord is above freezing, there is little heat loss to the atmosphere because of a thick insulating snow cover during the winter, and convective heat loss to the cold ocean below is limited because there is little mixing at the freshwater-saltwater interface due to strong density stratification (Keys, 1978; Hamilton, 2016). Solar heating also warms the water near the surface (Veillette *et al.*, 2008).

The minimum depth of the freshwater layer is approximately equivalent to the minimum draft of the ice shelf; below this depth, there is free exchange between the fiord and offshore (Keys, 1978; Vincent *et al.*, 2001; Hamilton *et al.*, 2017). The freshwater layer deepens over the course of the melt season with meltwater input to the fiord, with the volume of inflow in a given year dependent on the strength of the melt that year (Hamilton *et al.*, 2017). When inflow causes an epishelf lake to deepen past the minimum draft of the ice shelf, water flows out of the fiord beneath the base of the ice shelf, driven by the difference in density between the buoyant freshwater column and denser seawater

(Keys, 1978; Hamilton *et al.*, 2017). Outflow would cease once the depth of the epishelf lake is equivalent to (or less than) the ice shelf minimum draft.

Epishelf lake outflow could contribute to ice shelf growth, through basal freeze-on of ice (Keys, 1978; Jeffries and Sackinger, 1988; Jeffries, 1991). Based on measurements in Disraeli Fiord, Ellesmere Island, Keys (1978) suggested that, as brackish water near the freezing point flowed from the base of the epishelf lake under the ice shelf, it would lose heat to the colder seawater below and could form ice crystals or supercooled water that would subsequently accrete to the base of the ice shelf. Although there have been no in-situ measurements of sub-ice shelf circulation, ice cores from the Ward Hunt Ice Shelf suggest basal accretion of epishelf lake water had occurred beneath the Ward Hunt Ice Shelf (Jeffries and Sackinger, 1988). Keys (1978) theorized that epishelf outflow must occur in a ‘uniform sheet’ across the width of the ice shelf. He reasoned that if epishelf lake water flowed out through a channel, the channel would quickly be filled by ice formed when cooled epishelf lake water came in contact with the ice shelf base and thus, a consistent ice dam thickness should be maintained by basal accretion (Keys, 1978). The presence of a deeply incised basal channel in an ice shelf implies that Keys’ model is perhaps too simplistic, or that channelization is unlikely to be initiated by outflow alone.

2.3 Ice shelf change

Observations from early 20th century explorations along the northern coast of Ellesmere by Lieutenant Pelham Aldrich and Commander Robert Peary suggest that there was once a continuous ice shelf along the northern coast of Ellesmere, with an area of ~8900km² (Figure 1.1; Vincent *et al.*, 2001). By the early 1950s, however, episodic calving had significantly reduced the Ellesmere Ice Shelf, leaving several small individual ice shelves

in protected bays and fiords (Vincent *et al.*, 2001). From the 1950s to the end of the 20th century, ice shelves were relatively stable (Mueller *et al.*, 2017a). By the end of the 20th century, six major ice shelves remained, with a combined area of 1043 km²: the Serson, Petersen, Ward Hunt, Milne, Markham and Ayles ice shelves (Mueller *et al.*, 2006).

A renewed period of ice shelf loss and breakup occurred from the early 2000s until 2012, which included the loss of the Ayles Ice Shelf in 2005 (Copland *et al.*, 2007), a 60% reduction in area of the Serson Ice Shelf, calving of the entire 50 km² Markham Ice Shelf in 2008 (Mueller *et al.*, 2008; Vincent *et al.*, 2009), and ongoing decline of the Ward Hunt and Petersen ice shelves (Mueller *et al.*, 2017a). The pace of loss has reduced since 2012 but this is likely a temporary lull (Mueller *et al.*, 2017a). Presently, five major ice shelves remain (the Serson, Petersen, Ward Hunt, Ward Hunt East and Milne ice shelves) which represent <6% of the area of the original Ellesmere Ice Shelf (Mueller *et al.*, 2017a).

Ice shelf loss and disintegration have also resulted in the disappearance of epishelf lakes, since the existence of an epishelf lake is dependent on an intact ice shelf dam (Veillette *et al.*, 2008). In 2002, for instance, the fracturing event that bisected the Ward Hunt Ice Shelf resulted in the drainage of the associated epishelf lake in Disraeli Fiord (Mueller *et al.*, 2003). Fracturing of the Petersen Ice Shelf in 2005 also resulted in the drainage of the epishelf lake it dammed (White *et al.*, 2015). At one time, the Ellesmere Ice Shelf may have dammed up to 17 epishelf lakes (Veillette *et al.*, 2008). As recently as 2007, epishelf lakes were likely still present in five fiords or embayments (Veillette *et al.*, 2008). At present however, Milne Fiord appears to contain the only remaining deep epishelf lake in the Arctic (Veillette *et al.*, 2008).

The Milne Ice Shelf has suffered less dramatic loss than other ice shelves along the coast of Ellesmere Island, but nonetheless has decreased in size. Between 1950 and 2009, there was a 29% reduction in ice shelf area, which amounted to an 82 km² loss (Mortimer *et al.*, 2012). One large calving event of 26 km² occurred sometime between 1959 and 1974 from the northwest corner of the ice shelf (Jeffries, 1986). The ice that calved from the front was replaced by thinner multiyear landfast sea ice (MLSI) (the Milne ‘re-entrant’ of Jeffries, 1986). The remainder of the loss occurred through calving at the rear of the ice shelf and through expansion of ice marginal lakes, causing an expansion of the area of the epishelf lake (Mortimer *et al.*, 2012; Mueller *et al.*, 2017a). Several new fractures also developed on the ice shelf between 1981 and 2009 (Mortimer, 2011).

In addition to changes in ice shelf extent, ice shelves in the Canadian Arctic have also thinned. Thinning occurs when ablation from surface and/or basal melt outpaces accumulation from surface precipitation, basal accretion, and glacial input. Ablation stake measurements on the Ward Hunt, Petersen and Milne ice shelves indicate an increasingly negative surface mass balance as a result of increased temperatures and greater surface melt (Braun *et al.*, 2004; Mortimer *et al.*, 2012; White *et al.*, 2015). A repeat survey of historical radio echo sounding measurements of ice thickness on the Milne Ice Shelf by Mortimer *et al.* (2012) showed that the ice shelf thinned by an average of 8.1 m from 1981-2009. Observations of a 27% reduction in the depth of the Disraeli Fiord epishelf lake 1967 to 1999 also suggested the Ward Hunt Ice Shelf thinned over that time, though thinning did not necessarily occur evenly across the whole ice shelf (Vincent *et al.*, 2001). As mentioned previously, there is little known about basal melt rates beneath ice shelves along the coast of Ellesmere Island, so the relative contributions of basal and

surface melt to thinning are not well resolved. The loss of epishelf lakes associated with ice shelves means that the potential for basal accretion, which can add mass to an ice shelf and offset ablation, is also lost (c.f. Jeffries, 1991).

2.4 Consequences of ice shelf breakup

Ice shelf break-up does not contribute to sea level rise as the ice is already floating (Jeffries, 2002), but it has other potential consequences. Disintegration can result in the production of very large tabular icebergs ('ice islands'). Ice islands that calve from the Northern Ellesmere ice shelves may drift into the Beaufort or Chukchi seas under the influence of the Beaufort Gyre, where they present a potential hazard to offshore industry or shipping (Jeffries, 1992; Mueller *et al.*, 2013). Epishelf lakes provide a unique habitat wherein marine and freshwater organisms co-exist within the same water column, stratified by the different habitats that exist at different depths, while meltwater ponds on the surface of ice shelves are colonized by rare cold-tolerant microbial communities (Vincent *et al.*, 2000; Veillette *et al.*, 2011; Jungblut *et al.*, 2017). Ice shelf loss results in a loss of these rare habitats and the organisms that depend on them.

2.5 Causes of ice shelf breakup

The Arctic is warming at nearly twice the rate of the global average temperature (ACIA, 2004). The mean annual Arctic land surface air temperature for 2000-2013 was 1.0°C higher than the average for 1981-2000 (Overland *et al.*, 2014). Sustained periods of years where annual positive degree days exceed 200 are linked to increased rates of calving and break-up events in the Canadian Arctic (Copland *et al.*, 2007). It is likely that long-term negative surface mass balances and thinning, due to the increase in mean annual temperatures, result in 'pre-weakened' ice shelves that are increasingly vulnerable to

various stresses that ultimately cause break-up events (Mortimer *et al.*, 2012; Copland *et al.*, 2017). The timing of ice shelf calving events also appears to be related to periods of low sea ice coverage and increased open water along the seaward edges of Ellesmere Island ice shelves (Copland *et al.*, 2017). Arctic sea ice extent has declined over the satellite record and the lowest extents in the satellite record have all occurred since the end of the 20th century (Stroeve *et al.*, 2012). A sea ice ‘buffer’ along the edges of ice shelves is important in maintaining ice shelf stability because it provides a physical barrier that holds the ice shelf in place and protects it from wind, waves and impacts with pack ice (Copland *et al.*, 2007).

Persistent winds, waves and tides have all been suggested as potential mechanisms that, coupled with ‘pre-weakening’, may induce stresses large enough to finally cause fracturing and calving of ice shelves, determining the precise timing of breakup events. Ocean tides can cause the ice to flex, leading to bending stresses that might enlarge existing cracks or create new fractures: Holdsworth (1971) suggested that the calving of the Ward Hunt Ice Shelf in 1961-1962 was the result of an extreme tidal range where low water fell to 50 cm below its normal value, perhaps combined with a coincident seismic event. Strong winds blowing across an ice shelf may also exert sufficient stress to induce fracturing. Strong offshore winds are thought to have been key in triggering calving of the Ayles Ice Shelf in 2005 (Copland *et al.*, 2007). It has also been proposed that ocean waves might induce vibrations in the ice which can increase stresses to the point that fracturing occurs (Holdsworth and Glynn, 1981).

2.6 Basal channels

2.6.1 Basal channel formation

The melt rate of an ice shelf by warm water is primarily a function of flow velocity and thermal driving, which is the difference in temperature between the water and the freezing temperature at the ice shelf base (Holland *et al.*, 2008). Basal channels form when warm water beneath an ice shelf somehow becomes concentrated, resulting in locally higher melt rates and, thus, incision of the ice shelf base (Dutrieux *et al.*, 2013; Stanton *et al.*, 2013). In Greenland and Antarctica, ice shelf melt is driven by ice shelf exposure to relatively warm ocean waters at depth, which causes melting at the ice shelf base. Ice shelves thin away from their grounding lines, resulting in a sloped base. Meltwater is less dense than seawater, so it rises along the sloped ice shelf base in a buoyant plume, entraining the warm waters from below as it goes; heat supplied by this entrained ocean water is used to melt the ice shelf base (Figure 2.1; Jenkins, 1991; Jenkins, 2011). Additional freshwater may be added by the discharge of subglacial meltwater across the grounding line of the ice shelf, resulting in even stronger buoyant plumes (Jenkins, 2011). Several mechanisms have been proposed to explain how the channelization of warm water is initiated beneath Antarctic and Greenland ice shelves. Basal channels under some ice shelves may be the result of channelized subglacial discharge exiting the grounding line of an ice shelf (i.e. channels are an ‘extension’ of the subglacial hydrological pathways) (Le Brocq *et al.*, 2013). In other cases, it is thought that variations in ice thickness, caused by topographic features upstream of the grounding line (Gladish *et al.*, 2012) or variability in lateral shear along ice shelf margins (Sergienko *et al.*, 2013) are preferentially amplified and deepened by ocean melting via the buoyant

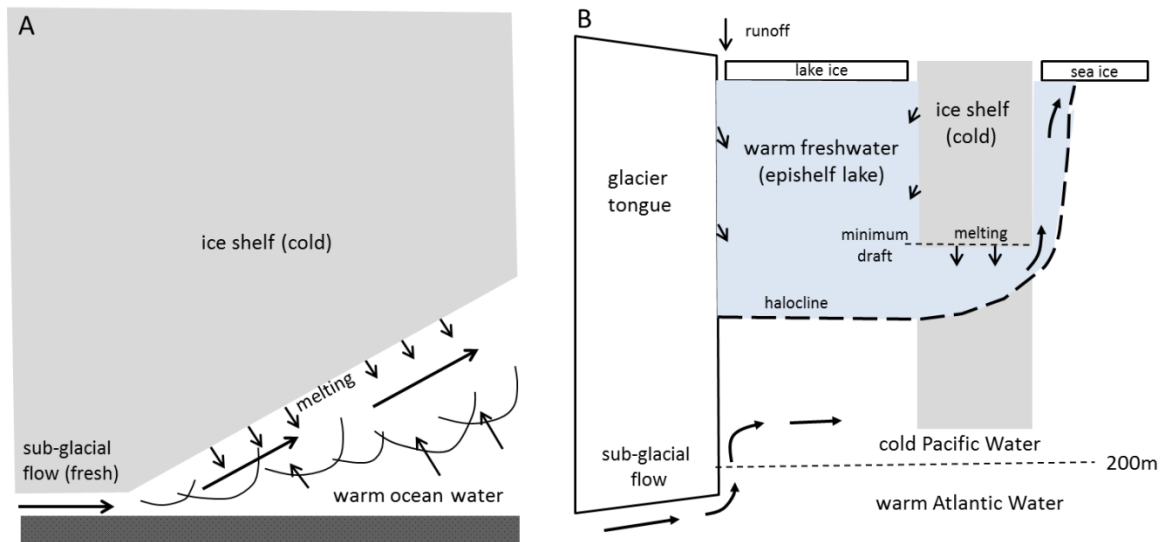


Figure 2.1 Ice shelf basal melt and channelization driven by (A) a buoyant freshwater plume originating from sub-glacial discharge and basal melt of an ice shelf and (B) channelized outflow of warm epishelf lake beneath an ice shelf. For a thick ice shelf exposed to warm water, typical of ice shelves in the Antarctic and Greenland, meltwater is generated at depth and may be supplemented by fresh subglacial discharge across the grounding line. The buoyant freshwater rises along the sloped base of the ice shelf in a buoyant plume, entraining warm water from below. Heat supplied by entrained ocean water is used to melt the ice shelf base. In the Canadian Arctic, the source of heat to melt and incise ice shelves is the freshwater impounded by an ice shelf. Epishelf lakes stay above 0°C year round; outflow beneath an ice shelf occurs when the epishelf lake thickens beyond the minimum draft of the ice shelf. Adapted from Jenkins, 2011 (A) and Hamilton et al., 2017 (B).

plume (Gladish *et al.*, 2012). Regardless of the mechanism of formation, once a channel is initiated, the buoyant meltwater plume is then preferentially directed into the channel, resulting in flow speeds and melt rates that are much higher within the channel than out of the channel (Rignot and Steffen, 2008; Dutrieux *et al.*, 2013).

Beneath the Milne Ice Shelf, entrainment of warm water by buoyant freshwater plumes is unlikely to be a source of warm water for potential channelization and melt of the ice shelf base (Figure 2.1). Warm (0-3°C), saline Atlantic Water is found only below ~200 m depth in Milne Fiord, above that is cold, fresh Pacific Water (Hamilton, 2016). The Milne Ice Shelf is thin enough that it does not float in Atlantic Water, so it is insulated from this warm layer. While there are also subglacial meltwater plumes discharged across the grounding line of Milne Glacier that entrain warm water at depth, these plumes reach their level of neutral buoyancy (the depth at which they no longer rise through the water column) between 30 and 55 m depth, which is below the halocline marking the base of epishelf lake (Hamilton, 2016). The sole source of warm water to drive basal channelization in Milne Fiord is therefore outflow from the epishelf lake. The epishelf lake represents a significant source of heat to melt ice as it has an elevated heat content (temperatures >0°C) year round (Hamilton, 2016). Concentration of epishelf lake outflow in a channel would result in an elevated heat flux from the relatively warm epishelf lake water to the ice (Hamilton *et al.*, 2017).

2.6.2 Channel morphology

Channels identified under Antarctic and Greenland ice shelves are hundreds of meters to a few kilometers wide, with heights of many tens to hundreds of meters (Rignot and Steffen, 2008; Vaughan *et al.*, 2012; Dutrieux *et al.*, 2014). Channel orientations both

parallel and perpendicular to the direction of ice flow have been observed (Rignot and Steffen, 2008; Dutrieux *et al.*, 2014). A surface depression is associated with most channels, formed by the downward sagging of unsupported ice at the channel crest (Mankoff *et al.*, 2012; Vaughan *et al.*, 2012). These depressions, however, are often not as deep as would be expected if the ice was in hydrostatic equilibrium, because of snow accumulation in the depression or bridging stresses limiting relaxation (e.g. Vaughan *et al.*, 2012).

Channels have sides that slope away from vertical, but the slope of the channel sides does not appear to be consistent; reported channel height to width ratios vary between ice shelves (Rignot and Steffen, 2008; Le Brocq *et al.*, 2013; Langley *et al.*, 2014). Channel sides have been characterized as smooth by several investigators (Rignot and Steffen, 2008; Stanton *et al.*, 2013), although Dutrieux *et al.* (2014) found evidence of stepped terraces along channel walls on the Petermann Glacier and Pine Island Ice Shelf. Melting in channels may take place right at the channel apex (Stanton *et al.*, 2013) or it may be more concentrated along channel sides (Rignot and Steffen, 2008; Dutrieux *et al.*, 2014), depending on the stratification of the water column in the channel. Modelling studies also suggest that channel morphology should be asymmetrical, due to the deflection of flow through a channel by the Coriolis force (Sergienko *et al.*, 2013). This deflection results in melt concentrated to one side and, thus, a steeper sidewall on the side because melt is intensified where flow is faster (Gladish *et al.*, 2012; Sergienko *et al.*, 2013).

2.6.3 Impacts of channelization

The presence of basal channels reduces the mechanical strength of an ice shelf, as concentrated melt causes localized thinning (Rignot and Steffen, 2008). Crevassing at the base and surface in the vicinity of a channel, due to the generation of extensional stress as the ice shelf settles back to hydrostatic equilibrium, also reduces the structural integrity of an ice shelf (Vaughan *et al.*, 2012). While strength is locally reduced along a channel due to thinning and crevassing, however, the presence of basal channels may in some cases actually reduce the total amount of melting occurring under an ice shelf. By concentrating the melting in channels, modelling studies show that the mean melt rate elsewhere is diminished, which can result in less melting overall than if no channels were present (Gladish *et al.* 2012; Millgate *et al.*, 2013).

While this scenario may hold true for Antarctic and Greenland ice shelves, it likely does not apply in the Ellesmere Island oceanographic context. A thin, distributed layer of epishelf lake outflow is more likely to result in epishelf lake water quickly losing heat and freezing on to the ice shelf base, adding mass, not causing additional melt. Channelized melt would therefore be more likely to destabilize an ice shelf in the Canadian Arctic, through the combined effects of localized thinning and the loss of a mechanism to add mass to the ice shelf.

2.6.4 Detection and characterization of ice shelf basal channels

The presence of basal channels beneath ice shelves and floating glacier tongues can be inferred from the presence of surface depressions seen in satellite imagery (Humbert *et al.*, 2015; Alley *et al.*, 2016). In some cases, surface topography can yield information about channel cross-sectional and plan morphology (Alley *et al.*, 2016). However, the

degree to which surface topography echoes basal topography depends on many factors, including the time ice has had to adjust to the removal of mass from the base, bridging stresses in the ice and the pattern of surface accumulation of mass since the formation of the depression (Luckman *et al.*, 2012; Humbert *et al.*, 2015). Therefore, to obtain detailed and accurate information about the morphology and extent of basal channels beneath ice shelves, it is necessary to image the ice shelf base.

Limited measurements of channel morphology have been obtained through acoustic radar surveys by autonomous underwater vehicles deployed beneath ice shelves (Vaughan *et al.*, 2012). Much more common, however, is the use of airborne or ground penetrating radar for mapping of basal channels (e.g. Rignot and Steffen, 2008; Vaughan *et al.*, 2012; Langley *et al.*, 2014). Ground penetrating radar uses the transmission and reflection of radio waves to image the subsurface (Annan, 2009). The application of radar specifically to the imaging of ice bodies is referred to as ice penetrating radar (IPR). Identification of the ice-water interface of a floating ice shelf or glacier tongue gives ice thickness; this is combined with surface elevation measurements to yield a detailed picture of ice shelf basal topography (Cassidy, 2009). In this study, IPR was used to map the purported channel incised into the base of the Milne Ice Shelf. A review of important physical principles and survey considerations for IPR studies follows.

2.7 Ice penetrating radar

2.7.1 Physical principles of ice penetrating radar

An IPR system is composed of a transmitter and a receiver and a pair of antennae in a fixed geometry (Figure 2.2). The transmitter sends an electrical signal to the transmitting antenna, which then sends a pulse of radar waves into the ice at regular intervals. Where

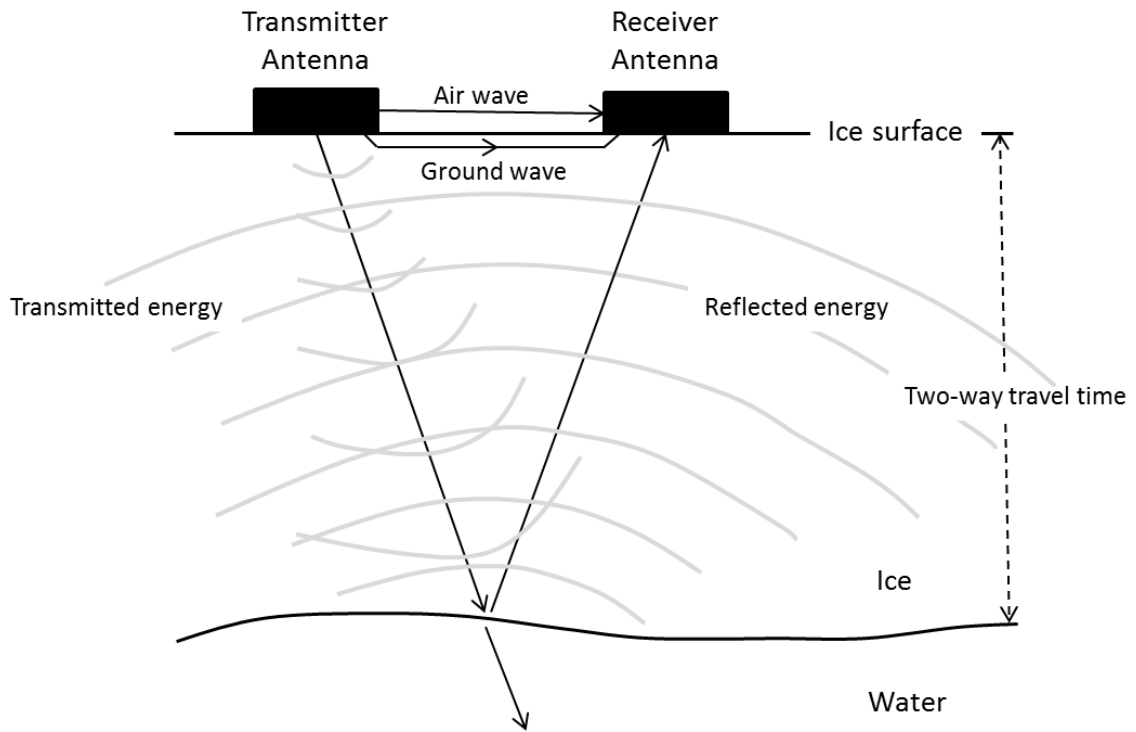


Figure 2.2 Ice penetrating radar (IPR) set up: the transmitting antenna sends a pulse of electromagnetic energy into the ice. When the pulse hits a boundary between materials with different electrical properties, some of the transmitted energy is reflected back to the surface. Some of the energy is absorbed and some transmitted into the underlying substrate. The amplitude and two-way travel time of the reflected pulse is recorded by the receiver antenna. Two-way travel time can be converted to distance to the reflector, using the velocity of the radar wave in ice.

the pulse encounters a boundary between media with different electrical properties (e.g. travelling from ice to water or ice to air) some of this energy is reflected back up to the surface, while the rest is either absorbed or penetrates into the underlying material (Annan, 2009). The amplitude (strength) and travel time of this reflected pulse is recorded by the receiver antenna at the surface. Two-way travel time can be converted to depth (and, thus, ice thickness, if the reflector marks the base of the ice mass) by assuming a velocity for the electromagnetic wave in the ice.

The propagation velocity (V) of a radar wave through ice (or any material) is controlled primarily by the relative permittivity (Annan, 2009):

$$V = \frac{c}{\sqrt{\epsilon_r}} \quad (2.1)$$

Where c is the speed of light in a vacuum ($3.00 \times 10^8 \text{ m s}^{-1}$) and ϵ_r (unitless) is the relative permittivity of a material, defined as the ratio between the absolute permittivity of the material to permittivity in a vacuum. Relative permittivity or the ‘dielectric constant’, describes how easily electromagnetic energy can move through a material (Hubbard and Glasser, 2005). Permittivity impacts the propagation velocity of a pulse: velocity will be higher through a material with a low relative permittivity than one with a higher relative permittivity. Table 2.1 shows the electrical properties of ice and water relative to other common earth materials. Where a radar wave travels from one material to another, the amplitude of the reflected wave is a function of the contrast in the relative permittivity of the two materials (Hubbard and Glasser, 2005). The relative permittivities of ice (3-4) and water (80) are very different, so IPR works well to identify the location of the ice-water boundary for floating glacier tongues and ice shelves. Previous studies have

Table 2.1 Typical values for the electrical properties of common earth materials.
Adapted from Hubbard and Glasser (2005).

Material	Relative electrical permittivity (ϵ_r)	Electrical conductivity (σ , mS m ⁻¹)	Radar wave propagation velocity (V, $\times 10^8$ m s ⁻¹)
Air	1	0	3.0
Fresh water	80	0.5	0.33
Ice	3-4	0.01	1.67
Salt water	80	3000	0.1
Granite	4-6	0.01-1	1.3
Silt	5-30	1-100	0.7

successfully used IPR to determine the thickness of the Milne Ice Shelf (Narod *et al.*, 1988; Mortimer *et al.*, 2012).

The strength of a returned radar signal recorded at the surface is also impacted by factors that cause signal loss within the material. Electrical conductivity describes the ability of a material to conduct an electric current (Table 2.1, Hubbard and Glasser, 2005). In conductive materials, such as saline ice, the radar signal attenuates (loses energy) rapidly and will not propagate as deeply (Cassidy, 2009). In contrast, pure ice is a 'low-loss' material, meaning there is a low signal loss with depth (Hubbard and Glasser, 2005). Radar signal strength loss also occurs as a result of reflections off heterogeneities within the ice, which leads to unwanted scatter, termed 'noise' or 'clutter' (Hubbard and Glasser, 2005). Scattering loss depends on the size, number and nature of scattering bodies in the ice, as well as the radar wavelength (Plewes and Hubbard, 2001).

The radar wave that propagates through the ice is a spherical wave, so it also suffers from attenuation due to geometrical spreading as a result of the spherical distribution of the energy at the front of the wave (Hubbard and Glasser, 2005). Signal loss also increases with radar frequency (Annan, 2009). A lower frequency antenna will therefore result in less attenuation and a deeper signal penetration but will also increase scattering loss and thus, decrease vertical resolution (Hubbard and Glasser, 2005). The antenna frequency chosen for a survey should therefore maximize resolution while also accounting for radar signal loss and ensuring sufficient depth of penetration. Antenna frequencies of 5 to 1000 MHz are typically used to profile ice, depending on the survey goals and site characteristics (Hubbard and Glasser, 2005).

2.7.2 Considerations for IPR data collection and analysis

A common-offset IPR survey is used to image the subsurface in the horizontal plane (Annan, 2009). In a common-offset configuration, the transmitter and receiving antenna are moved together, always separated by a constant distance, which is determined by the antenna frequency used for the survey (Annan, 2009, Figure 2.3). As the radar system is moved along the surface, data are recorded as individual radar traces, at regular intervals along the survey line (Figure 2.3). Traces are plotted as returned signal amplitude (x-axis) against time (y-axis). Traces can also be plotted side by side to produce a radargram which shows variation in reflections over space, to assist in interpretation (Hubbard and Glasser, 2005).

The first (earliest) wavelet seen in a trace is the direct wave, or airwave, which travelled from the transmitter to the receiver through the air at the speed of light (Hubbard and Glasser, 2005, Figure 2.3). Then there is the coupled wave, or ground wave, which travels directly between the transmitter and receiver through the ice, and is of opposite polarity to the air wave (Arcone *et al.*, 1995). It arrives slightly later, having travelled through the ice slower than the radar wave in air (Hubbard and Glasser, 2005). Later returning reflections represent reflections from within the ice and the basal interface, as well as below the interface until the wave is attenuated. The polarity of the reflected waves can be used to understand the nature of the reflector and identify the ice base. A reflected wave passing from a low to high relative permittivity material (e.g. ice to water, as in the case of a floating ice shelf) will have the same polarity as the air wave (Arcone *et al.*, 1995). A reversed polarity wave would indicate a transition from a high to low relative permittivity, e.g. ice to air or water to ice, which could indicate an air or

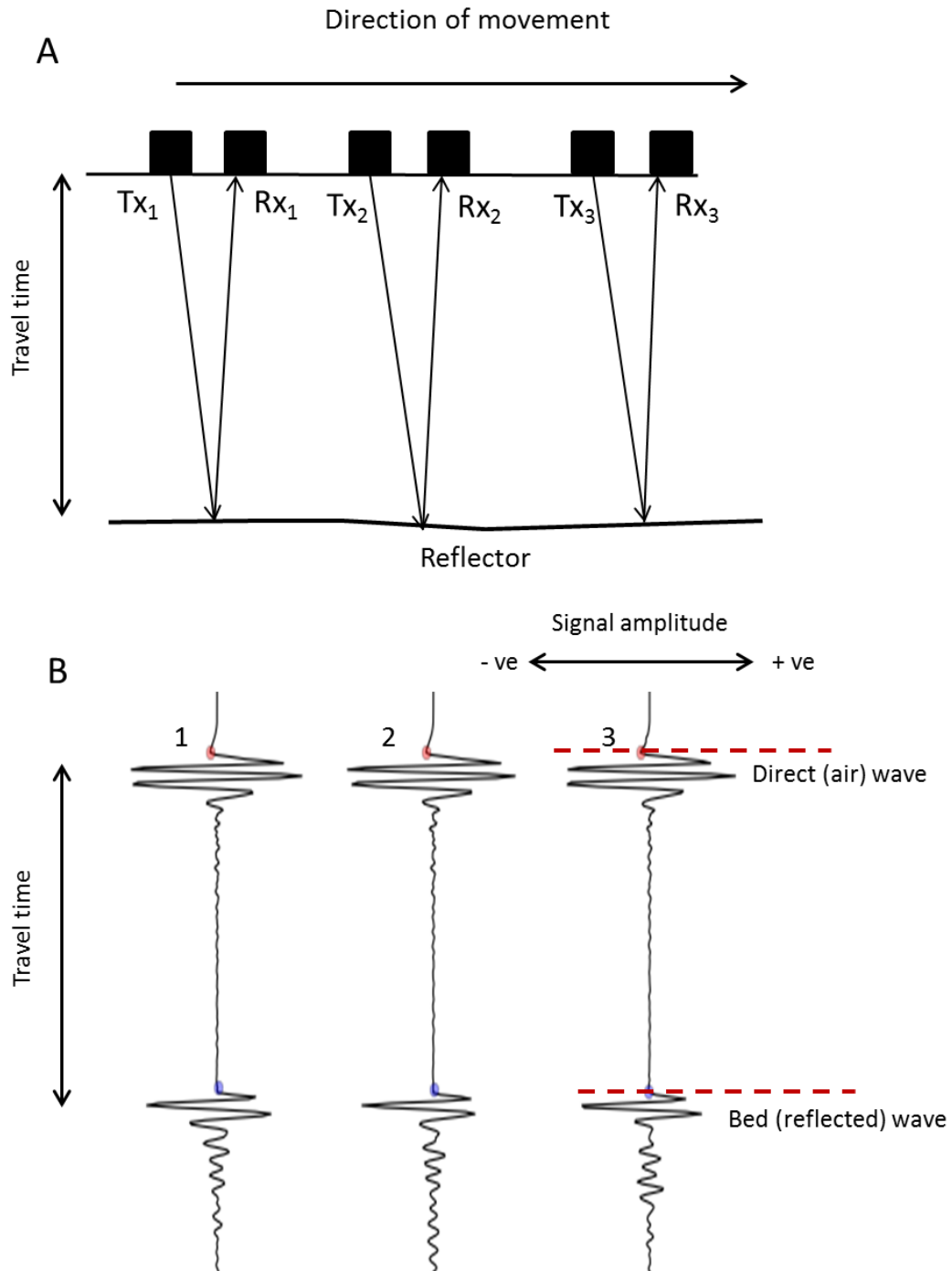


Figure 2.3 Configuration of a common-offset survey (A) and the resulting series of radar traces (B). Pulses are sent and received at regular intervals moving along the direction of travel. The associated traces show the amplitude and polarity of the transmitted pulse (airwave and ground wave combined) and the reflected pulse (bed wave). Red dashed lines indicate the location of the wavelet 'first break', which is the first increase in energy. Two-way travel time to the reflector is calculated using the position of the airwave first break and bed wave first break. Adapted from Cassidy (2009).

water-filled cavity within the ice. In terms of reflection patterns over space, the simplest case in an IPR survey is where the base is a planar reflector. However, the spherical nature of the radar wave means that steeply dipping reflectors in the ice body (such as the sloping sidewalls of a basal channel, for instance) will cause reflection patterns that obscure the true nature of the reflector. An angled reflector will result in reflections from points other than that directly below the radar (the nadir) (Navarro and Eisen, 2010). To facilitate interpretation, migration can be used in post-processing to move off-nadir reflectors to their correct spatial position (Fisher *et al.*, 1992).

The vertical resolution of a radar survey (the minimum detectable ice thickness) is determined by the wavelength of the antenna frequency (Mingo and Flowers, 2010). The wavelength of a given antenna frequency, λ , is a function of frequency f and the propagation velocity of the radar signal V :

$$\lambda = \frac{V}{f} \quad (2.2)$$

Vertical resolution is usually taken to be a minimum of one quarter of the radar signal's wavelength, but in practice one half of the wavelength is a better (more conservative) estimate (Hubbard and Glasser, 2005).

3 Methods

3.1 Study area

The 206 km² Milne Ice Shelf is located within Milne Fiord (82°35'N 80°35'W), between Cape Evans and Cape Egerton, along the northern coast of Ellesmere Island in the Canadian Arctic Archipelago (Figure 3.1). Milne Fiord has an average depth of 436 m, but there is evidence to suggest the seabed rises to within tens of metres of the surface under the outer region of the ice shelf (Hamilton, 2016). As a result, the ice shelf base may be grounded in spots (Hamilton, 2016). Seaward of the ice shelf, the sea bed deepens to greater than 600 m (Hamilton, 2016). The 55 km long, ~4 km wide Milne Glacier flows into the head of the fiord. The floating glacier tongue is separated from the ice shelf by the Milne Fiord epishelf lake, but they were once continuous (Mortimer *et al.*, 2012, Mueller *et al.*, 2017a). The ice shelf is composed of both glacial and sea ice; glaciers along the fiord walls still provide a small amount of glacial input (Mortimer *et al.*, 2012; Richer-McCallum, 2015).

Previous studies have determined that the Milne Ice Shelf has a mean thickness of 55 m and a maximum thickness of 94 m (Mortimer *et al.*, 2012, Figure 1.4). Seaward of the ice shelf, sea ice abutting the ice shelf has a thickness of 1-5 m (Mortimer, 2011). Ice thicknesses are greatest on the eastern side adjacent to Cape Egerton and thin toward the ice shelf edge (Jeffries, 1986; Narod *et al.* 1988; Mortimer *et al.*, 2012). The outer region of the ice shelf is characterized by rolls oriented parallel to the coastline with an average wavelength of 200 m and a maximum height from trough bottom to ridge depth of ~7.5 m (Jeffries, 1986). Dark blue areas on the ice shelf in Figure 3.1 are the meltwater ponds that form in the troughs of these ice shelf rolls every summer.

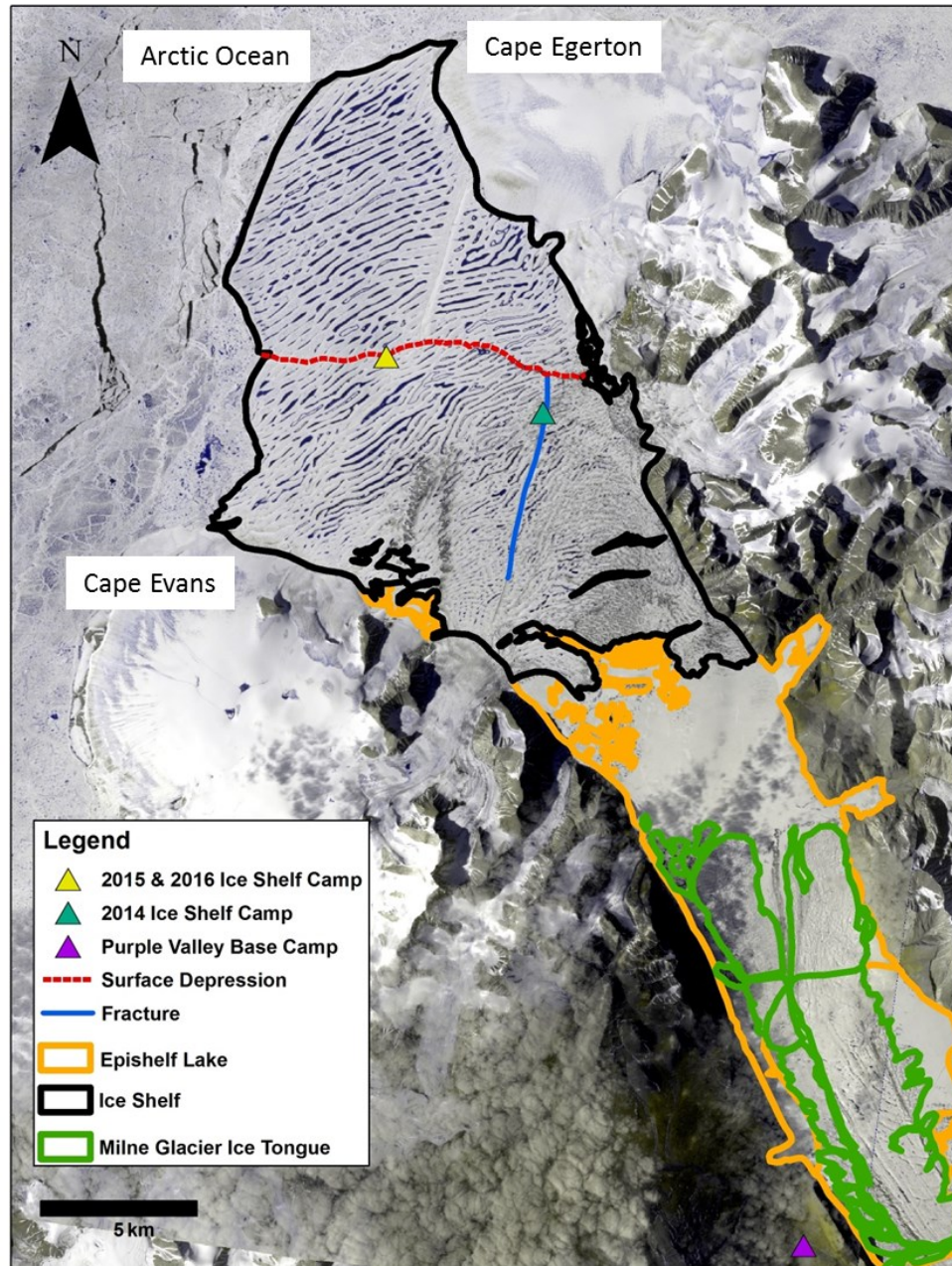


Figure 3.1 Map of Milne Fiord on the northern coast of Ellesmere Island, overlaid on an ASTER image from July 2016. The ice shelf is outlined in black, the epishelf lake is in orange and a portion of the floating tongue of the Milne Glacier is outlined in green. Triangles denote the locations of field camps occupied over the years of this study. The surface depression hypothesized to mark a basal channel is shown with a dashed red line. A fracture formed between 2008 and 2009 is outlined with a solid blue line. The hydrography and morphology of the channel and fracture were compared in this study. Dark blue meltwater ponds can be seen between the rolls on the ice shelf. There are several other linear features on the outer ice shelf, including a rehealed fracture dating to at least 1950 that can be seen running N-S from Cape Egerton to intersect the hypothesized channel.

The surface depression hypothesized to overlie a basal channel is found in this outer region (dashed red line, Figure 3.1). The curvilinear depression extends for 11 km, starting on the eastern margin of the ice shelf and extending west to the ice shelf edge. The morphology and hydrography of the hypothesized channel (hereafter referred to as ‘the channel’) were compared to those of a linear stress-fracture formed in 2009 (hereafter ‘the fracture’), which has since been infilled with ice (solid blue line, Figure 3.1). There are several other linear features on the outer region of the ice shelf, including a fracture dating to at least 1950 (Jeffries, 1986) that runs N-S from Cape Egerton and intersects the channel (Figure 3.1).

Fiordward of the E-W depression, the central part of the ice shelf has rolls that are more irregular in form and orientation, likely due to the influence of glacier inflow onto the ice shelf (Jeffries, 1986). Ice thicknesses in this region are more variable and thinner than the outer region (~50 m) (Narod *et al.*, 1988; Mortimer *et al.*, 2012, Figure 1.4). Notably, there is a very large area of thin ice (20 – 30 m) in the center of the ice shelf, just south of the hypothesized channel (Mortimer *et al.*, 2012, Figure 4.1).

Milne Ice Shelf dams the 71.2 km² Milne Fiord epishelf lake (Mueller *et al.*, 2017b). The lake is perennially covered by thin (<1 m) freshwater ice and is composed of a main body extending the width of the fiord, with arms that extend along the sides of the glacier tongue and pockets within the central part of the ice shelf. The epishelf lake is spatially uniform in depth, and is characterized by a layer of relatively warm, fresh (0-3°C, ~0.2 g kg⁻¹) water at the surface, separated from seawater (< -1°C, ~30 g kg⁻¹) by a sharp halocline only a few meters thick (Hamilton *et al.*, 2017). Seasonally, the lake deepens during the summer melt season (mid-June to mid-August) with meltwater input,

reaching a maximum depth in mid-August (Hamilton *et al.*, 2017). Once inflow ceases, the lake continues to drain under the ice shelf (Hamilton *et al.*, 2017). The lake reaches reaching a minimum depth in early June before beginning to refill again when melt recommences (Hamilton *et al.*, 2017). The epishelf lake warms over the melt season, peaking in mid-August (Hamilton *et al.*, 2017). Water temperatures in the epishelf lake gradually decrease over the winter but remain significantly above 0°C all year (Hamilton *et al.*, 2017). The epishelf lake has thinned over time from ~17.5 m depth when it was first measured in 1983 to 8.0 m in 2013 and the rate of thinning has increased over time coincident with increased air temperatures in the region (Hamilton *et al.*, 2017).

From the base of the epishelf lake to 50 m depth, seawater is influenced by interactions with ice and with subsurface glacier meltwater runoff, resulting in a water mass that is fresher (20 g kg⁻¹ to 34 g kg⁻¹) and up to 1°C warmer than water at equivalent depths offshore of the ice shelf ('fiord-modified water', Hamilton *et al.*, 2017). Below 50 m depth, water properties in the fiord are consistent with those offshore (Hamilton *et al.*, 2017). Cold, relatively fresh Pacific Water is found from 50 to ~200 m; below that is warm and saline Atlantic Water. The tides in the fiord are small, with a maximum range of 0.31 m (Hamilton *et al.*, 2017).

3.2 Field campaign overview

Fieldwork was conducted from July 12th to 27th 2014, July 6th to July 31st 2015, and July 11 to August 1st, 2016. Helicopter-supported fieldwork was conducted from a base camp at Purple Valley adjacent to Milne Fiord (82°42'N, 81°34'W) (Figure 3.1). Sampling on the ice shelf was also done from fly-in field camps on the outer ice shelf (adjacent to the

fracture at 82°70'N, 81°31'W in 2014; adjacent to the channel at 82°72'N, 81°66'W in 2015 and 2016).

During the field campaigns, IPR was used to map ice thicknesses along and across the channel and the fracture to characterize the size, shape and extent of these features. Conductivity-Temperature-Depth (CTD) profiles were collected through natural cracks and drilled boreholes in the channel and fracture to examine the properties of water flowing beneath the ice shelf and determine whether they were consistent with epishelf lake outflow. Current meters were deployed within the channel and fracture to measure water flow velocities. These data were also used to estimate discharge through the channel.

3.3 Characterization of feature morphology

3.3.1 Ice thickness surveys

An IPR unit developed by Blue Systems Integration Inc., as described in Mingo and Flowers (2010), was used to measure ice thicknesses and map the basal topography of the channel and the fracture in a common-offset survey configuration. The ruggedized, lightweight IPR receiver and transmitter units were ski-mounted and towed on foot, facilitating detailed surveys of a small area (Figure 3.2). The receiver and transmitter antennae were arranged in-line, with a fixed separation distance appropriate to the antenna frequency. The IPR receiver unit included an onboard GPS receiver which recorded location information concurrent with each IPR trace. In addition, a HiPer V Dual-Frequency GPS/GNSS receiver (Topcon Positioning Systems Inc.) mounted in front of the IPR receiver unit regularly recorded precise horizontal position and surface elevation.

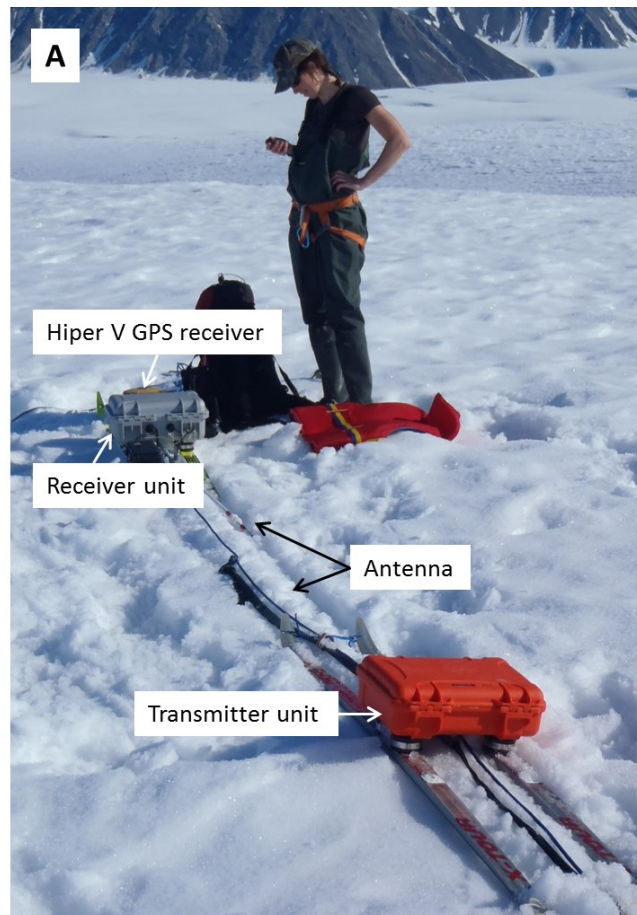


Figure 3.2 Panel A shows the field-ruggedized ice penetrating radar unit (IPR) used in this study. The transmitter and receiver were ski-mounted, in an in-line, common-offset survey configuration. The distance between antennae was adjusted as appropriate for the frequency used for a given survey. A Topcon Hiper V Dual-Frequency GPS receiver unit was mounted in front of the receiver and recorded precise horizontal positions and surface elevations along each transect. Panel B shows a survey in progress, with the front worker pulling the IPR unit and an additional person acting as a brake if required.

Along- and across-channel IPR profiles were acquired in four survey grids spaced along the channel in July and August 2014, 2015 and 2016 (grids A, B, C and D, Figure 3.3). Grid A was located at the seaward edge of the channel. Grids B, C and D were spaced along the channel with grid D at the far fiordward end of the channel. In 2014, profiles were taken at the fracture (grid E, Figure 3.3). Survey line locations were limited by where it was possible to walk back and forth across the channel and fracture; travel was limited by deep meltwater ponds or slush and by the presence of cracks in the ice spanning the fracture. Multiple cross-sectional profiles were gathered for each grid, and the cross-channel or cross-fracture lines extended to at least 100 m on either side of the channel and fracture.

Both a 50 MHz and 25 MHz antenna were used to image the ice shelf base (Table 3.1). For all surveys, the sampling rate was 2.5×10^8 samples s^{-1} . To improve the signal to noise ratio, each acquired trace was the average of 512 individual traces (stacking) (Hubbard and Glasser, 2005). The sampling interval of the Hiper V GPS receiver unit was set to match the IPR sampling interval. For the radar surveys using the 50 MHz antenna, the minimum detectable thickness (using $\lambda/2$) was equal to 1.7 m. For the 25 MHz antenna, it was 3.4 m. Ice thickness measurements were also taken manually through natural cracks and at boreholes at several locations in the channel and at the fracture (Figure 3.3).

Snow depth distribution was characterized along several IPR survey lines in grid D. Depths were measured using an avalanche probe with 5 cm markings along the length of the probe, at a variable spacing along the transects. It was determined during post-processing, however, that the temporal and spatial coverage of snow depth measurements

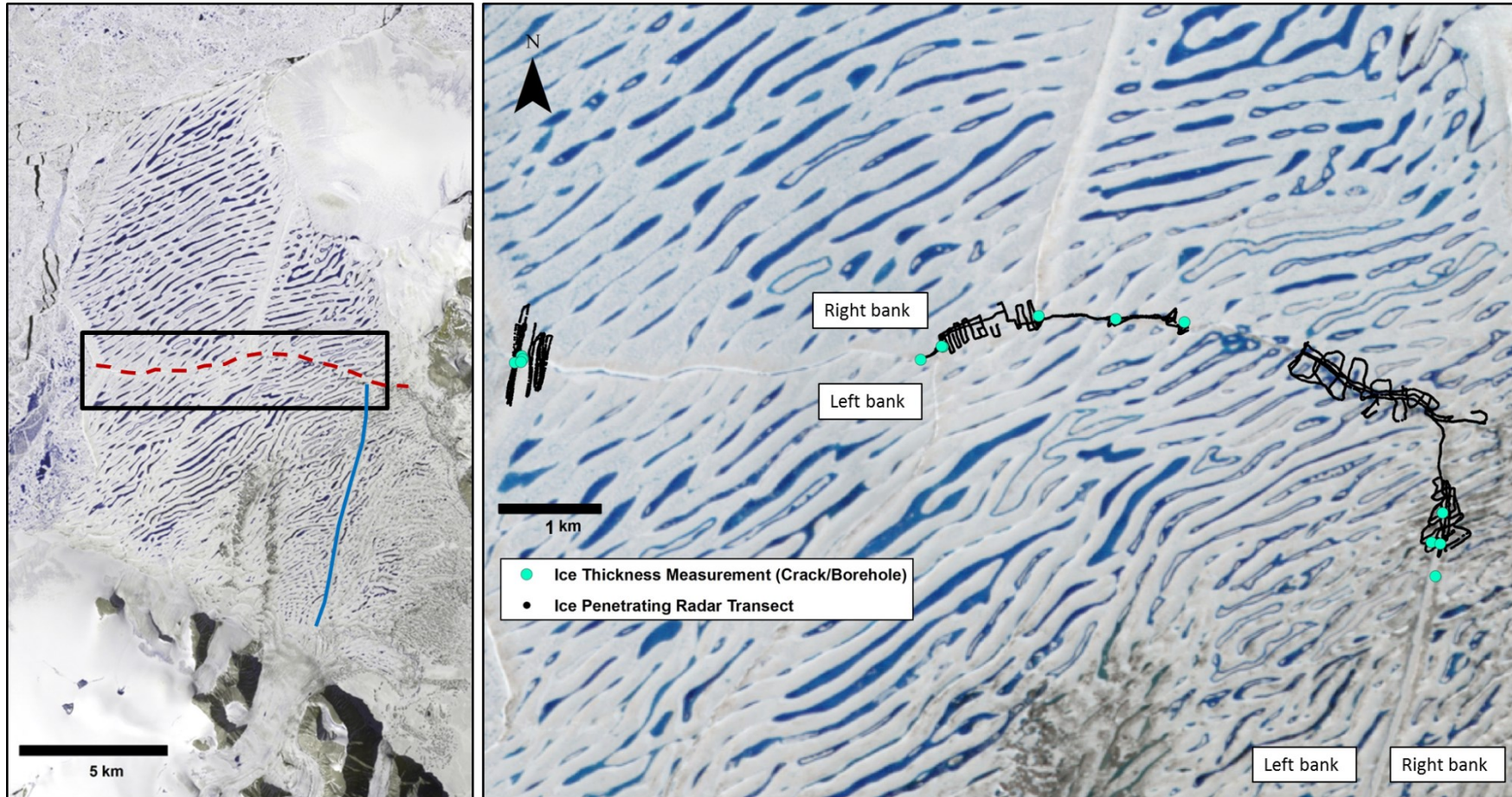


Figure 3.3 Ice penetrating radar survey grids along the channel (A, B, C and D) and the fracture (E). Each black line is an IPR transect line. Light green circles indicate the locations of ice thickness measurements taken in the channel or fracture through natural cracks or steam-drilled boreholes. Red dashed lines indicate the boundaries between survey grids. The left and right banks of the channel and fracture show the orientation of cross channel lines normalized to zero, where zero is the centerline of the feature. Locations to the left of the centerline have negative values for distance, while locations to the right of the feature centerline have positive distance values.

Table 3.1 *Antenna frequencies and settings for ice penetrating radar surveys of the channel (grids A-D) and the fracture (grid E).*

Grid	Antenna Frequency (MHz)	Antenna Separation (m)	Sampling Interval (s)
A	50	3	10
B	50 & 25	3 & 9	5
C	25	9	5
D	50	3	5
E	50	3	5

collected during the field campaign was insufficient to model and subtract snow cover from the total (snow plus ice) thicknesses recorded with the IPR. Therefore, thicknesses reported in this document are ice plus snow (if present). The uncertainty in thicknesses due to snow is discussed in Section 3.4.

3.3.2 Data processing

Positional data recorded by the Hiper V GPS receiver unit were post-processed for enhanced vertical and horizontal accuracy using the Canadian Spatial Reference System Precise Point Positioning (PPP) tool from Natural Resources Canada. The horizontal datum used to reference coordinates was NAD83 and the horizontal datum used to reference heights was the Canadian Geodetic Vertical Datum of 1928 (CGDV28). After correction, accuracy for horizontal positions was estimated at ± 0.03 m (95%, 2 standard deviations (SD)). Vertical position accuracy was ± 0.07 m (2 SD). Using the Radar Tools package (Wilson, 2013), readings from the on-board IPR GPS were replaced with the higher precision PPP-corrected Hiper V GPS positional data by matching time stamps.

PPP-derived elevations and ice thicknesses were corrected for the offset of the Hiper V GPS receiver unit from the ice shelf surface. Elevations were also corrected for tidal motion using tidal heights modelled using an 11-month record of water level collected in Milne Fiord between 01 July 2011 and 01 May 2012 (Hamilton, 2016). Anomalies from mean sea level were subtracted from surface elevation. The standard deviation of the residual between observations of tidal height and the model is ± 4 cm.

Radar Tools was used to post-process radar data to enhance the bed reflection and make the identification of the ice-water boundary easier. Stationary radar traces and empty soundings were removed. A dewow correction was applied to data to remove any

very low-frequency signal trend and reduce noise in the data. A linear gain filter was applied to data where required to enhance later returning reflections and assist in interpretation. Where required, a Stolt (F-K) migration was used on radargrams to restore dipping reflectors to their correct spatial positions (Annan, 2009).

The time of the wavelet first break was used as a reference for picking the surface and reflected waves. Selection of the location of the ice-water interface was done using a combination of the examination of individual traces; the pattern and spatial relationships across neighbouring traces; the radargram corrected for surface elevation, and theoretical ice-thicknesses calculated assuming the ice shelf was in hydrostatic equilibrium. For an ice shelf in hydrostatic equilibrium, the basal topography should roughly mirror surface topography. Therefore, in instances where there were multiple strong reflectors at the same location but different times, the theoretical ice thickness was used as a guide to selecting the correct reflector (i.e. to determine whether the shallower or deeper reflector should be selected). In cases where the bed reflection was uncertain or the data were too noisy to clearly determine the bed reflection, no pick was made.

Once the surface and basal reflectors had been picked wherever possible in all radargrams, two-way travel time associated with each pick was converted to ice thickness in metres using the equation:

$$T(m) = \sqrt{\left(\frac{\left(t + \left(\frac{s}{0.3}\right)\right) \cdot v}{2}\right)^2 - \frac{s^2}{4}} \quad (3.1)$$

where t is two-way travel time in ns, v is the radar wave propagation velocity and s is the transmitter-receiver antenna separation. According to the literature, the average velocity of a radar wave through ice is $1.67 \times 10^8 \text{ m s}^{-1}$, with slightly higher values for cold, dry ice

and slightly lower values for warm, temperate ice (Hubbard and Glasser, 2005). Previous studies on Ellesmere Island ice shelves have calculated a propagation velocity of 1.7×10^8 m s⁻¹ (Mortimer *et al.*, 2012) and 1.76×10^8 m s⁻¹ (Narod *et al.*, 1988). The velocity calculated by Narod *et al.* (1988), however, accounts for propagation through both ice and firn, through which radar wave velocities may be significantly faster (Clark and Bentley, 1994). Therefore, a radar wave propagation speed of 1.70×10^8 m s⁻¹ was used to convert measured two-way travel time to ice thickness for this study.

3.3.3 Cross-sectional form characterization, measurement and analysis

Cross-sectional ice thickness profiles were isolated and used to characterize channel and fracture geometry. Cross-sectional lines that were angled across the channel were corrected to perpendicular, to correct for any distortion of shape or measurements resulting from non-perpendicularity. Correction was done as follows: the centerline of the depression and fracture were digitized, based on the surface appearance of the features in RADARSAT-2 Fine Quad Mode images (pixel size 6.71 m) from the survey years. Then, straight lines perpendicular to the channel were defined for each location where an IPR line crossed the centreline, and the actual radar survey locations projected onto these lines. Cross-sections were normalized to the centerline, such that measurements to the left and right of the centerline were defined in terms of horizontal distance from the centerline (Figure 3.3). For the channel, the left bank (negative distances from 0) was defined looking in the down-channel (seaward) direction. For the fracture, the left bank was on the west (seaward) side of the fracture. Margins were defined both for the surface expression of the feature (elevation > 0 m asl) and for the basal expression (draft below 0

m asl), using the slope breaks along the base and the surface of the ice shelf (c.f. Rignot and Steffen, 2008).

Geometric variables measured for each corrected channel cross-section were: maximum basal width, maximum incision height, minimum measured ice thickness within the channel/fracture, upward slope of the sides from horizontal, ice thicknesses of the left and right banks, and the width and depth of the surface depression (Figure 3.4). For fracture cross sections, the penetration depth, minimum ice thickness, fracture width and the slope of the sidewalls from horizontal were measured (Figure 3.4). Summary statistics were calculated for all measured channel variables over each survey grid. The channel sidewalls were defined using the basal slope breaks and slope breaks identified at the crest of the channel. Angles for the left and right sides of the channel were calculated separately. Missing thicknesses were interpolated for every meter along the channel using a linear interpolation. Working from the channel margins to the center, the rise and run of each successive 1 m segment was calculated. This allowed for an examination of variability in slope along the channel walls. For each cross section, summary statistics were calculated for the individual slope segments, for each of the left and right sides. The mean sidewall slope angles reported here for each grid are the mean of the each cross-section mean slope; the standard deviation is the mean of the standard deviations for each cross-section.

To examine changes in surface and basal morphology between channel survey locations, variables were compared between channel survey grids. Differences in basal widths, surface widths, channel incision heights and mean slope of the channel walls between channel grids were assessed with a non-parametric Kruskal-Wallis rank sum

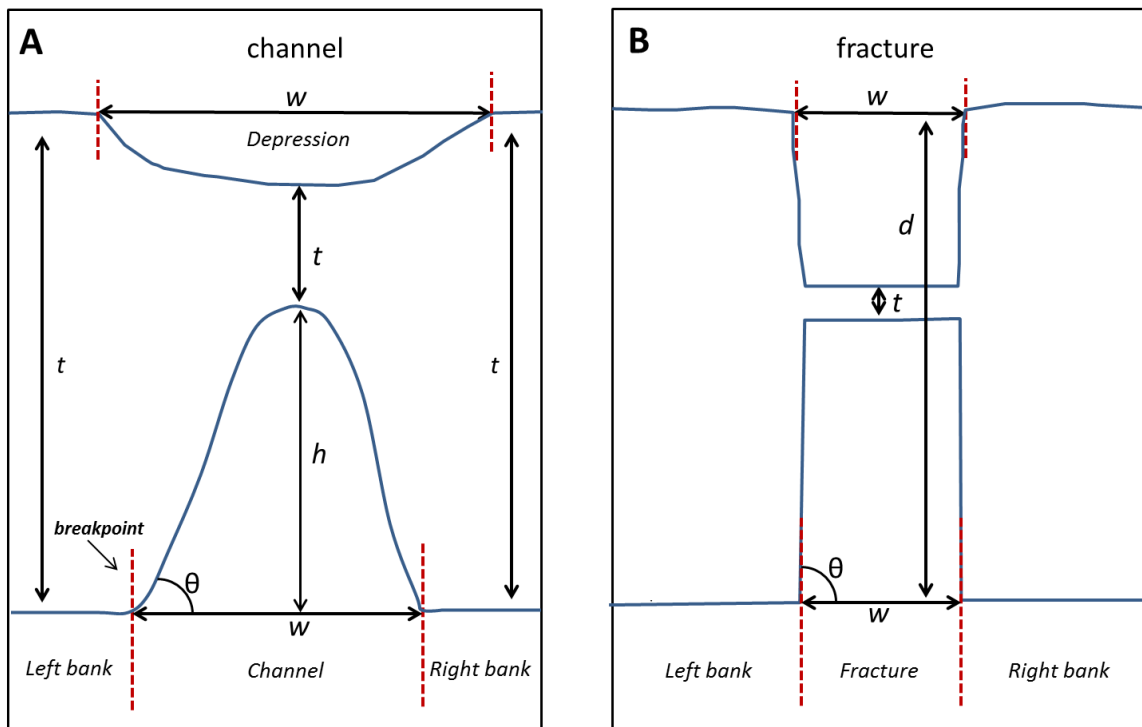


Figure 3.4 Schematics of an idealized channel ice thickness cross-section (A) and an idealized fracture ice thickness cross-section (B) showing the geometric variables measured in this study (not to scale). Slope breakpoints indicating the margins of the feature at the surface and at the ice shelf base are indicated by red dashed lines. For channel cross-sections, basal incision (h), basal and surface width (w), and the mean slope angle of each sidewall from horizontal (θ) was calculated. In addition, the thickness (t) of the ice on the left and right banks was measured, as well as the minimum thickness of the ice at the crest of the channel. For each fracture cross-section, the fracture penetration depth (d), minimum thickness of ice within the fracture, width of the fracture, and slope of the sidewalls up from horizontal was measured.

test. A post-hoc Neyemi pairwise comparison test was done to determine where differences occurred between groups. Differences in left and right bank thicknesses were tested for significance using a Wilcoxon rank sum test. A Student's t-test was used to assess whether there was a difference in mean slope on the left and right sides of the channel, within each grid. To compare channel and fracture morphology, the mean slope of the channel walls was compared to that of the fracture walls, to assess the hypothesis that the channel would have an inverted 'v' shape with sides that slope away from vertical while fracture sides would be near vertical. Variability in ice thickness within the channel was also compared with that of the fracture.

3.4 Ice thickness error estimation

There are several sources of measurement uncertainty that must be considered when determining the accuracy of ice thickness measurements reported here. Uncertainty in thickness measurements arises from uncertainty in the position of the surface and reflected waves, which in turn impacts the measurement of the waveform sampling interval and thus, the two-way travel time and calculated depth. Based on the sampling rate and radar wave velocity used in this study, the system uncertainty in thickness for this study is ± 0.68 m.

Uncertainty in thickness estimates also arises from operator error in picking the location of the reflected wave. To assess the impact of magnitude of picking errors, a cross-point analysis was conducted: all points from independent survey lines that were within a 4 m radius of each other were identified, and the difference in ice thickness between each pair of points was calculated. A total of 88 cross-points were identified. The median picking error from the cross-point analysis was 1.4 m (Table 3.2), with an

Table 3.2 Summary statistics for a cross-point analysis conducted to assess picking error in IPR survey data.

Number of points compared	Minimum (m)	First quartile (m)	Median (m)	Third quartile (m)	Maximum (m)	Standard deviation (m)
88	0	0.6	1.4	3.7	44.3	9.1

interquartile range of 3.1 m. Summing system uncertainty and the median uncertainty arising from errors in reflection picking, the uncertainty associated with ice thickness measurements in this study is ± 2.08 m.

There is also uncertainty in the reported thicknesses that result from neglecting the effect of differential radar wave propagation velocities through snow and through ice. As previously described, insufficient snow depth measurements collected during the field campaigns meant it was not possible to estimate or model snow cover on the ice shelf. It was also not possible to resolve the snow-ice boundary in the radar traces. Therefore, snow and ice were treated as one, and a radar propagation velocity of $1.70 \times 10^8 \text{ m s}^{-1}$ was used to convert two-way travel time to depth for the entire thickness measured.

However, the propagation velocity in snow is faster than in ice (Plewes and Hubbard, 2001). Thickness calculated from a two-way travel time measured by the IPR using the propagation velocity of a radar wave in ice would be less than if the faster velocity for snow were used. The maximum snow depth measured along the IPR transect was 2.6 m. Using a snow depth of 3 m, the difference in thickness when using a radar wave velocity in snow of $2.00 \times 10^8 \text{ m s}^{-1}$ (c.f. White *et al.*, 2015) to account for the snow thickness, compared with using only the velocity in ice of $1.70 \times 10^8 \text{ m s}^{-1}$, is 0.5 m. Therefore, by assuming the entire column is ice, the thicknesses reported here may underestimate thickness by up to ~ 0.5 m in places where there was appreciable snow. A very conservative estimate of uncertainty in ice thickness measurements in this study is then total uncertainty as calculated above, plus 0.5 m due to snow, for a total of ± 2.58 m.

3.5 Hydrography

3.5.1 Conductivity-temperature-depth profiling

Conductivity-temperature-depth (CTD) profiles were collected to examine the structure of the water column. Profiles were collected through leads in the sea ice offshore of the ice shelf and through boreholes and natural cracks through the ice shelf and epishelf lake ice. Profiling locations were accessed by foot or helicopter. Profiles were taken at two locations within the channel in 2015 and in 2016, to enable examination of change in water properties along the channel (sites 1 and 2, Figure 3.5). Profiles were taken at the fracture in all three years of the study. Profiles were also collected in the epishelf lake and offshore of the ice shelf, to enable comparison of the water column structure at these locations with those of the channel and fracture (Figure 3.5).

The profiles were recorded using a 6 Hz XR-620 CTD (RBR-Global Ltd.) and an 8 Hz Ocean Seven 304 Plus CTD (OS 304Plus, Idronaut S.r.l.). At each sampling site, CTDs were left to equilibrate for at least 1 minute in the water, and lowered through the water column at a rate of $\sim 0.5 \text{ m s}^{-1}$. CTD casts were full depth, to the bottom of the fiord. However, it is the near-surface water column that is of interest here, so only the top 50 m of the profiles are presented herein. The temperature sensor of the OS 304Plus has an accuracy of $\pm 0.002^\circ\text{C}$ with a resolution of 0.0001°C . The pressure sensor accuracy is $\pm 0.05\%$ F.S. (full scale) with a resolution of 0.0015% F.S. and conductivity measurements are accurate to $\pm 0.003 \text{ mS cm}^{-1}$ with an instrument resolution of $0.0003 \text{ mS cm}^{-1}$. For the RBR XR-620, the accuracy of the temperature sensor is $\pm 0.002^\circ\text{C}$ with a resolution better than 0.00005°C . Conductivity is accurate to 0.003 mS cm^{-1} with a

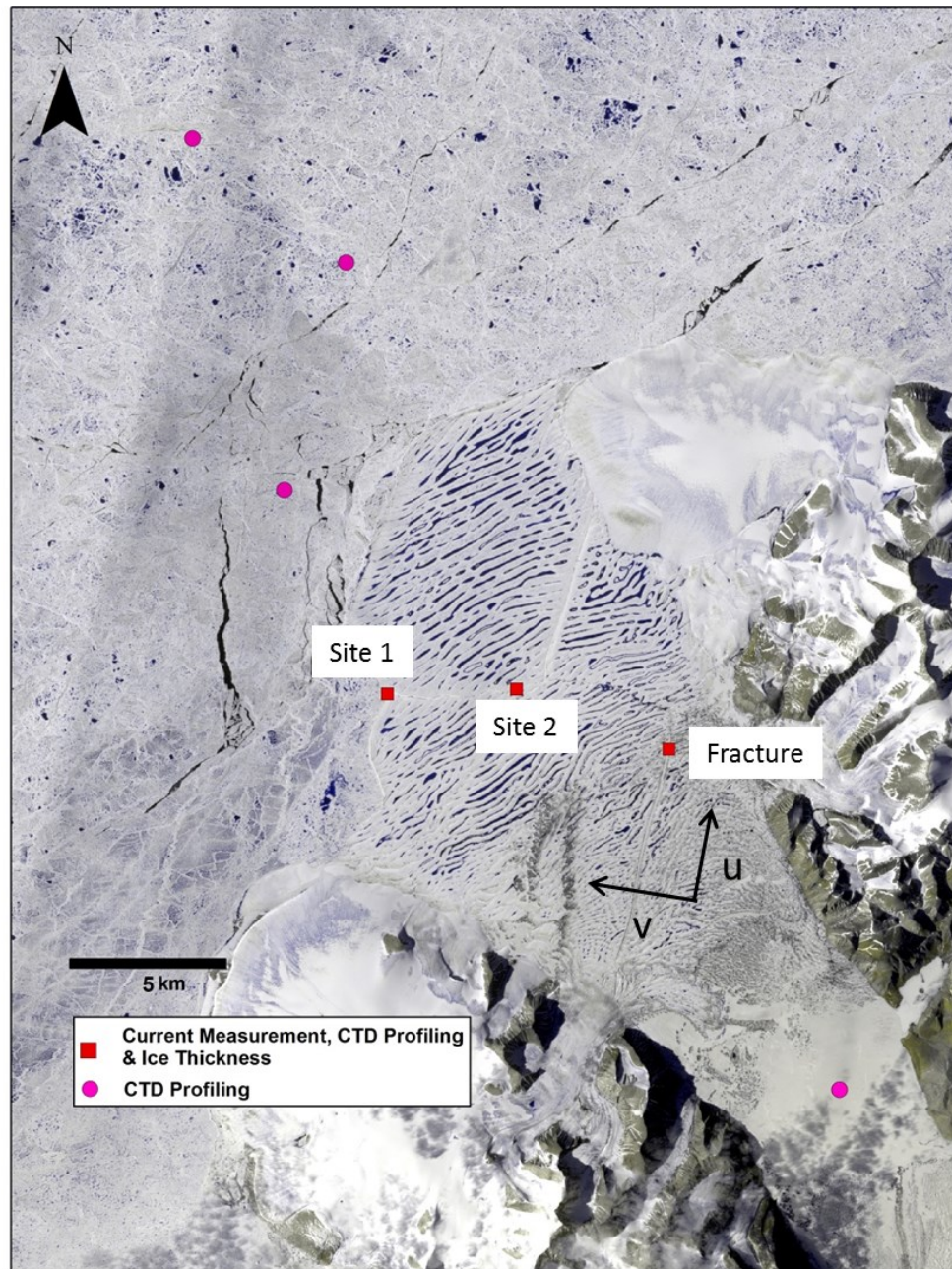


Figure 3.5 Locations of hydrographic measurements in this study. Pink circles indicate conductivity-temperature-depth (CTD) profiles. CTD profiling was done every year of the study in the epishelf lake, as well as in three different locations offshore of the northern edge of the ice shelf. CTD profiling, as well as current measurements were done at two sites in the channel and at one site in the fracture. Site 1 was at the seaward edge of the channel; site 2 was further up channel. Current measurements were done with a point current meter in the channel and an Acoustic Doppler Current Profiler (ADCP) in the fracture. The 'u' axis of the ADCP was oriented along the channel, with positive 'u' pointed northeast. The 'v' axis was oriented across the fracture, with positive 'v' pointed northwest.

resolution of $0.0005 \text{ mS cm}^{-1}$. The accuracy of the pressure sensor on the XR-620 is better than $\pm 0.05\%$ F.S

3.5.2 CTD profile data processing

For each profile, the downcast was isolated and any measurements taken within ice (e.g. in a borehole and so not exposed to the ambient water column) were removed. Instrument pressures were corrected for atmospheric pressure. Further processing and plotting were done in R using the *oce* package (Kelley and Richards, 2016): pressures were converted to depth, and the square of the Brunt-Väisälä buoyancy frequency, N^2 , was calculated as a measure of water column stratification. Additionally, Absolute Salinity (S_A , g kg^{-1}) and Conservative Temperature (Θ , $^{\circ}\text{C}$) were derived from Practical Salinity and in-situ temperature using the Gibbs Seawater TEOS-10 formulation (McDougall and Barker, 2011). As per Hamilton *et al.* (2017), the depth of the epishelf lake was defined as the depth of the stratification maximum (maximum N^2). Absolute Salinity and Conservative Temperature were plotted against depth to examine the structure of the water column at each profile location.

3.5.3 Current velocities

3.5.3.1 Channel measurements

Water speed with depth in the water column was measured in the channel using an Infinity AEM-USB electromagnetic point current meter (JFE Advantek Co. Ltd) with a resolution of 0.02 cm s^{-1} and accuracy of $\pm 1 \text{ cm s}^{-1}$. Current profiling was done at the same sampling locations in the channel as the CTD profiles (Figure 3.5). To profile, the current meter was attached to a line above one of the CTD instruments and the instruments were lowered in increments through the water column, to a depth of at least

25 m. Current speed was recorded for 2 minutes at each depth sampled. The sampling rate for all profiles with the current meter was 10 Hz.

For analysis, current meter data were matched with the CTD to obtain the exact depth associated with water speed measurements. First, the CTD data were adjusted for atmospheric pressure and for the offset between the pressure sensor and current meter. Due to the difference in sampling rates between the instruments, data from both instruments were averaged to one second intervals. Then, current speed and depth measurements were matched by time stamp. The first and last 20% of the current speed measurements recorded at each depth bin were removed to eliminate the possibility of readings taken while the instrument was being lowered into or out of position. This issue was due to a loss of synchrony between times recorded by the CTD, the current meter, and in field notes. The remaining values were averaged to obtain a mean current speed for each depth bin. Two profiles were completed at site 2, one after the other and current speed was recorded at slightly different depths in both profiles. To improve the depth resolution for current speed, the two profiles were merged.

3.5.3.2 Fracture

Water velocity with depth was measured in the fracture using a 4-beam 300 kHz Sentinel V100 Acoustic Doppler Current Profiler (ADCP, Teledyne Rd Instruments, Inc). ADCPs are used to measure current velocity throughout a column of water, providing a time series of flow over a series of binned depths. The ADCP was installed with a fixed orientation and deployed looking downward through the water column. The instrument transducers sat at a depth of 0.6 metres below the water surface. Measurement took place over 34 hours starting in the morning of July 14th, 2014. The ADCP bin size was 1.5 m,

with the center of the first bin at 2.33 m and the last at 100 m. The ADCP recorded an ensemble at 10 minute intervals, with 100 pings per ensemble at a rate of one ping per second. The instrument velocity measurement accuracy is $\pm 0.5\%$ of the water velocity relative to the ADCP, $\pm 0.5 \text{ cm s}^{-1}$. Velocity resolution is 0.1 cm s^{-1} .

ADCP data were processed using the ‘oce’ package in R. Coordinates were transformed from beam coordinates to instrument (xyz) coordinates. The ‘u’ axis was oriented along the fracture, roughly cross-fiord with positive u pointed north, and the ‘v’ axis was oriented across the fracture, with positive v pointed west, down-fiord (Figure 3.5). Data were screened for accuracy using a correlation threshold of 64 and for returned signal strength using an echo intensity threshold of 40 (RD Instruments, 2011). Data were also screened for consistency in the velocity measurements; any velocities with an associated error velocity greater than 2 m s^{-1} were rejected (RD Instruments, 2011). Finally, an ensemble mean velocity was calculated for each sampling interval from individual ping measurements. Mean velocity over the entire sampling period was plotted for each depth bin, for both the u and v axes, to examine velocity with depth at the fracture site in both the along-fracture and along-fiord directions.

3.5.4 Estimation of discharge

The geometry of the cross-sectional ice thickness profiles closest to each of sampling sites 1 and 2 were used to calculate the cross-sectional area of the channel over which flow occurred. For each site, the channel cross-section was divided into 1 m horizontal segments over the depth range of measurements made with the current meter; an example for site 2 is shown in Figure 3.6. For each segment where a current velocity measurement had been made within the depth range encompassed by that segment, that velocity value

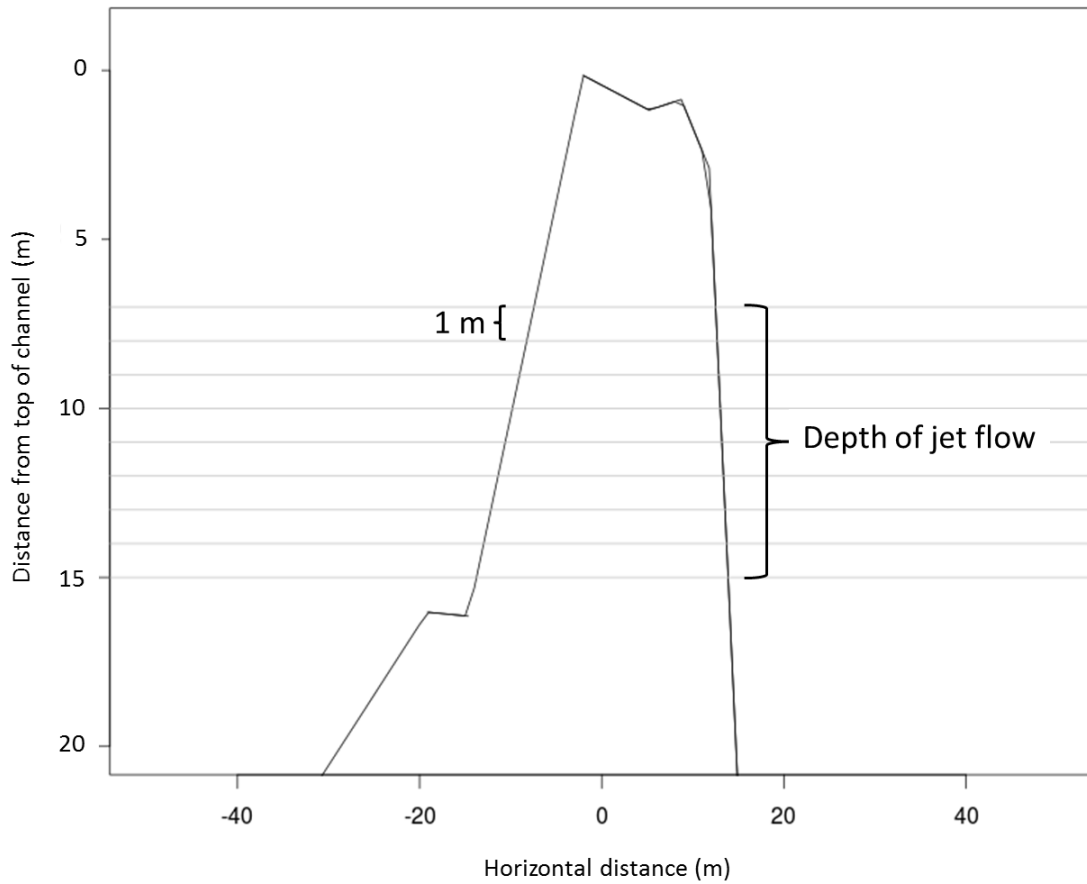


Figure 3.6 Schematic showing how channel cross-sectional geometry was used to calculate discharge, using the cross section and depth of flow for site 2. The channel was divided into 1 m horizontal segments over the depth where current measurements were available. The area of each segment was computed by parameterizing the segment as a trapezoid. Discharge was calculated for each segment and then summed to get total discharge through the channel.

was assigned to the segment. Where no measured velocity was available for a given segment, the mean velocity of the previous and successive velocity readings was used. If two measurements had been made within the 1 m depth range, the mean velocity of the two was taken. Segments were determined to be within the region of flow if their assigned velocity was $>0.05 \text{ m s}^{-1}$. This criterion was chosen based on a visual assessment of the plots of velocity with depth for each sampling site.

The area of each segment with an assigned flow velocity of at least 0.05 m s^{-1} was calculated by parameterizing the cross-sectional area of flow as a trapezoid:

$$A = h \left(\frac{b1 + b2}{2} \right) \quad (3.3)$$

where A is cross-sectional area (m^2), h is the height of the segment (1 m), $b1$ is the minimum width of the segment (m) and $b2$ is the maximum width of the segment. Discharge (Q) for each segment was calculated using the segment area (A) and the assigned flow velocity for that segment (V):

$$Q = A \times V \quad (3.2)$$

Discharge was summed over all segments for each site for total discharge through the channel at sites 1 and 2.

4 Results

4.1 Ice thickness survey overview

Over the three field campaigns for this study, ~40 km of surface elevation and ice thickness transects were completed, covering 5.5 km of the ~11 km long channel and 800 m of the ~7 km long fracture (Figures 4.1 and 4.2). Grid A had the lowest percentage of traces for which the ice-water reflector was identified (63%, compared to >75% in other grids) (Table 4.1). The ice shelf basal topography generally mirrored surface elevation as the lowest elevation surface areas corresponded to areas with the thinnest ice. Thin ice is seen along the length of the channel (grids A-D, Figure 4.2) and within the fracture (grid E). Within the channel, ice was consistently thinnest in grid A (<5 m). The ridges and troughs of the characteristic rolls on the ice shelf surface were also captured in the thickness data presented here. This effect was most prominent in the vicinity of the fracture, where survey lines across the fracture followed along these ridges and troughs: lines of thin ice (troughs) can be seen alternating with thicker ice (ridges) extending on either side of the fracture (box E, Figures 4.1 & 4.2).

Over the entire survey, the mean ice thickness was 41 m, with a minimum of 1 m and maximum of 68 m. Ice thicknesses less than 3.4 m thick (25 MHz) and 1.7 m (50 MHz) are artefacts and represent errors in picking the correct location of the basal reflector, because, as described previously, they exceed the minimum vertical resolution possible with the respective antennae. The mean surface elevation was 4.37 m, and the maximum was 8.89 m. The lowest surface elevation recorded was -0.86. Elevations below sea level, however, are likely erroneous and attributed to a datum-related error; as discussed in Chapter 5.

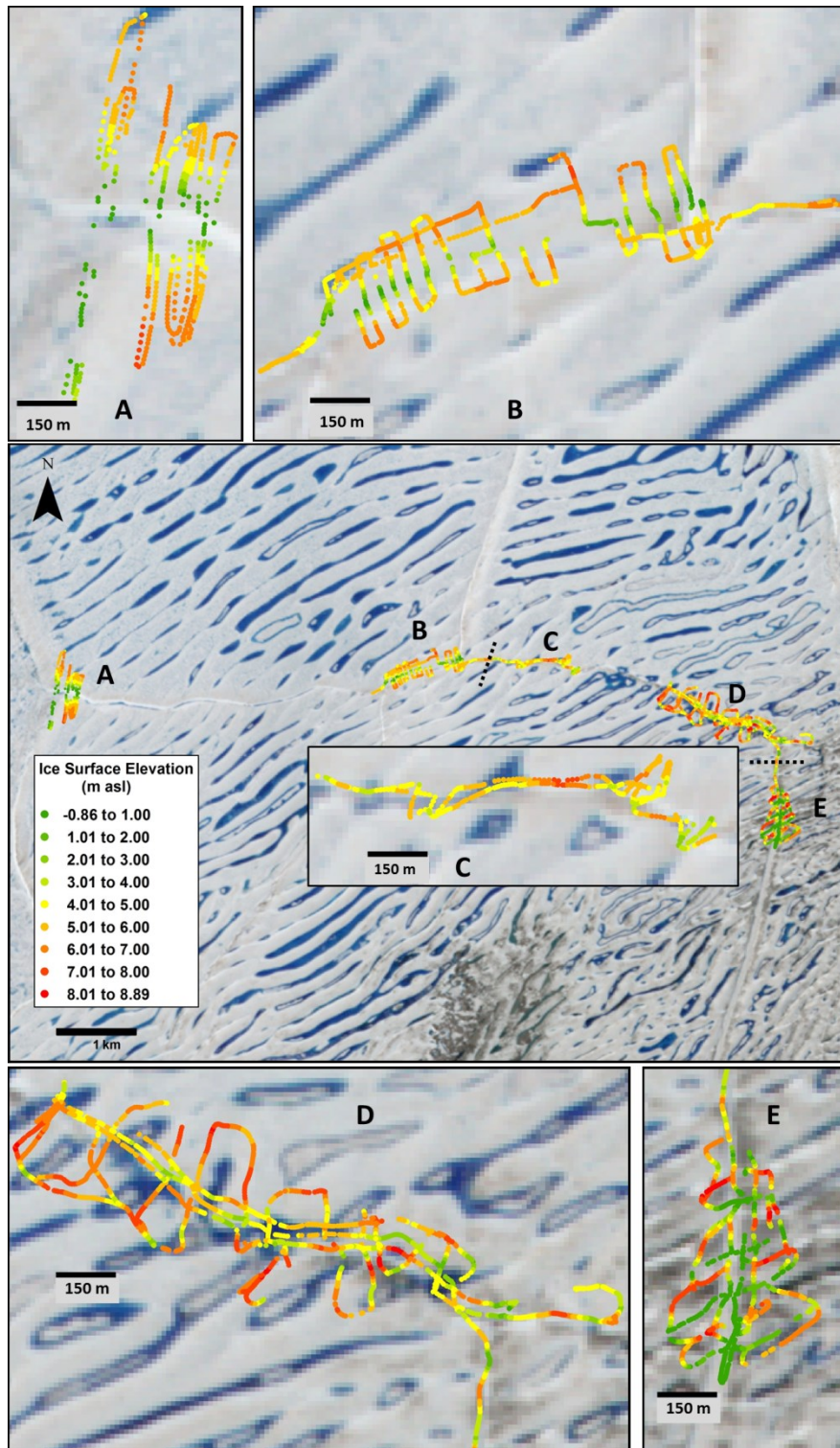


Figure 4.1 Map of point surface elevation measurements along IPR transect grids from a Dual Frequency GNSS receiver unit post-corrected with Precise Point Positioning. Data are overlaid on a July 2016 ASTER image of the Milne Ice Shelf. Grids are labelled by letter on the map and inset boxes, black dashed lines indicate boundaries between grids.

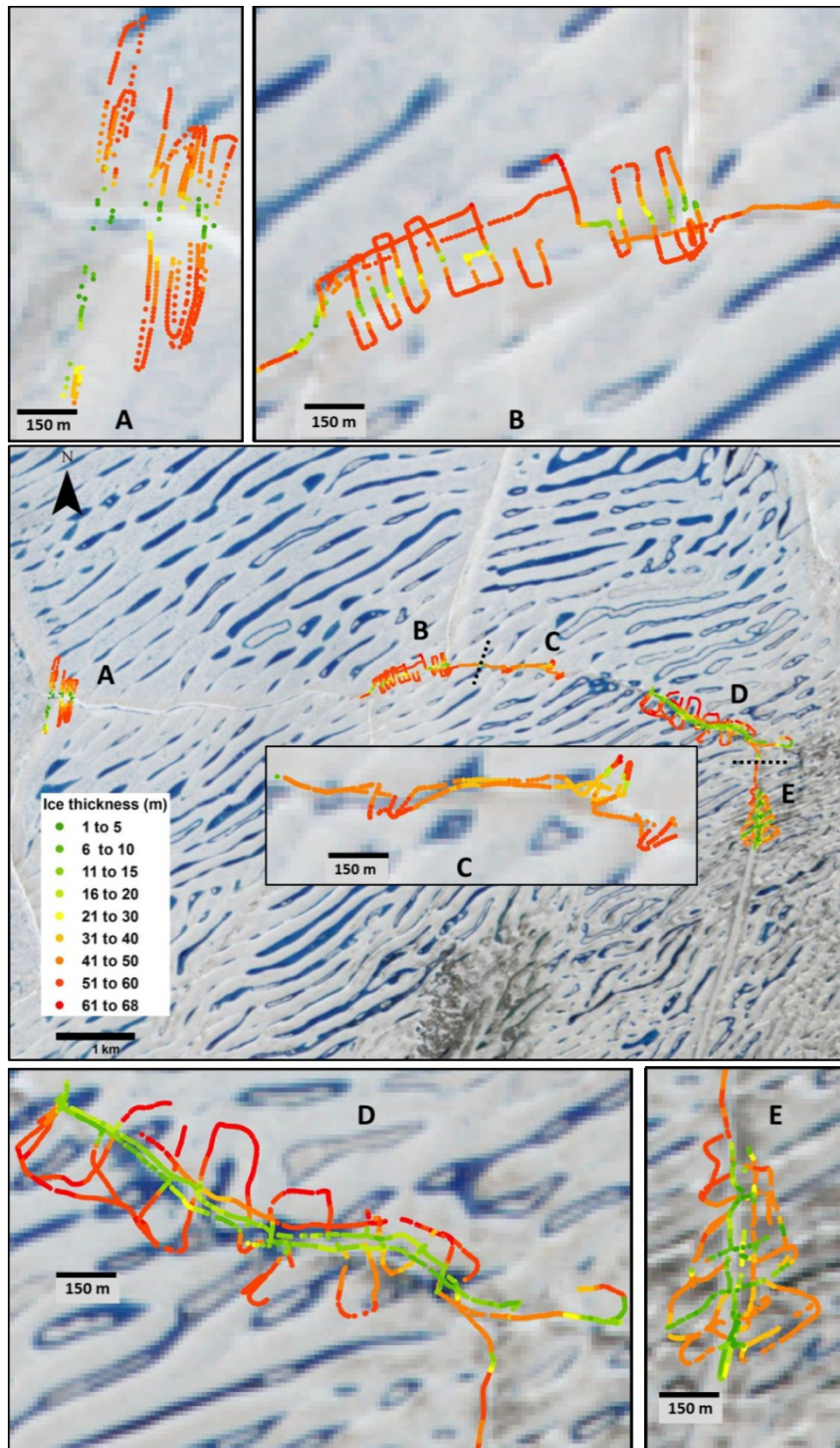


Figure 4.2 Map of ice thicknesses measured along IPR transect grids. Data are overlaid on a July 2016 ASTER image of the Milne Ice Shelf from July. Grids are labelled by letter on map and inset boxes; black dashed lines indicate boundaries between grids.

Table 4.1 Total number of IPR traces recorded and number of traces where the ice-water reflector could be identified, by survey grid.

Grid	Total number of recorded traces	Number of traces where ice-water interface was picked (as % of total)	Number of complete cross sectional profiles in grid
A	672	425 (63%)	7
B	2287	1898 (83%)	8
C	347	295 (85%)	3
D	2322	2047 (88%)	4
E	1116	836 (75%)	4

Figure 4.3 shows a typical radargram from a cross-channel IPR transect. The continuous black line seen at ~600 ns marks the ice surface. The strong, bright reflector arriving later (~1400 ns on the left side of the profile) is the ice-ocean interface. The basal channel can be seen cutting upward into the base of the ice shelf between traces 45 and 85, interrupting the continuous basal reflector. Where the ice shelf is sloped along the walls of the channel, accurately identifying the base of the ice is difficult due to noise from multiple off-nadir returns and absent reflections, as seen in Figure 4.3. Therefore, there are relatively few ice thickness measurements available from the sidewalls of the channel in the cross-sectional profiles.

4.2 Channel morphology

In total, 22 complete channel cross-sections across the channel were identified (Table 4.1). There were four fracture cross-sections. These cross-sections were used to characterize channel and fracture morphology (Table 4.2). For four of the cross-sections from grid A, there were no picks made between the breakpoints defining the channel banks, so channel height was only calculated using three of the seven cross sections.

The cross-sections from the channel all show a deeply-incised feature with sloping sidewalls located beneath the E-W surface depression (Figure 4.4). Away from the edge of the ice shelf, in grids B, C and D, basal width and incision height were fairly consistent (Figure 4.4, Table 4.2). Mean channel widths ranged from 57 to 86 m and the mean channel incision height across all three grids was 42 m, or 77% of the mean ice shelf thickness of 55 m reported by Mortimer *et al.* (2012). Channel height decreased in the down-channel direction. The channel was significantly broader and less deeply incised at the seaward edge, in grid A, than it was at the grids up-channel

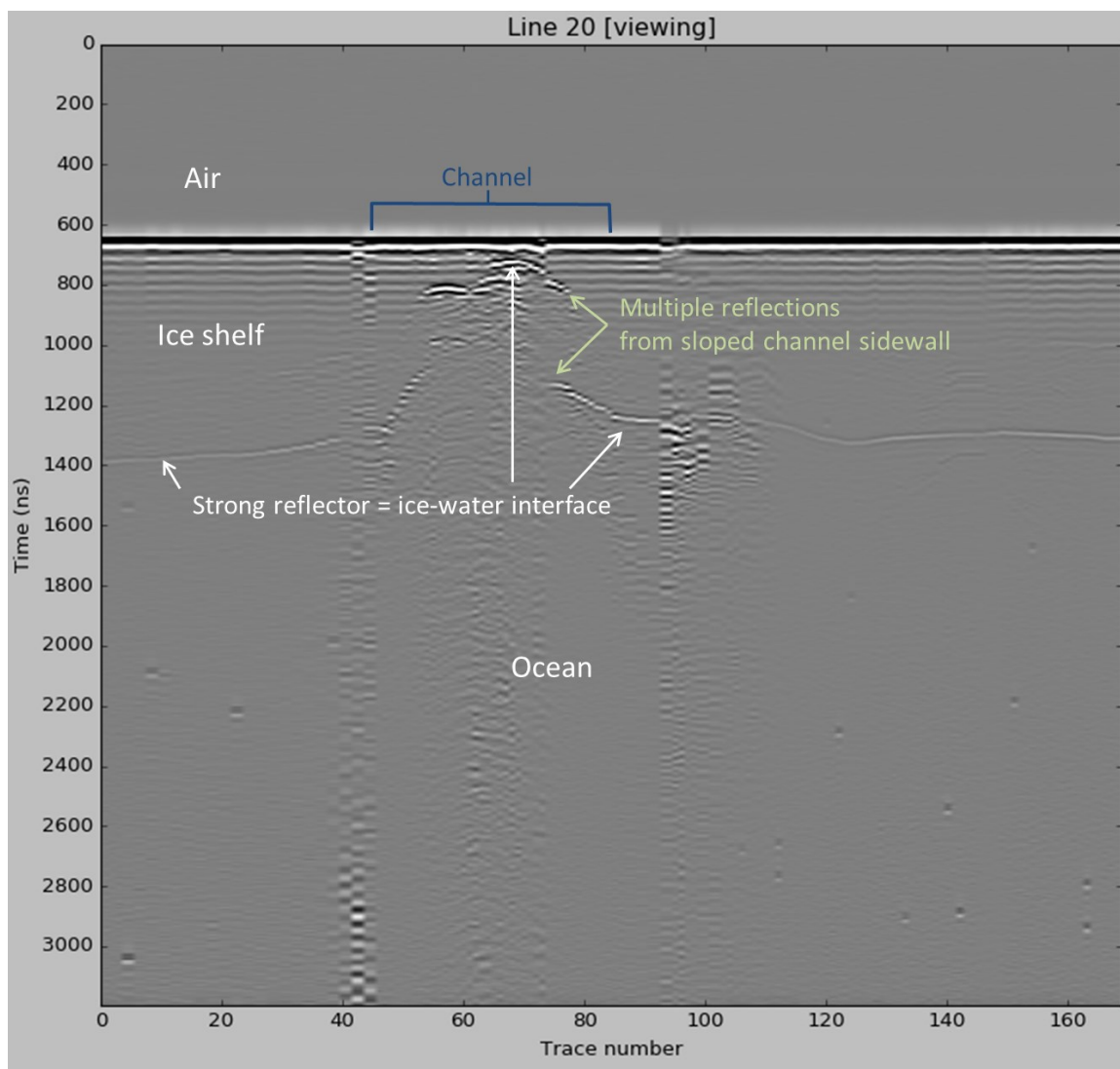


Figure 4.3 A radargram from a cross-channel profile in grid D. Multiple radar traces are aligned side by side in a radargram, in order to show variation in the subsurface over horizontal space. The continuous black line just below 600 ns is the ice surface. The bright reflector at 1400 ns is the ice shelf-ocean interface. The channel can be seen in the ice shelf from trace 45 to 90. On the sides of the channel, there are places where no reflector can be seen or where identifying the correct reflector was not possible, due to multiple reflections due to off-nadir reflections from the angled sidewall.

Table 4.2 Basal and surface morphology metrics calculated from all complete ice penetrating radar cross-sectional profiles across the channel (grids A to D) and fracture (grid E).

Grid	Mean width ± 1 SD (m)	Mean height ± 1 SD (m) (as % of total)	Minimum ice thickness (minimum draft)	Mean ice thickness left bank ± 1 SD (m)	Mean ice thickness right bank ± 1 SD (m)	Mean surface width ± 1 SD (m)	Mean surface depth ± 1 SD (m)	Mean sidewall slope angle ± 1 SD ($^{\circ}$)
A	164 \pm 12 n = 7	32 \pm 2 (58) n = 3	3(3)	51 \pm 7	48 \pm 6	320 \pm 12 n = 7	6 \pm 1 n = 7	32 \pm 15
B	86 \pm 12 n = 8	39 \pm 3 (71) n = 8	6(6)	51 \pm 4	52 \pm 6	68 \pm 4 n = 5	3 \pm 1 n = 5	43 \pm 21
C	57 \pm 8 n = 3	43 \pm 2 (78) n = 3	10(9)	40. \pm 2	59 \pm 2	NA	NA	61 \pm 22
D	82 \pm 7 n = 4	45 \pm 4 (82) n = 4	10(5)	52 \pm 5	61 \pm 3	96 \pm 30 n = 2	3 \pm 1 n = 2	40 \pm 11
E	69 \pm 21 n = 4	43 \pm 4* (100) n = 4	4(3)	–	–	–	–	78 \pm 6

* for the fracture, mean depth was calculated, using the height of both sidewalls

Metrics not calculated for the fracture are marked with –

NA indicates metric could not be calculated

Uncertainty associated with ice thickness measurements in this study is ± 2.58 m

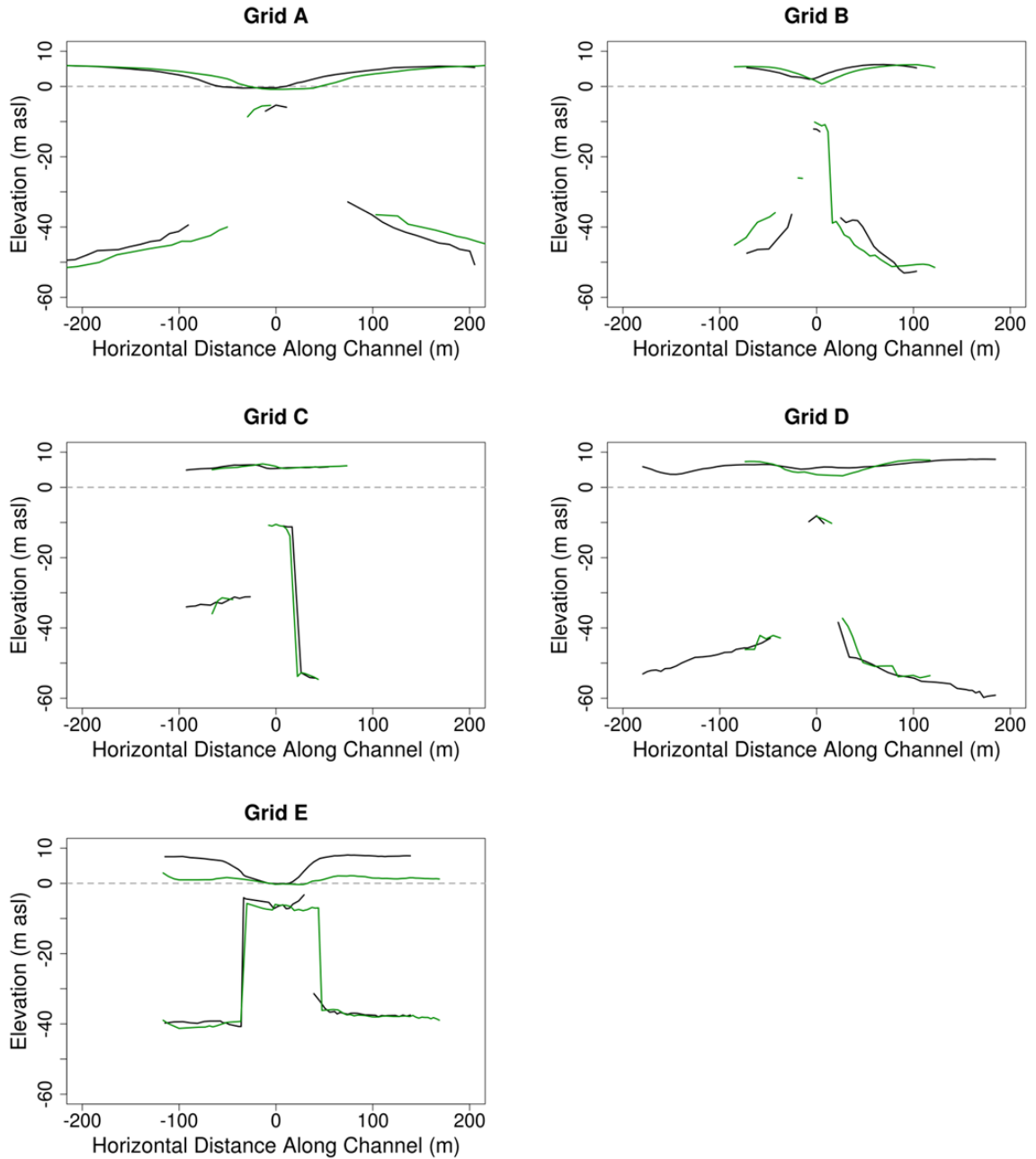


Figure 4.4 Two representative cross-sectional ice thickness profiles (one plotted in green, one in black) from cross-channel (grids A to D) and cross-fracture (grid E) transects. Channel profiles run from the left (negative) to right (positive) where the left is defined in the downstream direction and zero corresponds to the centerline defined along the channel at the surface of the ice shelf. Fracture profiles run from north (negative) to south (positive) across the fracture; zero corresponds to the fracture centerline. Plots of channel and fracture cross-sections not shown here are provided in Appendix A.

($\chi^2_{\text{width}} = 17.52, p < 0.001$; $\chi^2_{\text{height}} = 14.99, p = 0.001$). The minimum ice thickness at the crest of the channel was in grid A (3 m) and thickness increased up channel to grid D (10 m) (Table 4.2). The maximum draft (ice < 0 m asl) measured in the channel was 9 m, at grid C.

The mean slope of the channel sidewalls, averaged across the left and right sides of the channel, ranged from 32° at grid A to 61° at grid C (Table 4.2). The surface depression was widest (320±12 m) and deepest (6±1 m) at grid A, and narrower and shallower away from the ice shelf edge, consistent with the patterns noted in basal morphology. There was considerable variability in surface morphology along the channel. The depression was consistently narrow in grid B (68±4 m), but highly variable in grid D (96±30 m). Notably, there was no appreciable depression at the surface of the ice shelf overlying the channel in grid C.

A striking feature of the cross-sections was the asymmetrical nature of the profiles from grid C and, to a lesser extent, grids B and D. Ice thicknesses on the left bank of the channel were significantly less than ice thicknesses on the right bank in grids B ($W = 2671.5, p = 0.009$), C ($W = 110, p < 0.001$) and D ($W = 312, p < 0.001$) (Table 4.2). The mean slope of the channel sidewalls in grid C also differed on the left and right sides. The mean slope of the left channel wall at grid C was 42°, consistent with sidewall slope angles at grids B and D but the right wall of the channel was much steeper, with a mean slope of 80° (Figure 4.5). There were no significant differences in slope between the left and right sidewalls of the channel in grid A ($t = -0.49, p = 0.65$), B ($t = -0.67, p = 0.51$) or D ($t = -0.44, p = 0.68$) (Figure 4.5). While mean sidewall slope angles were fairly consistent between grids, there was substantial variability in slope angle along each

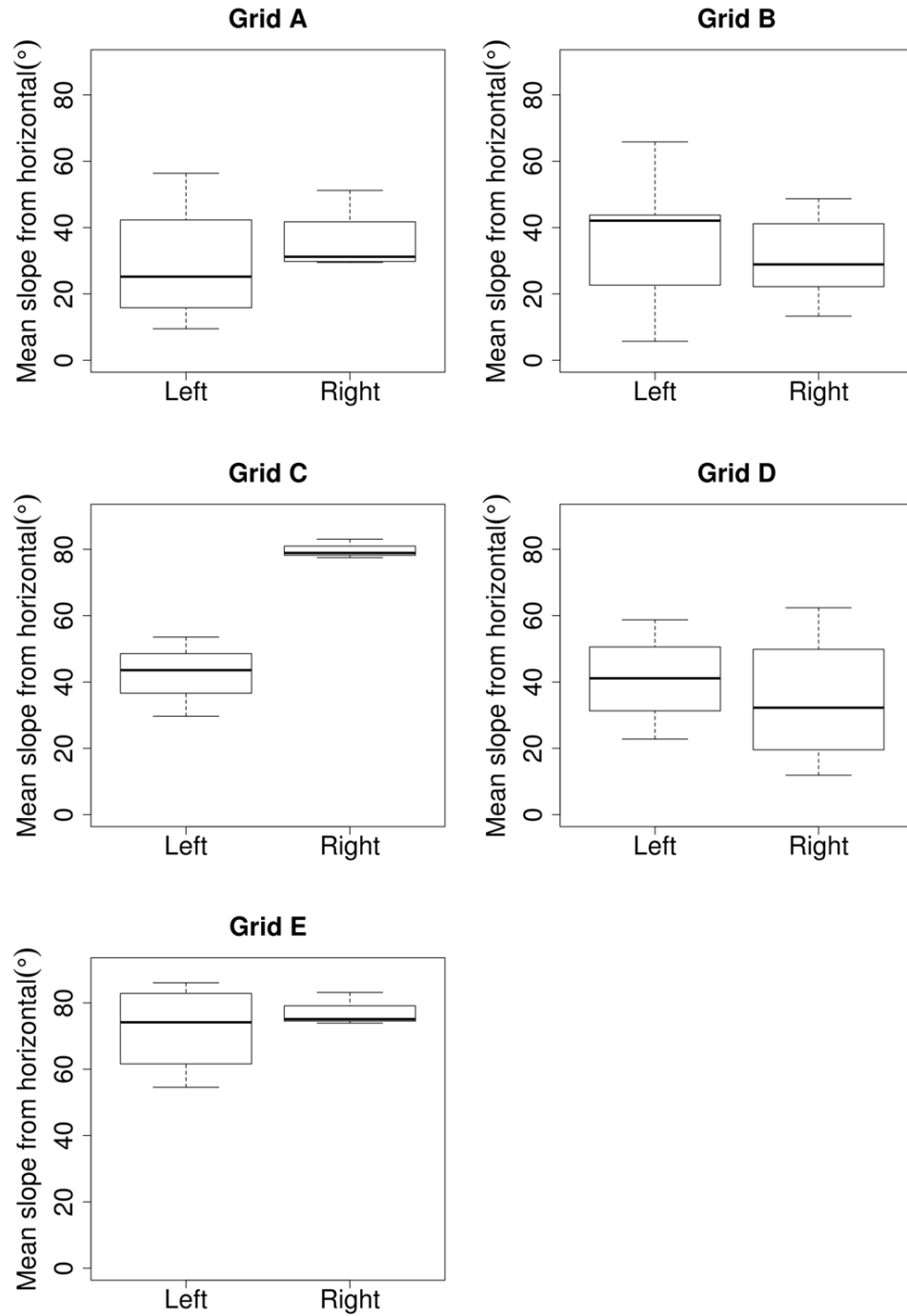


Figure 4.5 Boxplots showing variability in mean sidewall slope angle up from horizontal, calculated for each of the left and right sides of each cross-section, by grid. The right side of the channel is substantially steeper at grid C, whereas there is no significant difference in slope angle between the left and right sides for any other grid. The plot for grid E shows that sidewall slope angles on both sides of the fracture are consistently much steeper than those of the channel.

segment of the channel walls in individual cross sections, reflected in the standard deviation (Table 4.2). Variability in the sidewall topography can also be seen in the plotted cross-sections (Figure 4.4): there appear to be ‘steps’ incised into the channel walls in the profiles from grid B near the base of the channel.

4.3 Comparison of fracture and channel morphology

The sidewalls of the fracture were substantially, and consistently, steeper than those of the channel, with a mean slope angle of $78\pm 6^\circ$ (Table 4.2, Figure 4.5). Median ice thickness in the fracture was 7 m (Figure 4.6), and ice thicknesses across the width of the fracture were fairly consistent whereas channel ice thickness increased rapidly away from the middle of the channel (Figure 4.4). The fracture was through the full ice shelf thickness. The width of the fracture was quite variable in the cross sections surveyed (Table 4.2). The cross-sections plotted in Figure 4.4 (grid E) illustrate an instance of a transect along the crest of a ridge (higher surface elevation, black line) and a transect along a trough between rolls (lower surface elevations, green line). The plotted cross-section also show an instance where thin ice in a trough is not echoed at the base of the ice shelf (green line) though Figure 4.1 and 4.2 show that generally, there was thin ice along the troughs.

4.4 Additional ice thickness measurements

Ice thickness measurements made through natural cracks and steam-drilled boreholes in the channel show ice thicknesses ~ 2 m in grid A, with thicker ice in grids B and C (Table 4.3). No additional ice thickness measurements were made in grid D. Ice thicknesses and drafts measured through boreholes in grids B and C are comparable to those measured in the channel with IPR (B: 5-6 m, C: ~ 8 m). Ice drafts of ~ 1 m measured around the

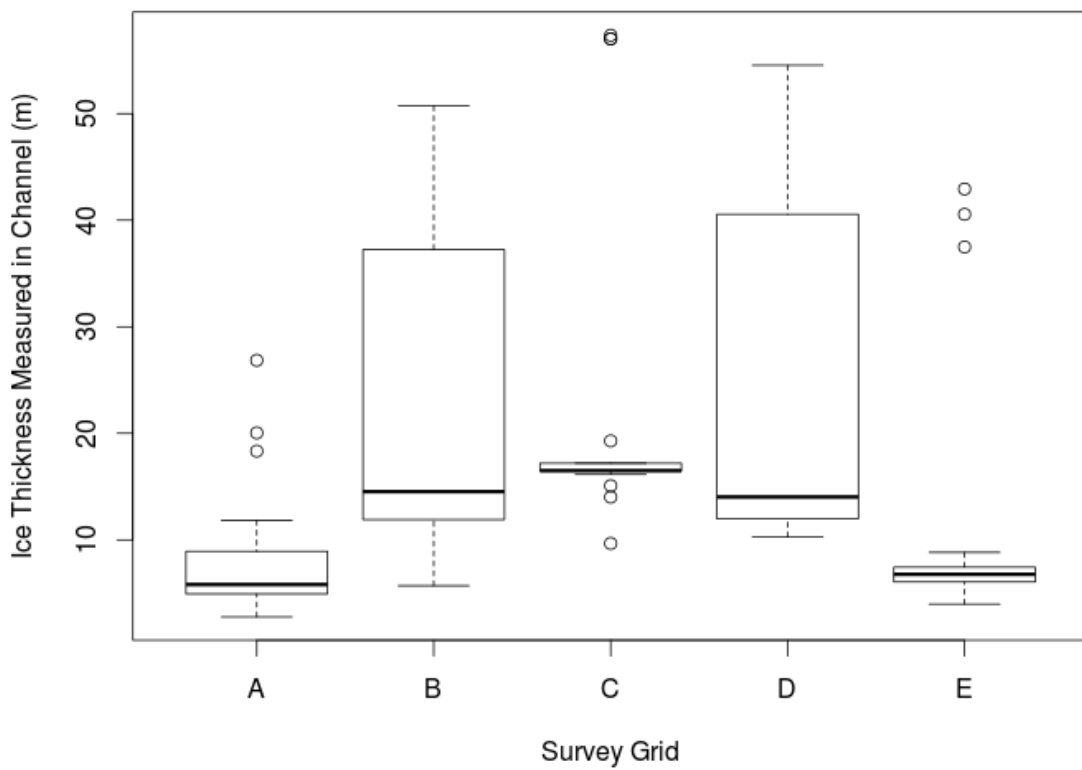


Figure 4.6 Boxplots showing variability in ice thicknesses measured with ice penetrating radar within the channel (grids A, B, C and D) and within the fracture (E).

Table 4.3 Ice thickness and ice draft measurements made through natural cracks and steam-drilled boreholes in the channel.

Grid	Ice thicknesses (m)
A	1.75, 1.52, 1.65, 1.50, 1.68, 1.80, 1.81
B	3.27(draft), 3, 3.5, 7(draft)
C	8(draft)
D	NA*
E	1.04, 1.50 (draft), 1.75 (draft), 1.33 (draft)

*NA indicates no ice thickness measurements were made through cracks or boreholes within the grid

profiling sites in the fracture are thinner than the minimum ice thicknesses that could be measured with the IPR.

4.5 Characterization of snow cover

Snow depths were measured along several IPR transect lines in grid D. Snow depth varied from 0.00 m to 2.60 m, with a median snow depth of 0.25 m (Figure 4.7). Peak snow depth values were measured within the depression but snow depths within the channel were also highly variable. Outside the depression, snow depths were more consistent; depth was generally less than 0.5 m.

4.6 Hydrography

4.6.1 Temperature and salinity profiles

Temperature and salinity profiles from along-channel CTD transects in 2015 and 2016 show the structure of the near-surface water column within the channel, compared to that of the epishelf lake and offshore of the ice shelf (Figure 4.8). The strongly stratified epishelf lake has a layer of warm ($>0^{\circ}\text{C}$) and fresh ($S_A < 1 \text{ g kg}^{-1}$) water overlying colder, more saline water ($<1^{\circ}\text{C}$, $S_A > 25 \text{ g kg}^{-1}$) with a steep halocline and thermocline, indicating the transition occurs over just a few meters. The depth of the epishelf lake was 10.3 m in July 2015 and 9.8 m in July 2016. The profile taken offshore shows seawater through the entire depth of the profile, save for a very thin freshwater cap from seasonal sea ice melt.

Profiles from within the channel are distinct from the epishelf lake and offshore profiles. Channel profiles from both years and both sampling sites show a well-mixed layer several meters thick present just below the ice at both channel sites. This layer had temperatures (-1°C to 0°C) and salinities ($5\text{-}14 \text{ g kg}^{-1}$) that were intermediate

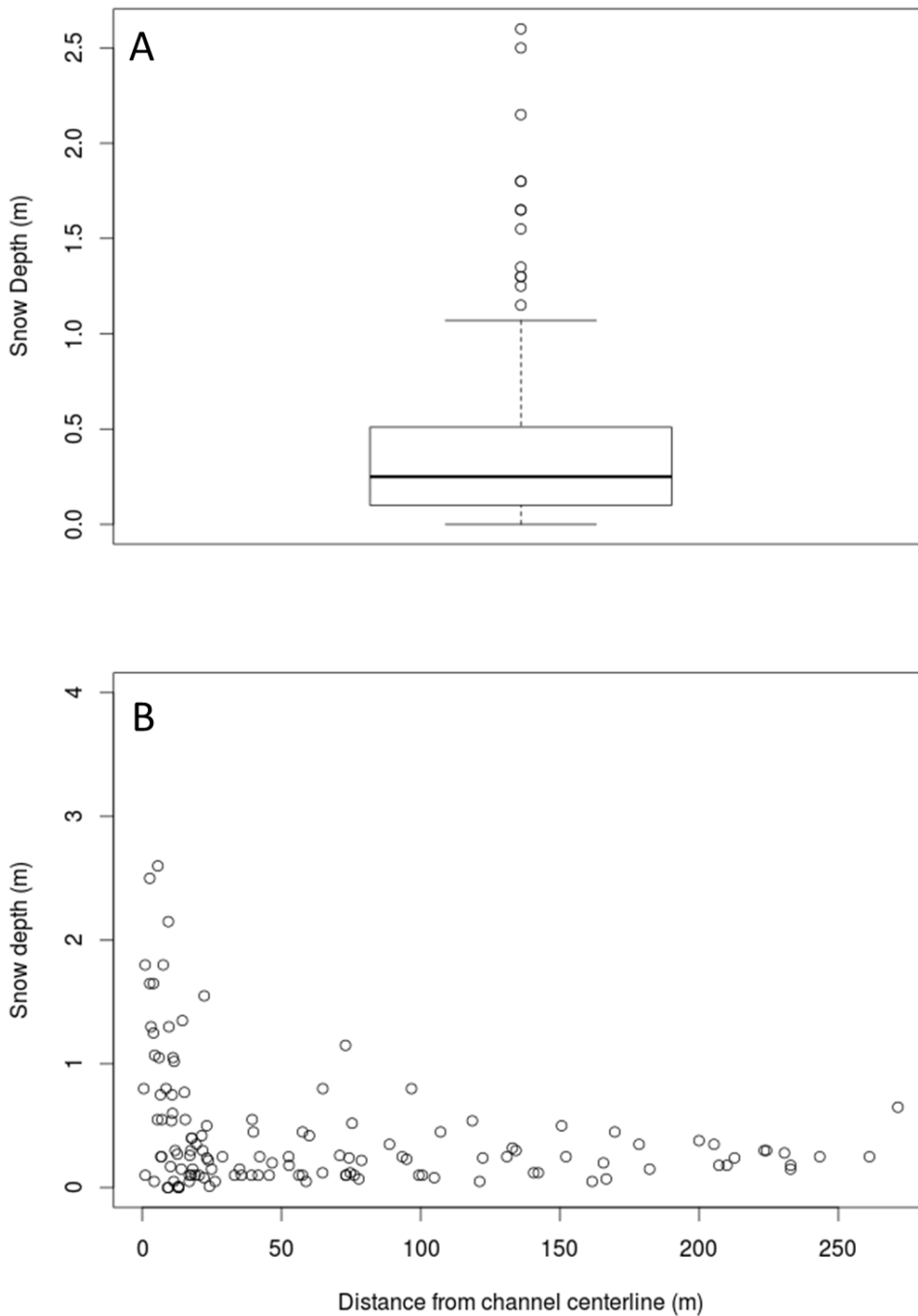


Figure 4.7 Plots illustrating variability in snow depths measured along grid D IPR transects. A boxplot of snow depths (A) shows that median snow depth was 0.25 m, with a minimum of 0.00 and maximum of 2.60 m. A plot of snow depth (B) against distance from the channel centerline shows that snow depths were most variable in the depression overlying the channel; peak values were also located in the channel.

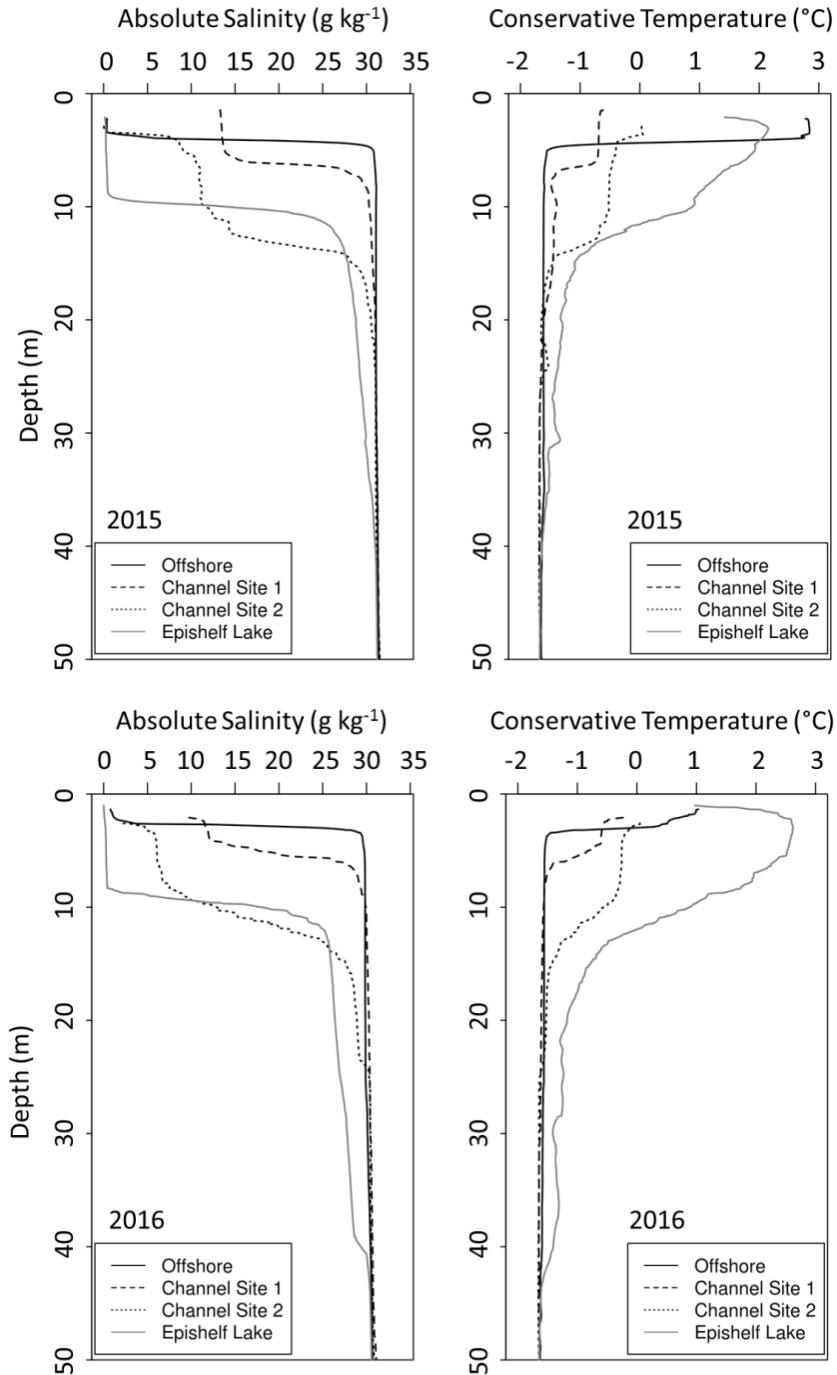


Figure 4.8 Temperature and salinity with depth for four locations in an along-channel CTD transect done in 2015 and 2016. Only the upper water column, to 50 m depth, is shown. Measurements taken within ice were removed from the top of the profiles and the downcasts isolated. The solid black line indicates the profile taken offshore of the ice shelf through a lead in the sea ice; the dashed line is the profile from sampling site 1 at the seaward edge of the channel; the dotted line is the profile from sampling site 2 located roughly mid-channel and the solid grey line is the epishelf lake profile for each year.

between the epishelf lake and offshore profiles. Below the brackish layer, salinity and temperature gradually transition to that of ambient seawater by 30 m depth. At site 1 at the seaward edge of the channel, however, the brackish layer was thinner, saltier and cooler than the layer at site 2 in both years. Although there was some year to year variability, the CTD profiles show that general salinity structure of the profiles, and the spatial pattern seen along the CTD transect, were consistent over the two years of study.

Temperature and salinity profiles from the fracture in 2014, 2015, and 2016 are plotted with epishelf lake and channel profiles in Figure 4.9. The structure of the water column at the fracture site was not consistent year to year. In 2014, the fracture site and epishelf lake profiles showed the same stratified structure with a freshwater layer to 9 m. In 2015, only a thin freshwater layer was present and the water column was very weakly stratified, indicative of mixing. In 2016, the fracture profile again had a distinct near-surface freshwater layer, and had become more stratified than in 2015.

4.6.2 Current measurements

4.6.2.1 Channel

Plots of mean current speed with depth for sites 1 and 2 in the channel show a subsurface jet of relatively fast flowing water from ~3-10 m depth (site 1) and from ~7-15 m depth (site 2) (Figure 4.10). Above and below the jet, current speeds were substantially lower ($<5 \text{ cm s}^{-1}$). The highest current speed at site 1 ($62 \pm 3 \text{ cm s}^{-1}$) was recorded at 5.4 m depth. At site 2, the maximum current speed in the jet of $48 \pm 2 \text{ cm s}^{-1}$ was recorded at 9.9 m depth (Figure 4.10). The sampling increment was ~1.5 to 2 m at site 2, and even coarser at site 1, so even faster water speeds may have occurred at un-sampled depths. Mean current speed with depth at sites 1 and 2 is plotted against salinity in Figure

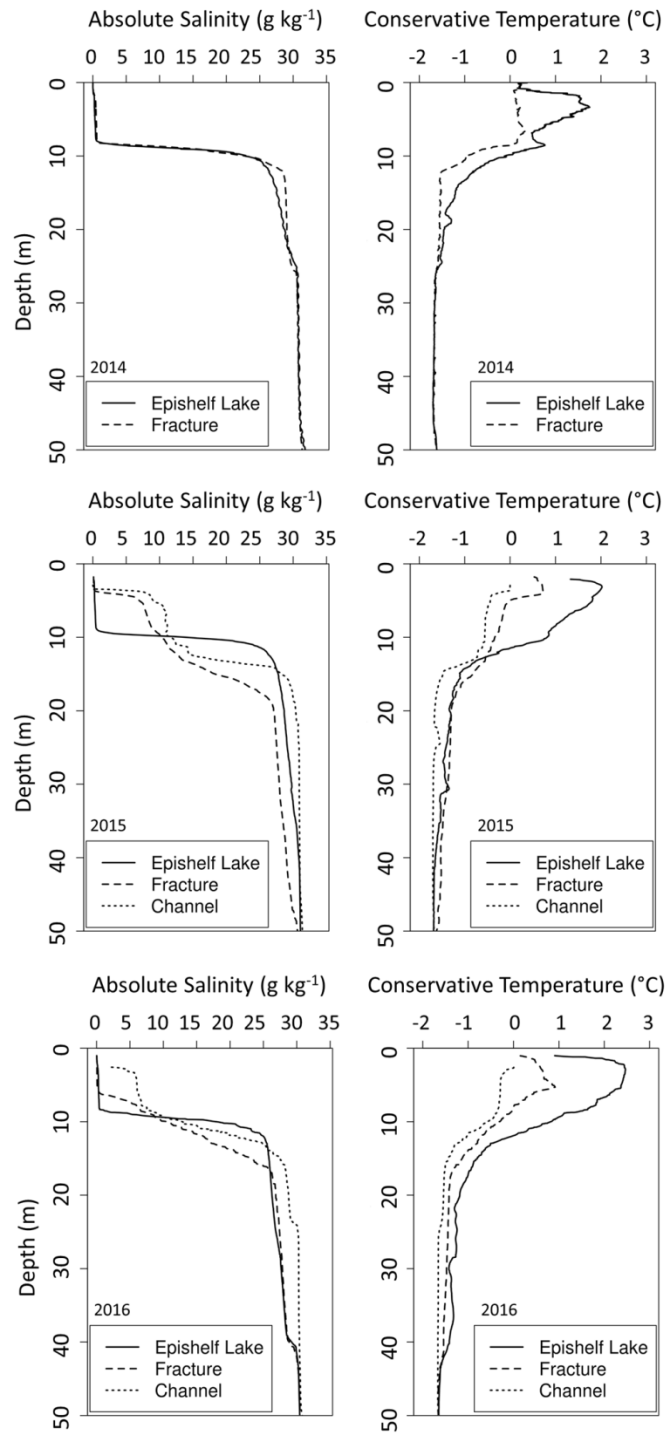


Figure 4.9 Salinity and temperature profiles for 2014, 2015 and 2016 showing profiles from the fracture, plotted against profiles from the epishelf lake and the channel for the same year for comparison. The channel was not profiled in 2014. For each profile, measurements taken in ice were removed, and the downcast isolated. The epishelf lake profile is shown with a solid line, the fracture with a dashed line and the channel profile with a dotted line.

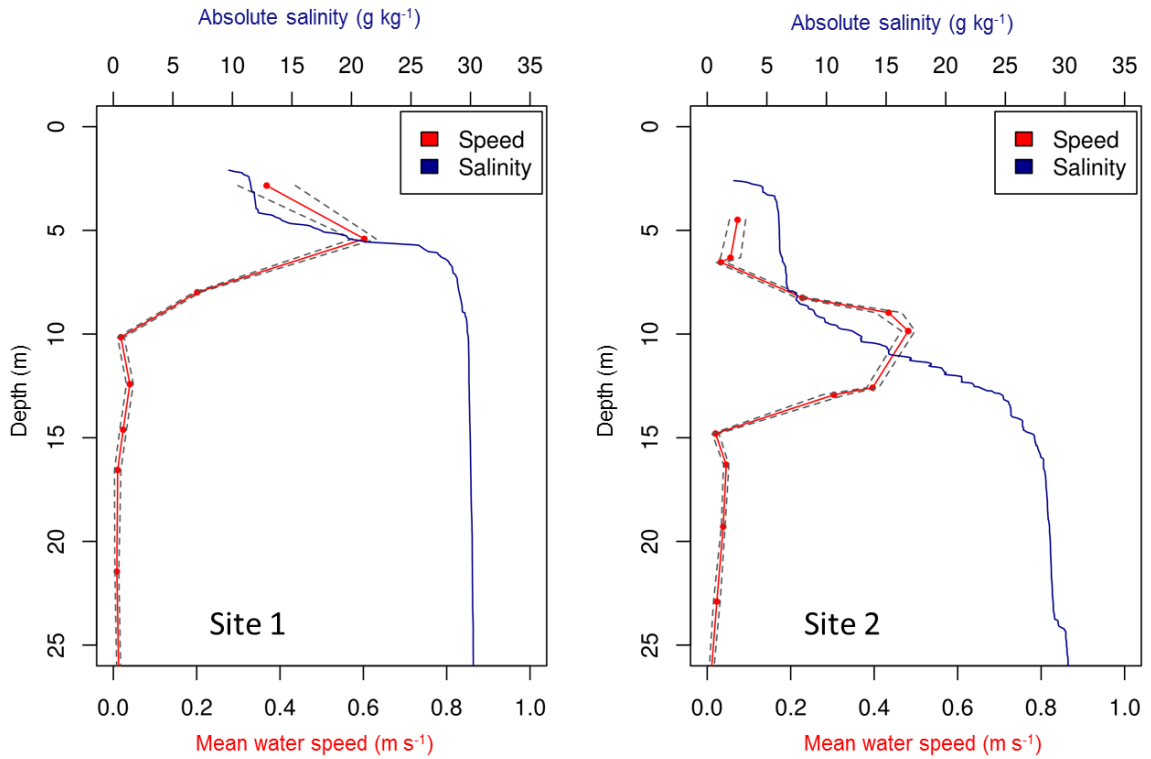


Figure 4.10 Mean water speed with depth at the seaward edge of the channel (site 1), and approximately mid-way along the channel (site 2). Water speed was measured for 2 minutes at each depth, and the mean of the middle 80% of the recorded values taken. Mean speed (in m s^{-1}) is plotted in red; points indicate the depths at which water speed measurements were recorded. The dashed grey lines indicate one standard deviation from the mean. Salinity with depth at each location is plotted in blue.

4.10. The region of fastest flow for both sites occurs within the halocline separating the brackish layer and seawater.

Flow directionality in the channel was inferred from observations. When a weighted line was lowered into the water column in the channel, the instrument line was pulled sharply in the down-channel direction at depths consistent with the depth range of the jet, causing the line to hang at an angle (Figure 4.11). This was observed in all instances where current measurements were being made in the channel, at both sampling sites. Therefore, flow in the channel was assumed to be primarily in the down-channel (out-fiord) direction. No angling of the line was observed at any time when lowering instruments into the water at the fracture.

4.6.2.2 Fracture

Current measurements in the fracture were collected with an ADCP so flow directionality was recorded by the instrument. Flow velocities in the along-fracture (u axis) and along-fiord directions (v axis) were uniformly low to 25 m, at least an order of magnitude slower than flow recorded in the channel (Figure 4.12). Water velocities recorded along the fracture (u axis) ranged from -0.9 to 0.7 cm s^{-1} , with a mean of $-0.2 \pm 2.0 \text{ cm s}^{-1}$; there was no dominant flow direction. Along the v axis, the range was -1.2 to 2.3 cm s^{-1} , with a mean of $0.8 \pm 2.2 \text{ cm s}^{-1}$. Flow occurred primarily in the positive v direction, which was cross-fracture and roughly out of the fiord.

4.6.3 Estimation of discharge

Discharge calculated for each of the 1 m segments spanning the estimated thickness of the outflow jet at sites 1 and 2 are shown in Table 4.4 and Table 4.5, respectively. Based on these results, the total discharge through the channel at site 1 was $110.34 \text{ m}^3 \text{ s}^{-1}$ and

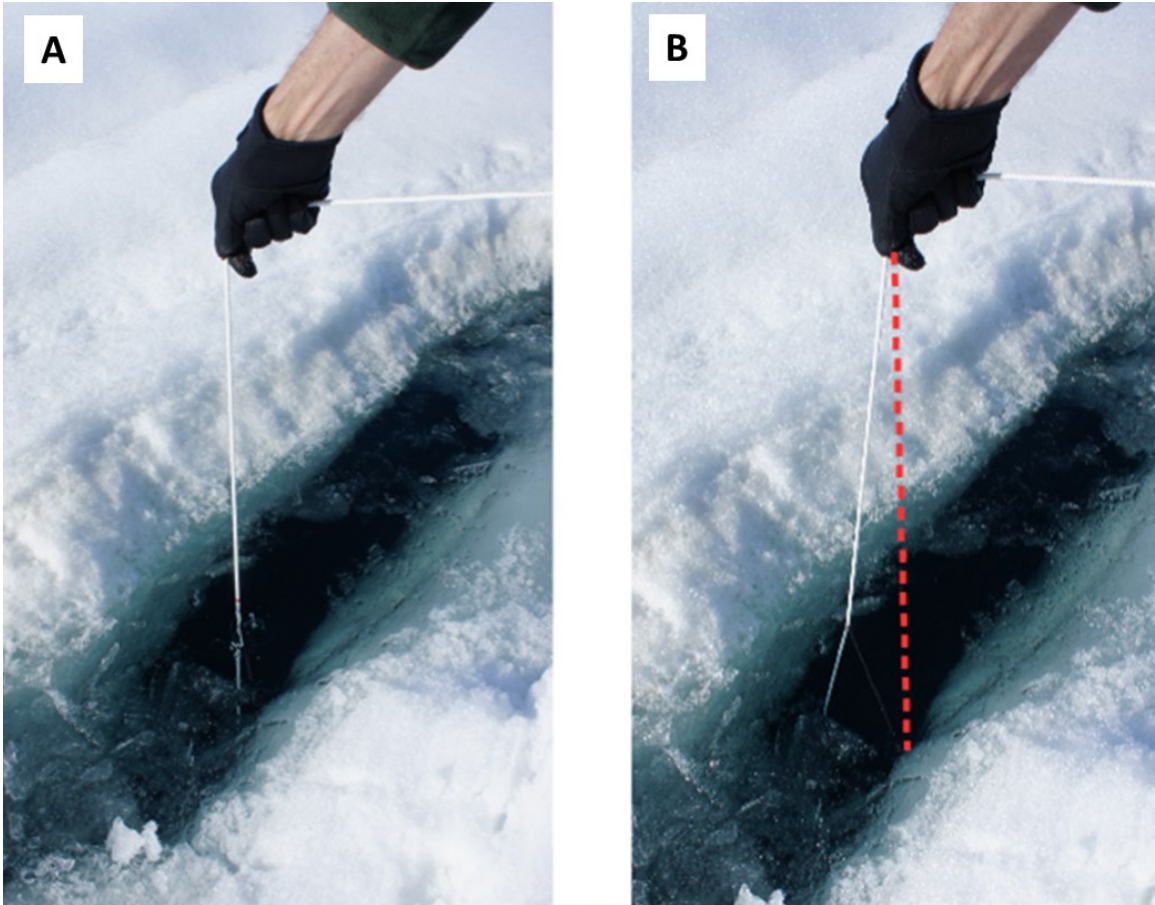


Figure 4.11 Photos of a weighted line lowered through a natural hole in the ice overlying the channel. Panel A shows the line before the weight reached the depth of fast flowing water: the line hung straight down into the water from the hand. Panel B shows the line when it has been taken up by the fast flowing near-surface current. The line was pulled downstream (left side of crack in the photo) and thus, angled away from vertical. The red dashed line marks the vertical from the hand for comparison.

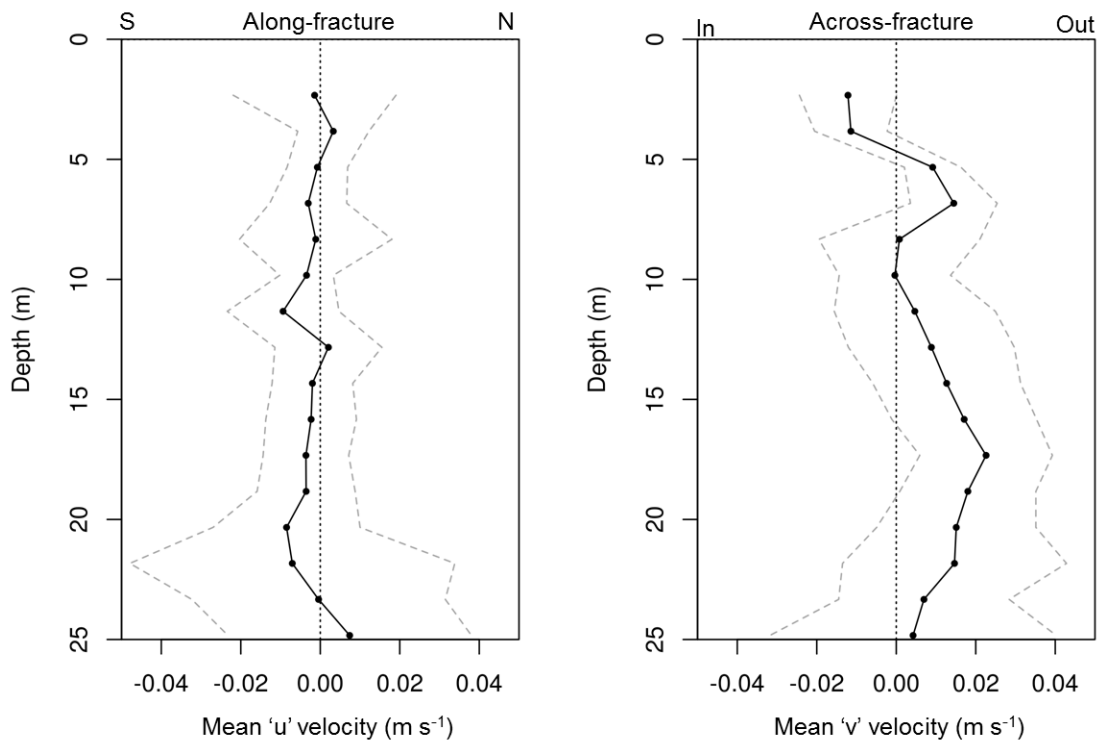


Figure 4.12 Time-averaged velocities with depth in the water column at the fracture. The 'u' axis is along the fracture, with positive u running NE, toward the intersection of the fracture and channel. The 'v' axis is oriented roughly along-fiord, with positive v being toward the ocean. Grey dashed lines indicated one standard deviation from the mean for each depth. Depth bins are 1.5 m, with the center of the first bin at 2.33 m depth.

Table 4.4 Area, water velocity and discharge for each 1 m depth segment over the estimated depth of flow in the channel at site 1. Discharge is summed across all segments for total discharge.

Depth Range (m)	Area (A, m ²)	Velocity (V, m s ⁻¹)	Discharge (Q, m ³ s ⁻¹)
3-4	41.81	0.37*	15.47
4-5	47.38	0.49	23.22
5-6	51.27	0.60*	30.76
6-7	55.16	0.40	22.06
7-8	59.26	0.20*	11.85
8-9	63.46	0.11	6.98
Total			110.34

*indicates a velocity reading was made with the current meter within the specified depth range

Table 4.5 Area, water velocity and discharge for each 1 m depth segment over the estimated depth of flow in the channel at site 2. Discharge is summed across all segments for total discharge.

Depth Range (m)	Area (A, m ²)	Velocity (V, m s ⁻¹)	Discharge (Q, m ³ s ⁻¹)
7-8	17.10	0.13*	2.22
8-9	20.51	0.33*	6.77
9-10	21.42	0.46	9.86
10-11	23.43	0.45*	10.13
11-12	24.28	0.42	9.84
12-13	24.28	0.35*	8.50
13-14	25.33	0.23*	5.82
14-15	26.33	0.10*	2.63
Total			55.77

*indicates a velocity reading was made with the current meter within the specified depth range

55.77 m³ s⁻¹ at site 2. The vertical sampling resolution at site 1 was coarser than at site 2 (Figure 4.10, Tables 4.4 and 4.5) so it is less certain how representative interpolated velocities are of actual flow in the jet. There were also no measurements of velocity made at depths less than 3 metres at site 1, though it is suspected there would have been flow at shallower depths given the relatively high flow velocity recorded between 3 and 4 m (Table 4.4).

5 Discussion

5.1 Morphological evidence for channelization

Cross-sectional ice thickness profiles support the hypothesis that there is a channel incised upward into the base of the Milne Ice Shelf. Cross-channel profiles along the E-W surface depression show a deeply-incised, inverted 'v'-shaped feature with sidewalls that sloped upward on average $\sim 40^\circ$ from horizontal (Figure 4.4, Table 4.2). The morphology of the purported channel is distinct from that of the fracture, which is consistent with differing mechanisms of formation. The inverted 'v' shape of the channel is consistent with upward thermal incision into the ice shelf by water, analogous to the formation of a v-shaped valley by a river. The fracture, in contrast, rifted through the entire thickness of the ice shelf as a result of tensile stresses which exceeded the strength of the ice (Lawn, 1993). As a result, it had consistently near-vertical sidewalls (Table 4.2, Figure 4.5). After formation, the fracture infilled with ice; ice thicknesses are therefore uniformly thin across the fracture width rather than thickening toward the margins as in the channel (Figure 4.6).

Observations of a channel with sloping sidewalls are consistent with the morphology of basal channels detected beneath the floating tongue of the Petermann Glacier in Greenland (Rignot and Steffen, 2008) and the Pine Island Glacier ice shelf in Antarctica (Stanton *et al.*, 2013). The surface morphology of the E-W depression is also consistent with channelization. The presence of a surface depression overlying the channel is consistent with downward deformation of ice toward hydrostatic equilibrium as mass is removed from below (c.f. Vaughan *et al.*, 2012). Longitudinal crevasses were observed along the walls of the surface depression (Figure 1.3). The formation of

crevasses along the flanks of the surface depression overlying a basal channel have also been noted on other ice shelves (Vaughan *et al.*, 2012) and are attributed to bending stresses induced as the ice shelf surface settles downward in response to gradually reduced ice thickness above the channel (McGrath *et al.*, 2012).

5.2 Controls on channel surface and basal morphology

The morphology of the surface depression overlying the channel was somewhat obscured by snow deposition. Limited snow thickness measurements showed snow could be up to several metres thick within the channel (Figure 4.7), so, in many locations, the depression was likely deeper than indicated by the surface elevations presented herein. In addition, snow deposition across the depression may also not have been homogenous across the channel. The orientation of the channel with respect to the prevailing wind, or the effect of local topographic surface variations, may have resulted in preferential accumulation in certain aspects or locations over others.

Although the mean channel basal width was consistent between grids B and D, the mean width of the surface depression in D (96 ± 30 m) was wider and more variable than that of grid B (68 ± 4 m, Table 4.2). If the only factor determining surface depression morphology was the downward deformation of the ice shelf surface to hydrostatic equilibrium, it is expected that surface morphology would be reasonably consistent. At grid C, there was no discernible surface depression overlying the channel at all. Inconsistent infilling of the surface depression by snow may explain the variability in the width of the surface depression between the survey grids. Variability may also be attributed to variations in bridging stresses along the channel. The channel was narrowest at grid C, and the ice thicknesses at the crest of the channel thickest, so it could be that

bridging stresses at that location were great enough that the surface of the ice shelf had not yet slumped noticeably downward. An estimation of whether these surface elevation measurements demonstrate that the ice is in hydrostatic equilibrium should be done. If the ice shelf was not yet in hydrostatic equilibrium, further settling of the ice shelf surface over the channel would be expected in future.

IPR survey grids were spaced along the length of the channel, with the aim of investigating changes in channel morphology over distance. Channel basal morphology (basal width, incision height and sidewall slope angle) was fairly consistent away from the seaward edge of the ice shelf over the 5 km length spanned by grids B, C, and D (Table 4.2). The channel appeared to be broader and less deeply incised at the edge of the ice shelf in grid A, with a shallower mean sidewall slope angle as a result. However, the differences in morphology noted at the edge of the ice shelf (grid A), are likely not reflective of the channel proper.

Rather, the apparent widening is attributed to mistakenly surveying seaward of the actual ice shelf edge. At the location of grid A, the ice shelf was notched inward and had been infilled by MLSI (the Milne 're-entrant' described by Jeffries, 1986). During the IPR survey, many of the across-channel lines crossed from thick ice shelf ice onto the thin sea ice, and back onto thick ice shelf ice on the other side of the notch, rather than over ice shelf-ice thinned by incision. Therefore, no conclusion can be made about whether channel morphology was significantly different at the seaward edge of the ice shelf. It is expected that, had it been possible to survey the length of the channel, the channel would be less incised with distance from the epishelf lake, as the potential for melt (thermal driving) would lessen as heat was lost from epishelf lake outflow.

For four of the IPR transects across grid A, no reflections indicating the ice-water interface could be identified in the thin ice between the thick channel banks. Grid A also had the lowest percentage of traces in which the ice-water reflector could be identified (Table 4.1). The lack of reflections across the channel in grid A is attributed to the attenuation of the radar signal due to the presence of the conductive saline MLSI, coupled with ice thicknesses in the channel that were thinner than the minimum resolvable by the IPR antenna frequency used. Ice thicknesses measured through cracks and steam-drilled boreholes were 1.50 to 1.75 m in the middle of the channel in grid A (Table 4.3). A 50 MHz antenna was used to survey grid A, for which the minimum detectable thickness was calculated to be 1.7 m in Section 3.3.2. Where ice is too thin, the air and reflected waves overlap so it was not possible to identify and pick the location of the ice shelf base in many locations.

Previous studies of basal channel morphology have identified both smooth-sided basal channels (Rignot and Steffen, 2008; Stanton *et al.*, 2013) and channels with terraced sidewalls (Dutrieux *et al.* 2014). Dutrieux *et al.* (2014) described terraced channel geometry in two different settings, on both an Antarctic ice shelf (Pine Island Glacier) and the Petermann Glacier (Greenland), leading them to conclude terraced melting could be a generic feature of melting in an ice shelf channel. Topographic variability along a channel results from heterogeneous melt patterns; they suggest that it is specifically uneven melt due to stratification in the ice-ocean boundary layer within a channel that leads to terracing. Variability in slope angles calculated along the channel walls in this study show there is local (metre-scale) topographic variability along the

channel walls (Table 4.2), and cross sectional profiles are suggestive of the existence of stepped topography near the base of the channel for grids B and D (Figure 4.4).

Although terracing noted by Dutrieux *et al.* (2014) is on scale much larger than what was observed here (terraces hundreds of metres wide in Antarctica and Greenland), it is plausible that the steps seen here are also caused by stratified flow and heterogeneous melt rates. Indeed, the CTD profiles from within the channel collected in this study, discussed in section 5.3, suggest flow is stratified within the channel beneath Milne Ice Shelf (Figure 4.8). The steps identifiable in the cross-sectional profiles occur 30 to 50 m below the top of the channel. At this depth, the CTD profiles from the channel indicate there is no influence from the epishelf lake as water properties are consistent with ambient ocean water (Figure 4.8). The formation of steps would presumably occur near the top of the channel where the warm epishelf lake outflow is in contact with the channel sides. These steps are unlikely to be the result of active incision, but they may be ‘legacy’ channel features, formed earlier when the channel was less deeply incised.

If steps are formed sequentially as the channel is incised, steps may be expected along the height of the channel walls, which is not seen in these data. However, the full extent of topographic variations along the channel walls is not well resolved by the methods used here, since a detailed geometry of the channel walls is hampered by the presence of noise from multiple reflectors off the steeply angled walls (e.g. Figure 4.3). The channel, therefore, may appear artificially smooth away from the channel base, due to the linear interpolation used to fill in missing thicknesses. Some of the apparent variability in sidewall slope angle is undoubtedly the result of errors in the determination of the correct position of the basal reflector, but erroneous picks are unlikely to account

for all the observed variability. Conversely, the presence of terraced topography also controls melt rates (Dutrieux *et al.*, 2014), so an understanding of detailed channel morphology may be an important element in understanding melt and channel evolution.

Minimum ice thicknesses at the crest of the channel measured in the IPR survey were 6 ± 2.58 m in grid B, and 10 ± 2.58 m in both grids C and D. Ice thicknesses are consistent with those made through cracks and boreholes in grids B and C (Table 4.3) and with findings by Mortimer (2011) of ice <10 m thick in the channel based on a limited number of cross-sections in 2008-2009. Mortimer *et al.* (2012) also identified a large area of thin ice (~ 20 -30 m) abutting the southern side of the channel near the confluence of the channel and the N-S fracture formed prior to 1950 (Figure 1.4). They measured much greater ice thicknesses on the opposing side of the channel (upwards of 50 m). The presence of this anomalous area of thin ice, combined with depth soundings that showed the sea bed rose to within 28 m of the surface led Hamilton (2016) to conclude the ice shelf was likely grounded on a seabed ridge that rises beneath the ice shelf and extends 2 km south of the fracture. Findings of differential reflectivity from the ice shelf base in this area by Narod *et al.* (1988) are also consistent with a grounded ice shelf.

The area of thin ice detected by Mortimer *et al.* (2012) and the location of the depth sounding by Hamilton (2016) are coincident with the location of the asymmetrical ice thickness profiles from grid C, where thicknesses were significantly less on the left (south) side of the channel (40 ± 2 m) than on the right (north) side (59 ± 2 m). This effect is also seen in profiles from grids B and D, though it is less pronounced (Table 4.2, Figure 4.4). The results presented here provide corroborating evidence for a locally grounded ice shelf. Further, the ice thickness profiles may help to constrain the extent of

the seabed ridge, as they show that the ice shelf might be grounded for as much as 4 – 5 km (the distance between grids B, C, and D) along the south bank of the channel. Future work should examine the nature of basal reflectivity on either side of the channel, as an additional line of evidence for a grounded ice shelf.

Differing slope angles on the left and right sides of the channel in profiles from grid C might be the result of variability in melt rates due to an asymmetrical flow velocity profile in the channel at grid C. Deflection of flow to the right wall of the channel and the associated elevated velocities could have accelerated melting along the right wall, for instance, similar to the development of a steep cut bank on the outside of a river meander. Modelling investigations of channel formation have shown that the deflection of flow through a channel by the Coriolis force could result in preferentially higher melt rates to one side and, thus, asymmetry in channel side slope angle (Millgate *et al.*, 2013).

However, the scale of the channel on the Milne Ice Shelf is much smaller than the range of the Rossby radius of deformation for the Arctic (e.g. Cottier *et al.*, 2010) so deflection by the Coriolis force does not explain why the right side of the channel is steeper at grid C. Local deflection of flow due to curvature in the channel is a possible explanation; RADARSAT-2 imagery and photos of the surface depression (Figure 1.3) do show some meandering along the channel. Perhaps differential hydrostatic adjustment of grounded and ungrounded ice due to mass removal (or gain, if accretion occurred at the ice shelf base for some reason) also had an impact on side slope asymmetry. It is possible that side slope asymmetry is somehow related to the left-right asymmetry in ice thicknesses at grid C since, for instance, if the ice shelf is grounded in this location, perhaps a local deflection of flow occurs as a result of the influence of sea bed

topography there. The difference in side slope angle could also be related to differential movement of the ice shelf on the right and left sides of the ice channel as a result of grounding. If ice on the right side of the channel is moving relative to the other one side of the channel (because only the floating side is adjusting to hydrostatic equilibrium as the ice shelf thins), then perhaps the ongoing deformation of the ice along the channel can explain the observed morphology.

The data suggest that channelized melt produced the observed surface and basal morphology, but ice shelf grounding is a plausible mechanism to explain the initiation of this channelized flow beneath the Milne Ice Shelf. If the ice shelf was indeed locally grounded, tensile stresses (from differential movement of the grounded and ungrounded ice in response to tides, for example) may have resulted in weaknesses/fractures within the ice, or basal crevassing, along the grounded/ungrounded boundary. Over many years, outflow from the epishelf lake could then have been preferentially directed along this weakness, resulting in upward incision and the observed channel morphology. This potential model for channel formation is consistent with Keys' (1978) assertion that channelization would be unlikely to be initiated by epishelf lake outflow alone, as any incipient channel would fill with frazil ice as the thin outflow layer cooled. A large volume of outflow directed through an existing weakness, in contrast, would have a high heat content and thus, high melt potential.

5.3 Properties of flow through the channel

Current measurements, coupled with CTD profiles of the channel water column, confirm that the channel was a drainage pathway for the epishelf lake. A fast-flowing jet of water flowing in the down-channel direction was detected at both sampling locations in the

channel. Peak flow velocities recorded at both sites in the channel (40-60 cm s^{-1} , Figure 4.10) are an order of magnitude higher than velocities measured below the halocline of the epishelf lake (i.e. where outflow could theoretically occur) (1-2 cm s^{-1} , Hamilton, 2016) or velocities measured along either axis at the fracture (Figure 4.12, 1-2 cm s^{-1}). Tidal dynamics cannot explain flow velocities of the observed magnitude, as the tidal range in the fiord is very small (Hamilton, 2016). The presence of the jet therefore suggests that outflow is being concentrated in the channel. The observation of the fast flowing jet at both sampling sites in the channel, coupled with the consistent surface and basal morphology along the channel, also confirms the channel is continuous and connected.

The thickest ice along the outflow channel acts as a constriction and so, controls flow through the channel and the depth of the epishelf lake. It seems likely the constriction is located in the area of grid C. Minimum ice drafts measured at the crest of the channel in grid C with IPR and through a steam drilled borehole were 8-9 m whereas drafts on either side along the channel in grids B and D were much less (Tables 4.2, 4.3). Though there is uncertainty associated with ice thickness measurements, a draft of ~ 9 m is roughly consistent with the measured depth of the epishelf lake in July 2015 (10.3 m) and July 2016 (9.8 m) since it is expected that the freshwater layer would be distinctly deeper than the minimum draft by July, at the height of the melt season, due to inflow. The exact properties of the warm outflowing epishelf lake water depend on the depth of the outflow layer. At 9 m depth in 2015 and 2016, water in the epishelf lake had a temperature of $\sim 1^\circ\text{C}$ and an absolute salinity of $< 1 \text{ g kg}^{-1}$, whereas by 10 m depth, water had an absolute salinity of $\sim 15 \text{ g kg}^{-1}$ but was still $\sim 1^\circ\text{C}$ in temperature (Figure 4.8).

It can be seen from the velocity profiles from site 2 that outflow did not occur right at the top of the channel but rather, peak velocities occurred within the halocline at 9.9 m depth (Figure 4.10). The water flowing out of the epishelf lake in the jet is fresher and more buoyant than the seawater beneath the ice shelf, but denser than the fresh water being generated at the top of the channel through submarine melting of the ice shelf (and from the injection of surface meltwater in some cases). As a result, the outflow jet is vertically constrained by density stratification, and it cannot rise up against the base of the ice shelf. Sampling resolution is poor at site 1 but flow appears to be shallower and closer to the ice shelf base; velocity at 5.4 m depth was $62 \pm 3 \text{ cm s}^{-1}$. This may be because stratification of the water column lessens downstream (e.g. because less melt is generated as the heat content of the jet diminishes), allowing the jet to rise higher up in the channel.

The outflow jet transported the warm and comparatively fresh epishelf lake water through the channel, which modified the structure of the water column. If there was no epishelf lake outflow in the channel, a water column structure resembling a typical offshore profile would be expected, with a very thin layer of surface meltwater transitioning quickly to seawater. Instead, at the depth of the jet, water in the channel is warmer and fresher than seawater, consistent with outflow. However, with distance from the epishelf lake, the halocline shoals upward, and water in the jet is cooler and saltier, indicating the water column was becoming more and more well-mixed with distance along the channel. Therefore, it is concluded that the velocity of the jet must be sufficient to overcome stratification in the channel and cause turbulent mixing, at least in some places along the channel.

Both sites 1 and 2 had a connection between the ice shelf surface and the channel, as sampling was done through natural cracks in the ice, and surface meltwater was observed to flow into these cracks. The addition of surface meltwater may have altered the structure of the water column somewhat at the sites sampled (e.g. the thickness of the meltwater layer at the top of the channel impacts at what depth the outflow jet can flow). Nonetheless, the hydrographic profiles here clearly demonstrate epishelf lake water was flowing through the channel and the similarity in flow velocities measured at channel sites separated in space suggests velocity measurements were fairly representative.

The morphology of the channel and the presence of epishelf lake water in the channel are consistent with the idea that warm epishelf lake outflow transports heat into the channel causing localized melting and channelization. As previously described, the outflow jet was vertically constrained due to stratification in the channel, so it flowed a few metres below the top of the channel. The presence of a mixed layer at the top of the channel overlying the warmer epishelf lake water may mean that there is insufficient heat at the top of the channel for significant melt, so melting may be concentrated along the sides of the channel where velocities are highest. There may even be freezing occurring at the top of the channel while melting occurs along the sides, as has been theorized to occur in some basal crevasses (Khazendar and Jenkins, 2003). With distance from the epishelf lake, water in the jet was cooler and more saline, as heat was presumably lost to melting and as more cold seawater was mixed upward (Figure 4.8). Therefore, melt rates in the channel are expected to decrease with distance from the epishelf lake. Indeed, channel incision heights calculated here decreased slightly in the down-channel direction (from grids D to B) which is consistent with decreasing melt rates.

Freshwater input to the epishelf lake occurs from early-June to mid-August during the melt season, resulting in a corresponding deepening of the epishelf lake (Hamilton, 2016). When inflow ceases, the epishelf lake gradually thins as excess freshwater flows out of the channel. Outflow beneath the ice shelf is non-linear and drainage occurs at a rate proportional to the difference between the minimum ice draft and the epishelf lake depth (Hamilton, 2016). Therefore, discharge through the channel increases over the melt season, reaching a maximum at the end of the melt season in mid-August when the epishelf lake is deepest. Heat content of the epishelf lake also increases over the melt season (Hamilton, 2016). Consequently, outflow velocities and the structure of the water column (temperature, salinity and thickness of the mixed layer), as well as the resulting melt patterns, are presumed to vary over the course of the year. Melting may be ongoing, or may have seasonal modulation. Future work should focus on obtaining hydrographic measurements over time, to understand how the velocity, thickness, flow depth and temperature of the outflow jet changes over the year, as these dynamics will impact melt and channel evolution.

5.4 Discharge

Discharge through the channel was estimated at $110 \text{ m}^3 \text{ s}^{-1}$ at site 1 in the channel, and $56 \text{ m}^3 \text{ s}^{-1}$ at site 2 (Tables 4.4 and 4.5). The estimate from site 2 is likely more reliable than that from site 1, due to a higher density of velocity measurements through the depth of flow there. In addition, the location of site 1 in grid A may also mean that this discharge measurement is not representative of flow through the channel because this location may not be within the channel proper, as previously discussed. Nonetheless, while there is uncertainty in these estimates, discharge calculated for site 2 in particular is likely a

reasonable first order approximation of the magnitude of epishelf lake outflow volume directed through the channel for the date sampled.

To explore how important the channel might be in draining the epishelf lake, an estimate of total outflow from the epishelf lake is required for comparison. The available estimates for outflow are bulk annual estimates. Using the glacier mass budget for the northern Canadian Arctic Archipelago for 2000 – 2011 estimated by Lenaerts *et al.* (2013), the total meltwater runoff from the 1108 km² Milne Fiord catchment is estimated to be at least $1.12 \times 10^9 \text{ m}^3 \text{ a}^{-1}$ by Hamilton *et al.* (2017). The percentage of this runoff that enters the fiord at the surface and contributes to the epishelf lake is likely between 10 and 28%, based on observed changes in the depth of the epishelf lake (Hamilton *et al.*, 2017). Assuming that 30% of the total meltwater runoff enters the epishelf lake as inflow, and that over the course of the year all inflow leaves the epishelf lake as outflow, this gives a total outflow estimate of $3.4 \times 10^8 \text{ m}^3 \text{ a}^{-1}$.

Discharge in this study was measured on a day in mid-July, which is approximately midway through the melt season (mid-June to mid-August). The lake deepens over the melt season, reaching a maximum depth in mid-August, and outflow from the epishelf lake increases with the depth of the freshwater layer (Hamilton *et al.*, 2017). Therefore, the outflow volume through the channel in mid-July is unlikely to represent the maximum discharge volume reached over the melt season. Outflow from the epishelf lake occurs during the entire year, but it would be much lower in early June when the epishelf lake is at its lowest. If, as a rough estimate, the discharge value from site 2 is taken to be something close to mean discharge volume over the two month melt season, then the total outflow volume through the channel over 2 months is $\sim 2.9 \times 10^8 \text{ m}^3$. On this

approximation, outflow through the channel during the summer alone would account for 85% of the total annual outflow of $3.4 \times 10^8 \text{ m}^3$ as calculated above. If the discharge from site 1 were used, the estimate of outflow through the channel would be even higher. While these estimates for discharge through the channel and total outflow from the epishelf lake are highly simplified, and it is beyond the scope of this thesis to do a detailed accounting of inflow and outflow, discharge data are a first look at the relative importance of the channel in draining the epishelf lake. These calculations suggest that outflow through the channel is at least the same order of magnitude as total outflow from the epishelf lake and, further, that it is possible the channel is indeed an important drainage pathway for the epishelf lake.

This interpretation is supported by the findings of Hamilton *et al.* (2017), who showed that observed changes in the depth of the Milne Fiord epishelf lake were well modelled assuming that outflow was directed through a constriction of similar dimensions to the one mapped herein. Additionally, findings by previous investigators suggested that the only ice thin enough to constitute an outflow channel beneath the ice shelf is along the E-W feature (Narod *et al.*, 1988; Hamilton *et al.*, 2017, Figure 1.4). There are no other candidate surface depressions or fractures on the ice shelf that could represent outflow conduits (Figure 1.3A). Therefore, it seems plausible that the channel documented here accounts for the majority of the water leaving the Milne Fiord epishelf lake.

5.5 Fracture hydrography and morphology

The fracture had similar water properties to the epishelf lake, which suggests there was connectivity between the fracture and the main body of the epishelf lake. Epishelf lake

water in fractures within the ice shelf have been previously noted, indicating a network of fractures must connect the main body of the epishelf lake to these ‘satellite’ lakes (Hamilton, 2016). There was, however, variability in the depth of the freshwater layer in the fracture between the years surveyed. In 2014, the depth of the freshwater layer was identical to that of the main epishelf lake (Figure 4.9). ADCP measurements showed negligible flow along and across the channel in 2014, consistent with the presence of strong stratification of the water column that year (Figure 4.12).

In 2015, however, the water column structure in the fracture did not resemble that of the main epishelf lake. The gradient of the halocline and thermocline were much gentler and the stratified structure was disturbed (Figure 4.9). The freshwater layer thinned to just a few meters. In 2016, though, it appeared the epishelf lake may have been once again developing within the fracture, as the freshwater layer had deepened and the halocline steepened. However, while there was evidence from the CTD profiles that mixing had occurred, no appreciable flow was noted in the fracture in either 2015 or 2016 when a weighted instrument line was lowered into the water column, as noted earlier.

The seeming recovery of the stratified structure of the water column in 2016, coupled with the fact that there was no flow through the fracture, indicates that the disruptions of the stratified water column structure in the fracture were the result of temporary events and not, say, the result of outflow through the fracture. Mixing at the fracture may have been caused by an isolated (and time-limited) mixing event that caused localized changes to the water column structure in the fracture. This phenomenon is not unknown in Milne Fiord; a sudden decrease in the thickness of the main epishelf lake in January 2012 was attributed to an episodic mixing event by Hamilton (2016). Internal

waves, tidal oscillations and iceberg calving events outside the fiord have all been suggested as possible mechanisms which could generate energy for episodic mixing (Veillette *et al.*, 2008; Hamilton *et al.*, 2017). Alternatively, the connection between the fracture could be ephemeral and the 2015/2016 profiles were taken while the fracture was draining and/or refilling of the fracture with epishelf lake.

The presence of the epishelf lake water in the 2009 fracture helps to further constrain the specific location of the ice shelf dam, i.e. the constriction that controls the depth of the epishelf lake and marks the beginning of channelized outflow. The fracture intersects the channel very close to the fiordward end of the channel. The dam must be seaward of the fracture or the epishelf lake would not have been present there, as it would have drained out through the channel. Combined with the ice draft measurements along the channel, this further suggests the constriction is in the area of grid C.

Ice thickness measurements showed that along most of the troughs between rolls in the vicinity of the fracture, ice was very thin (<10 m), but along one, ice thicknesses in the troughs were comparable to those beneath roll crests (Figures 4.1 & 4.2, Figure 4.4). Though these findings represent a fairly small sample area, they shed some light on the ongoing question of whether (or to what degree) the rolling surface topography on the surface of the ice shelf is echoed at the base (Jeffries, 2017). These results seem to suggest the base is not a mirror image of the surface, but that significant topographic variability at the ice shelf base is related to surface topography. Narod *et al.* (1988), in contrast, found that there was little to no bottom expression of the surface rolls on the Milne Ice Shelf. However, the IPR survey lines along the rolls and troughs only extend to

~200 m on either side of the fracture, so it cannot be said how widespread this pattern is from these data.

If the thinning is localized, it may be the result of lateral melting along the fracture walls by the warm epishelf lake water in the fracture. The concentration of melt along certain troughs is still perhaps suggestive of some dampened initial variability in ice thickness on the underside of the ice shelf resulting in preferential melt along the thinner ice, however. White *et al.* (2015) also noted thin ice in troughs on the Petersen Ice Shelf, and ice islands from the Petersen Ice Shelf appeared to be ridges that had broken away from the ice shelf along troughs. The findings of White *et al.* (2015) imply that the results presented here, of thin ice in troughs, could be very significant in terms of ice shelf stability as they represent zones of weakness that could make the Milne Ice Shelf more prone to fracture.

5.6 Sources of error

Minimum absolute surface elevations measured in this study were below 0 m asl (Figure 4.1), but the ice surface was not observed to be depressed below sea level at any location. Negative surface elevations are attributed to the vertical datum used as a reference for surface elevations. The datum used in this study to post-process locational data was the CGVD28 datum. The accuracy of heights derived with CGVD28 in southern Canada is ± 5 cm, whereas in northern regions the accuracy is on the order of decimeters because there are few accurate and known CGVD28 height benchmarks that can be used for correction in northern Canada (Hughes Clark *et al.*, 2005). Uncertainty in absolute surface elevation does not present a problem in interpreting the results in this study,

because relative elevations and ice thicknesses are not affected assuming the error in vertical position is constant over the small area surveyed.

There was also uncertainty in ice thickness measurements due to picking errors which was quantified using a cross-point analysis (Table 3.2). While the median difference in cross-points was 1.4 m, there were some instances with very large disagreement between cross-points. Error in ice thicknesses reported here is attributed primarily to differences in the apparent depth of the bed reflection between down-channel and across-channel IPR transects where basal topography was steeply sloped. A pulse of energy transmitted by a radar system is not focused, but spreads out as it travels through the ice (Hubbard and Glasser, 2005). Therefore, where the ice is sloped, reflected energy is returned from points upslope of the point directly below the midpoint of the transmitter and receiver (the nadir), as well as from the nadir (the location of the desired reflector). Steep basal topography, such as the side slopes of the channel in this study, result in multiple off-nadir reflections (Bauder *et al.*, 2003), which makes it difficult to determine the true location of basal reflections in survey lines that travel longitudinally along or adjacent to a steep slope.

Along-channel IPR transects were highly susceptible to multiple reflections from the channel sidewalls because profiles were along the slope, while cross-channel transects were less affected. Large errors in ice thickness were most likely the result of a correct pick of the bed reflection in the cross-channel line and an erroneous pick in the along-channel line. However, while the cross-point analysis used points from the intersection of along- and across-channel transects, only cross-channel profiles were used to generate

plots of ice thickness with distance across the channel/fracture and calculate geometry. Therefore, large errors in picks are unlikely to plague cross-channel profiles.

The presence of meltwater ponds and wet slush in the depression also prevented picks from being made in many cases, as the radar signal was attenuated by water and there was no bed reflection. In some cases, ice thicknesses were recorded that are thinner than the minimum resolvable thickness for the antennae used (the minimum ice thickness reported in Chapter 4 was 1 m). Nonetheless, although there were errors in the selection of the correct reflector particularly where ice was thin, ice thicknesses measured along the channel banks and within the channel are in good agreement with previous studies (Mortimer, 2011; Mortimer *et al.*, 2012). Additionally, ice thicknesses measured through steam-drilled boreholes and natural cracks within the channel compare very well with coincident IPR results (Tables 4.2 & 4.3), providing confidence in this analysis.

5.7 Implications of channelization for ice shelf stability

Thin ice overlying the basal melt channel represents a significant structural weakness in the Milne Ice Shelf. Reduced mechanical strength along the channel means the ice shelf is likely to be particularly vulnerable to fracturing along this weakness. Crevassing along the channel at the surface of the ice shelf is also an indicator of reduced ice shelf stability due to channelization (Vaughan *et al.*, 2012). Ice thicknesses at the crest of the channel are already as little as 6 m in some locations. As described previously, the 2001-2002 breakup of the Ward Hunt Ice Shelf is thought to have occurred along a basal channel incised by epishelf lake outflow, where ice thickness were ~25 m, compared to mean thicknesses of 40-60 m (Mueller *et al.*, 2003). The drainage of the epishelf lake dammed by the Petersen Ice Shelf may have initiated in a similar way. A ‘meandering fissure’ was

noted running from the epishelf lake along the margin of the ice shelf and the location of this fissure coincided with the thinnest ice surveyed on the ice shelf (White *et al.*, 2015).

Increased incision of the Milne Ice Shelf is expected in a warming climate. Meltwater runoff is predicted to more than double over this century (Lenaerts *et al.*, 2013). Increased inflow into the epishelf lake will cause increased outflow through the channel. Increased outflow volume will result in augmented heat transport to the channel, leading to higher melt and incision rates in the channel. Repeat ice thickness measurements at one location in the channel showed that overlying ice thickness had already decreased from ~40 m in 1981 to <10 m in 2008/2009 (Mortimer, 2011). Based on the change in the depth of the epishelf lake, Hamilton (2016) estimated that the minimum draft of the ice shelf (the ice dam) thinned a further 5.4 m between 2009 and 2014. If the ice shelf does not fracture along the channel first, enhanced melt along the channel as a result increased outflow could incise completely through the ice overlying the channel in the next 5 to 10 years.

6 Conclusion

The aim of this study was to determine whether epishelf lake outflow was channelized beneath the Milne Ice Shelf. The results of this study support the hypothesis that a curvilinear depression that ran E-W across the outer region of the ice shelf was the surface expression of a basal channel and confirm that outflow occurred along this channel.

The first objective of this study was to characterize the morphology of the suspected channel and compare it to a straight stress fracture that formed on the ice shelf in 2009. Ice penetrating radar was used to map ice thicknesses in several survey grids along the length of the ~11 km channel. Cross-sectional ice thickness profiles revealed an inverted 'v'-shaped basal channel with sloping sidewalls beneath the surface depression, consistent with incision of the ice shelf by warm water. The mean slope of the channel sidewalls ranged from ~40 to 60°. Ice thickness data from grid A were determined not to be representative of the channel but rather the result of surveying seaward of the ice shelf edge. Away from the edge, in grids B, C and D, the channel was 57- 86 m wide at the base and was incised 39-40 m upward into the ice shelf, which was >70% of the mean ice shelf thickness. Ice thicknesses at the crest of the channel were as little as 6 ± 2.58 m. The fracture, in contrast, had rifted through the entire ~40 m thickness of the ice shelf. It had steeply sloping parallel sidewalls and was infilled with uniformly thin ice (<5 m).

The surface morphology of the channel was also consistent with channelization. The presence of a depression is consistent with channelization, formed as unsupported ice deforms downward to hydrostatic equilibrium. Stresses induced as the ice surface settles results in the formation of crevasses along the flanks of the channel at the surface;

longitudinal crevassing was observed at several locations along the length of the channel. Variability in the width of the depression along the length of the fracture might result from infilling by snow, and/or along-channel differences in bridging stresses that determines the ice shelf response to the removal of mass from below.

Channel morphology at grid C was notably different than it was within 1-2 km on either side in grids B or D. The cross-sections from grid C showed that ice thicknesses were significantly less on the left side of the channel than on the right side. The right side of the channel was also much more steeply sloped than the left side (80° compared to 42°). Asymmetry in ice thickness was seen in profiles from B and D, but was much less pronounced; mean sidewall slope angles were consistent for both sides of the channel in grids B and D. Previous investigators have suggested the Milne Ice Shelf was locally grounded on a sea bed ridge in the vicinity of the channel. Asymmetrical cross-channel profiles presented here seem to be consistent with grounding along the inner edge of the channel, but further work needs to be done to confirm grounding.

The second objective of this study was to profile the temperature and salinity of the water in the channel, as well as current speed and direction, to determine whether they were consistent with epishelf lake outflow. Conductivity-temperature-depth (CTD) profiling of the water column in the channel, coupled with the current measurements, confirmed warm, brackish outflow from the epishelf lake flowed through the channel. Flow velocities $>60 \text{ cm s}^{-1}$ were recorded in the channel, which was an order of magnitude higher than flow recorded in the epishelf lake or in the fracture, indicating that outflow was concentrated in the channel. Peak velocities of the outflow jet occurred within the halocline, several metres below the top of the channel due to the stratification

of the channel water column. Stratified flow may also mean melt in the channel is concentrated along the channel sides, rather than the top. The stratified nature of flow in the channel may also have influenced the development of local variations (steps) in the channel sidewalls.

The final objective of the study was to calculate discharge through the channel. Discharge at site 1 was estimated at $110.34 \text{ m}^3 \text{ s}^{-1}$, and $55.77 \text{ m}^3 \text{ s}^{-1}$ at site 2. While it cannot be concluded from these data alone that the channel is the primary drainage pathway for the Milne Fiord epishelf lake, when compared with inflow estimates, the discharge volumes calculated for the channel in this study seem consistent with findings of previous investigators who suggest that the channel was the primary conduit for outflow from the epishelf lake. Based on hydrographic profiling of the 2009 fracture and minimum ice drafts along the channel, it was determined the ice shelf dam, or constriction point that controls outflow from the epishelf lake, was most likely located a few km seaward of the confluence of the fracture and channel. Outflow occurred along the entire length of the channel, exiting at the seaward edge of the ice shelf. These results contribute to an understanding of the dynamics of Milne Fiord and the processes operating at the base of the ice shelf.

This study provides the first confirmation of a basal channel under an ice shelf in the Canadian Arctic. The presence of a basal channel beneath an ice shelf decreases its stability. Thin ice along the length of the channel represents an area of weakness that makes the Milne Ice Shelf increasingly vulnerable to stresses. Channelization of epishelf lake outflow may have been an important factor in deglaciation along the northern coast of Ellesmere Island: observations suggest previous ice shelf breakup events in the

Canadian Arctic occurred along areas of thin ice formed by channelization. The Milne Ice Shelf may also be vulnerable to break up along thin ice in troughs between the ice shelf rolls, though more work is required to elucidate the extent and cause of thin ice in the troughs. Future breakup of the Milne Ice Shelf is likely to occur along the channel in the near future, resulting in the drainage of the last epishelf lake in the Northern Hemisphere.

Building on these results, the next step should be modelling the rate of incision of the ice shelf by epishelf lake outflow, in order to understand channel evolution. Detailed channel morphology, current speed and water temperature and salinity data from this study make it possible to model basal melt rates along the channel and estimate the incision rate of the ice shelf by epishelf lake outflow. Mass loss and runoff are projected to increase in the Canadian Arctic Archipelago in a warming climate (Gardner *et al.*, 2011; Lenaerts *et al.*, 2013). An increase in runoff input into the Milne Fiord epishelf lake will result in increased outflow and consequently, increased incision rates and a further reduction in ice thickness. An understanding of melt rates is therefore necessary to understand channel evolution and ice shelf stability in a warming climate.

There exist few direct measurements of water properties or current speed in ice shelf basal channels, due to the difficulty of accessing ice shelf cavities (e.g. Rignot and Steffen, 2008; Stanton *et al.*, 2013). Though the exact values are specific to the channel beneath the Milne Ice Shelf, in-situ observations from this study will contribute to an improved understanding of how the presence of basal channels can alter ice-shelf ocean interactions. Understanding controls on ice shelf stability is important because the collapse of ice shelves along the coasts of Greenland and Antarctica will result into greater flux of ice into the ocean from the continent, contributing to global sea-level rise.

Quantitative data from this study can be used to develop and validate models of ice ocean processes and, thus, better predictions about ice shelf stability and change in a warming climate.

7 References

- Alley, K.E., Scambos, T.A., Siegfried, M.R., and Fricker, H.A. (2016) Impacts of warm water on Antarctic ice shelf stability through basal channel formation. *Nature Geoscience*, 9: 290-293.
- Annan, A.P. (2009) Electromagnetic Principles of Ground Penetrating Radar. In Jol, H. ed. *Ground Penetrating Radar Theory and Applications*, Elsevier, Oxford, England.
- Antoniades, D., Francus, P., Pienitz, R., St-Onge, G., and Vincent, W.F. (2011) Holocene dynamics of the Arctic's largest ice shelf. *Proceedings of the National Academy of Sciences*. 108(47): 18899-18904.
- Arcone, S., Lawson, D., and Delaney, A. (1995) Short-pulse radar wavelet recovery and resolution of dielectric contrasts within englacial and basal ice of Matanuska Glacier, Alaska, U.S.A. *Journal of Glaciology*, 41(137): 68-86.
- Bauder, A., Funk, M., and Gudmundsson, G.H. (2003) The ice-thickness distribution of Unteraargletscher, Switzerland. *Annals of Glaciology*, 37: 331-336.
- Braun, C. Hardy, D.R., and Bradley, R.S. (2004) Surface mass balance of the Ward Hunt Ice Rise and Ward Hunt Ice Shelf, Ellesmere Island, Nunavut, Canada. *Journal of Geophysical Research*, 109(D22110).
- Cassidy, N.J. (2009) Ground penetrating radar data processing, modelling and analysis. In Jol, H. ed. *Ground Penetrating Radar Theory and Applications*, Elsevier, Oxford, England.

- Clark, T.S. and Bentley, C.R. (1994) High resolution radar on Ice Stream B2, Antarctica: measurements of electromagnetic wave speed in firn and strain history from buried crevasses. *Annals of Glaciology*, 20: 153-59.
- Copland, L., Mueller, D.R., and Weir, L. (2007) Rapid loss of the Ayles Ice Shelf, Ellesmere Island, Canada. *Geophysical Research Letters*, 34(L21501).
- Copland, L., Mortimer, C., White, A., Richer McCallum, M., and Mueller, D. (2017) Factors contributing to recent Arctic ice shelf losses. In Copland, L., and Mueller, D.R. eds. *Arctic Ice Shelves and Ice Islands*, Springer, Dordrecht, The Netherlands, in press.
- Cottier, F.R., Nilsen, F., Skogseth, R., Tverberg, V., Skardhamar, J. and Svendsen, H. (2010) Arctic fjords: a review of the oceanographic environment and dominant physical processes. In Howe, J.A., Austin, W.E.N., Forwick, M and Paetzel, M. eds. *Fjord Systems and Archives*, Special Publication, Geological Society, London, 344: 35-50.
- Crary, A.P. (1960) Arctic ice island and ice shelf studies, Part II. *Arctic*, 13: 32-50.
- Dowdeswell, J.A. (2017) Eurasian Arctic ice shelves and tidewater ice margins. In Copland, L., and Mueller, D.R. eds. *Arctic Ice Shelves and Ice Islands*, Springer, Dordrecht, The Netherlands, in press.
- Drewry, D.J., Jordan, S.R., and Jankowski, E.J. (1982) Measured properties of the Antarctic Ice Sheet: surface configuration, ice thickness, volume, and bedrock characteristics. *Annals of Glaciology*, 3: 83-91.

- Dutrieux, P., Vaughan, D.G., Corr, H.F.J., Jenkins, A., Holland, P.R., Joughan, I., and Fleming, A.H. (2013) Pine Island Glacier ice shelf melt distributed at kilometer scales. *The Cryosphere*, 7(5): 1543-1555.
- Dutrieux, P., Stewart, C., Jenkins, A., Nicholls, K.A., Corr, H.J., Rignot, E.R. and Steffen, K. (2014) Basal terraces on melting ice shelves. *Geophysical Research Letters*, 41: 5506-5513.
- England, J.H., Lakeman, T.R., Lemmen, D.S., Bednarksi, J.M., Stewart, T.G., and Evans, D.J.A. (2008) A millennial-scale record of Arctic Ocean sea ice variability and the demise of the Ellesmere Island ice shelves. *Geophysical Research Letters*, 35(L19502).
- Fisher, E., McMechan, G.A., and Annan, A.P. (1992) Acquisition and processing of wide-aperture ground-penetrating radar data. *Geophysics*, 57(3): 495-504.
- Gardner, A.S., Moholdt, G., Wouters, B., Wolken, G.J., Burgess, D.O., Sharp, M.J., Cogley, J.G., Braun, C., and Labine, C. (2011) Sharply increased mass loss from glaciers and ice caps in the Canadian Arctic Archipelago. *Nature*, 473(7347): 357-360.
- Gibson, J., and Andersen, D. (2002) Physical structure of epishelf lakes of the southern Bunger Hills, East Antarctica. *Antarctic Science*, 14(3): 253-261.
- Gladish, C.V., Holland, D.M., Holland, P.R. and Price, S.F. (2012) Ice-shelf basal channels in a coupled ice/ocean model. *Journal of Glaciology*, 58(212): 1227-1244.
- Hamilton, A.K. (2016) *Ice-Ocean Interactions in Milne Fiord*. PhD thesis, University of British Columbia, Vancouver, Canada. 151 pp.

- Hamilton, A.K., Laval, B.E., Mueller, D.R., Vincent, W.F. and Copland, L. (2017) Dynamic response of an Arctic epishelf lake to seasonal and long-term forcing: implications for ice shelf thickness. *The Cryosphere Discussion*, doi:10.5194/tc-2017-19.
- Hattersley-Smith, G. (1963) The Ward Hunt Ice Shelf: recent changes of the ice front. *Journal of Glaciology*, 4: 415-424.
- Holdsworth, G. (1971) Calving from Ward Hunt Ice Shelf, 1961-1962. *Canadian Journal of Earth Sciences*, 8(2): 299-305.
- Holdsworth, G., and Glynn, J. (1981) Iceberg calving from floating glaciers by a vibration mechanism. *Nature*, 274: 464-466.
- Holland, P.R., Jenkins, A., and Holland, D.M. (2008) The Response of ice shelf basal melting to variations in ocean temperature. *Journal of Climate*, 21: 2558-2572.
- Hubbard, B. and Glasser, N. (2005) *Field Techniques in Glaciology and Glacier Geomorphology*. John Wiley & Sons Ltd, West Sussex, England.
- Hughes Clarke, J.E., Dare, P., Beaudoin, J., and Bartlett, J. (2005) A stable vertical reference for bathymetric surveying and tidal analysis in the high Arctic. *U.S. Hydrographic Conference*, San Diego, California, USA. 16 pp.
- Humbert, A., Steinhage, D., Helm, V., Hoerz, S., Berendt, J., Leipprand, E., Christmann, J., Plate, C., and Muller, R. (2015) On the link between surface and basal structures of the Jelbart Ice Shelf, Antarctica. *Journal of Glaciology*, 61(229): 975-986.
- Jeffries, M. O. (1986) Glaciers and the morphology and structure of the Milne Ice Shelf, Ellesmere Island, N.W.T., Canada. *Arctic and Alpine Research*, 18(4): 397-405.

- Jeffries, M.O. (1991) Perennial water stratification and the role of basal freshwater flow in the mass balance of the Ward Hunt Ice Shelf, Canadian High Arctic. In Weller, G., Wilson, C.L. and Severin, B.A.B. eds. *Proceedings of the International Conference on the Role of Polar Regions in Global Change Vol 1*, Fairbanks, Alaska, USA: 332-337.
- Jeffries, M.O. (1992) Arctic ice shelves and ice islands: origin, growth and disintegration, physical characteristics, structural-stratigraphic variability and dynamics. *Reviews of Geophysics*, 30(3): 245-267.
- Jeffries, M.O. (2002) Ellesmere Island ice shelves and ice islands. In Williams, R.S. Jr and Ferrigno, J.G. eds. *Satellite Image Atlas of Glaciers of the World: Glaciers of North America*, U.S: Geological Survey Professional Paper 1386-J-1, Reston, VA, USA: 147-163.
- Jeffries, M.O. (2017) The Ellesmere ice shelves, Nunavut, Canada. In Copland, L., and Mueller, D.R. eds. *Arctic Ice Shelves and Ice Islands*, Springer, Dordrecht, The Netherlands, in press.
- Jeffries, M.O., and Sackinger, W.M. (1988) Water circulation and ice accretion beneath Ward Hunt Ice Shelf (Northern Ellesmere Island, Canada), deduced from salinity and isotope analysis of ice cores. *Annals of Glaciology*, 10: 68-72.
- Jenkins, A. (1991) A one-dimensional model of ice shelf-ocean interaction. *Journal of Geophysical Research: Oceans*, 96(C11): 20671-20677.
- Jenkins, A. (2011) Convection-driven melting near the grounding lines of ice shelves and tidewater glaciers. *Journal of Physical Oceanography*, 41(12): 2279-2294.
- Jungblut, A.D., Mueller, D.R., and Vincent, W.F. (2017) Arctic ice shelf ecosystems. In

- Copland, L., and Mueller, D.R. eds. *Arctic Ice Shelves and Ice Islands*, Springer, Dordrecht, The Netherlands, in press.
- Kelley, D. and Richards, C. (2016) *oce: Analysis of Oceanographic Data*. R package version 0.9-2.0. <http://CRAN.R-project.org/package=oce>.
- Keys, J.E., Johannssen, O., and Long, A. (1968) On the oceanography of Disraeli Fiord on Northern Ellesmere Island. *Marine Sciences Centre Manuscript Report 6*, McGill University, Montreal, Canada.
- Keys, J.E. (1978) Water regime of Disraeli Fiord, Ellesmere Island. *Technical Report 792, Defence Research Establishment, Ottawa, Canada*.
- Khazendar, A., and Jenkins, A. (2003) A model of marine ice formation within Antarctic ice shelf rifts. *Journal of Geophysical Research*, 108(C7): 3525.
- Langley, K., von Deschanden, A., Kohler, J., Sinisalo, A., Matsuoka, K., Hattermann, T., Humbert, A., Nost, O.A., and Isaksson, E. (2014) Complex network of channels beneath an Antarctic ice shelf. *Geophysical Research Letters*, 41(4): 1209-1215.
- Lawn, R. (1993) *Fracture of Brittle Solids*, 2nd ed. Cambridge University Press, Cambridge, England.
- Lazzara, M., Jezek, K., Scambo, T., MacAyeal, D., and Van der Veen, C. (1999) On the recent calving of icebergs from the Ross Ice Shelf. *Polar Geography*, 23: 201-212.
- Le Brocq, A., Ross, N., Griggs, J.A., Bingham, R.G., Corr, H.J., Ferraccioli, F., Jenkins, A., Jordan, T.A., Payne, A.J., Rippin, D.M. and Siegert, M.J. (2013) Evidence

- from ice shelves for channelized meltwater flow beneath the Antarctic Ice Sheet. *Nature Geoscience*, 6: 945-948.
- Lemmen, D.S., Evans, D.J. & England, J. (1988) Ice shelves of northern Ellesmere Island, NWT. *The Canadian Geographer*, 32: 363-367.
- Lenaerts, J., Angelen, J.H., Broeke, M.R., Gardner, A.S., Wouters, B., and Meijgaard, E. (2013) Irreversible mass loss of Canadian Arctic Archipelago glaciers. *Geophysical Research Letters*, 40(5): 870-874.
- Mankoff, K.D., Jacobs, S.S., Tulaczyk, S.M., and Stammerjohn, S.E. (2012) The role of Pine Island Glacier ice shelf basal channels in deep-water upwelling, polynyas and ocean circulation in Pine Island Bay, Antarctica. *Annals of Glaciology*, 53(60): 123-128.
- McDougall, T.J. and Barker, P.M. (2011) *Getting Started With TEOS-10 and the Gibbs Seawater (GSW) Oceanographic Toolbox*, SCOR/IAPSO WG127, ISBN 978-0-646-55621-5. 28 pp.
- McGrath, D., Steffen, K., Rajaram, H., Scambos, T., Abdalati, W., and Rignot, E. (2012) Basal crevasses on the Larsen C Ice Shelf, Antarctica: Implications for meltwater ponding and hydrofracture. *Geophysical Research Letters*, 39(L16504).
- Millgate, T., Holland, P.R., Jenkins, A., and Johnson, H.L. (2013) The effect of basal channels on oceanic ice-shelf melting. *Journal of Geophysical Research: Oceans*, 118: 6951-6964.
- Mingo, L., and Flowers, G.E. (2010) Instruments and methods: An integrated lightweight ice-penetrating radar system. *Journal of Glaciology*, 56(198): 709-714.

- Mortimer, C.A. (2011) *Quantification of Changes for the Milne Ice Shelf, Nunavut, Canada, 1950-2009*. MSc. thesis, University of Ottawa, Ottawa, Canada. 185 pp.
- Mortimer, C.A., Copland, L., and Mueller, D.R. (2012) Volume and area changes of the Milne Ice Shelf, Ellesmere Island, Nunavut, Canada, since 1950. *Journal of Geophysical Research*, 117(F04011).
- Mueller, D.R., Vincent, D.F., and Jeffries, M.O. (2003) Break-up of the largest Arctic ice shelf and associated loss of an epishelf lake. *Geophysical Research Letters*, 30(20): 1-4.
- Mueller, D.R., Vincent, W.F., and Jeffries, M.O. (2006) Environmental gradients, fragmented habitats and microbiota of a northern ice shelf cryoecosystem, Ellesmere Island, Canada. *Arctic, Antarctic and Alpine Research*, 38(4): 593-607.
- Mueller, D.R., Copland, L., Hamilton, A., and Stern, D. (2008) Ice shelf break-up and ecosystem loss in the Canadian High Arctic. *EOS*, 84(49): 548-552.
- Mueller, D.R., Crawford, A., Copland, L., and Van Wychen, W. (2013) Report to the Northern Transportation Assessment Initiative, Innovation Policy Branch, Transport Canada, Ottawa, Canada.
- Mueller, D.R., Copland, L., and Jeffries, M. (2017a) Changes in Canadian Arctic ice shelf extent since 1906. In Copland, L., and Mueller, D.R. eds. *Arctic Ice Shelves and Ice Islands*, Springer, Dordrecht, The Netherlands, in press.
- Mueller, D.R., Copland, L. and Jeffries, M.O. (2017b) Northern Ellesmere Island ice shelf and ice tongue extents, v 1.0 (1906-2015). *Nordicana* D28.

- Narod, B.B., Clarke, G.K.C., and Prager, B.T. (1988) Airborne UHF sounding of glaciers and ice shelves, northern Ellesmere Island, Arctic Canada. *Canadian Journal of Earth Sciences*, 25(1): 95-105.
- Navarro, F., and Eisen, O. (2010) Ground penetrating radar. In Pelikka, P and Rees, W. eds. *Remote Sensing of Glaciers: Techniques for Topographic, Spatial and Thematic Mapping of Glaciers*, CRC press/Balkema, Leiden, The Netherlands.
- Overland, J., Key, J., Hanna, E., Hanssen-Bauer, B-M., Kim, S-J., Walsh, J., Wang, M., Bhatt, U., Liu, Y., Stone, R., Cox, C., and Walden, V. (2014) The Arctic. The lower atmosphere: air temperature, clouds and surface radiation. In: "State of the Climate 2014". *Bulletin of the American Meteorological Society*, 95(7): S115-S117.
- Plewes, L.A. and Hubbard, B. (2001) A review of the use of radio-echo sounding in glaciology. *Progress in Physical Geography*, 25(2): 203-236.
- RD Instruments (2011) *Acoustic Doppler Current Profiler Principles of Operation: A Practical Primer*. Teledyne RD Instruments Inc., Poway, California, USA.
- Richer McCallum, M. (2015) *Analysis of Ice Types Along the Northern Coast of Ellesmere Island, Nunavut, Canada and Their Relationship to Synthetic Aperture Radar (SAR) Backscatter*. MSc. thesis, Carleton University, Ottawa, Canada. 147 pp.
- Rignot, E., and Steffen, K. (2008) Channelized bottom melting and stability of floating ice shelves. *Geophysical Research Letters*, 35(L02503).
- Scambos, T., Hulbe, C., and Fahnestock, M. (2003) Climate-induced ice shelf disintegration in the Antarctic Peninsula. *Antarctic Research Series*, 79: 79-92.

- Sergienko, O.V. (2013) Basal channels on ice shelves. *Journal of Geophysical Research: Earth Surface*, 118: 1342-1355.
- Stanton, T.P., Shaw, W.J., Truffer, M., Corr, H.F.J., Peters, L.E., Riverman, K.L., Bindschadler, R., Holland, D.M., and Anandakrishnan, S. (2013) Channelized ice melting in the ocean boundary layer beneath Pine Island Glacier, Antarctica. *Science*, 341: 1236-1239.
- Stroeve, J.C., Serreze, M.C., Holland, M.M., Kay, J.E., Malanik, J., and Barrett, A. (2012) The Arctic's rapidly shrinking sea ice cover: a research synthesis. *Climatic Change*, 110: 1105-1027.
- Vaughan, D.G., Corr, H.F.J., Bindschadler, R.A., Dutrieux, P., Gundmundsson, G.H., Jenkins, A., Newman, T., Vornberger, P., and Wingham, D.J. (2012) Subglacial melt channels and fracture in the floating part of Pine Island Glacier, Antarctica. *Journal of Geophysical Research: Earth Surface*, 117(F03012).
- Veillette, J., Mueller, D.R., Antoniades, D., and Vincent, W.F. (2008) Arctic epishelf lakes as sentinel ecosystems: Past, present and future. *Journal of Geophysical Research: Biogeosciences*, 113(G04014).
- Veillette, J., Lovejoy, C., Potvin, M., Harding, T., Jungblut, A.D., Antoniades, D., Chenard, C., Suttle, C.A., and Vincent, W.F. (2011) Milne Fiord epishelf lake: a coastal Arctic ecosystem vulnerable to climate change. *Ecoscience*, 18(3): 304-316.
- Vincent, W.F., Gibson, J.A.E., Pienitz, R., and Villeneuve, V. (2000) Ice shelf microbial ecosystems in the High Arctic and implications for life on snowball Earth. *Naturwissenschaften*, 87: 137-141.

- Vincent, W. F., Gibson, J.A.E., and Jeffries, M.O. (2001) Ice shelf collapse, climate change, and habitat loss in the Canadian high Arctic. *Polar Record*, 37(201): 133–142.
- Vincent, W.F., Whyte, L.G., Lovejoy, C., Greer, C.W., Laurion, I., Suttle, C.A., Corbeil, J., and Mueller, D.R. (2009) Arctic microbial ecosystems and impacts of extreme warming during the International Polar Year. *Polar Science*, 3(3): 171-180.
- Vincent, W.F., Fortier, D., Levesque, E., Boulanger-Lapointe, N., Tremblay, B., Sarrazin, D., Antoniadis, D., and Mueller, D.R. (2011) Extreme ecosystems and geosystems in the Canadian High Arctic: Ward Hunt Island and vicinity. *Ecoscience*, 18(3): 236-261.
- Welch, B.C., Pfeffer, W.T., Harper, J.T., and Humphrey, N.F. (1998) Mapping subglacial surface of temperate valley glaciers by two-pass migration of a radio-echo sounding survey. *Journal of Glaciology*, 44(146): 164-170.
- White, A., Copland, L., Mueller, D., and Van Wychen, W. (2015). Assessment of historical changes (1959-2012) and the causes of recent break-ups of the Petersen Ice Shelf, Nunavut, Canada. *Annals of Glaciology*, 56(69): 65-76.
- Wilson, N. (2013) *Radar Tools* (software). <http://doi.org/10.5281/zenodo.43972>

Appendix A: Cross-sectional ice thickness profiles from IPR survey grids

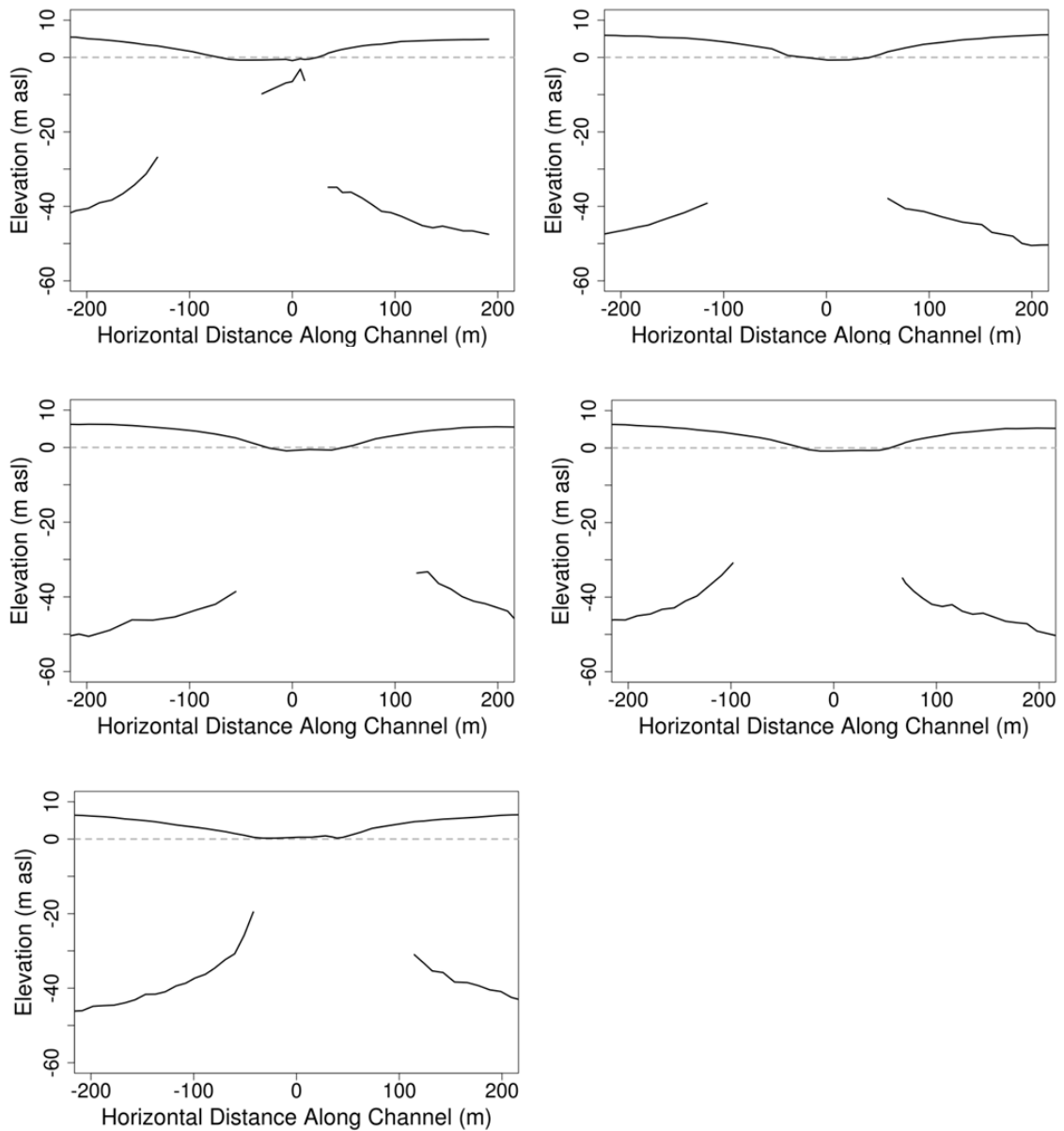


Figure A1 Cross-sectional ice thickness profiles from grid A in the channel, used in the calculation of metrics in Table 4.2 but not shown in Figure 4.4. Channel profiles run from the left (negative) to right (positive) where the left is defined in the downstream direction and zero corresponds to the centerline defined along the channel at the surface of the ice shelf. The dashed grey line indicates sea level (0 m asl).

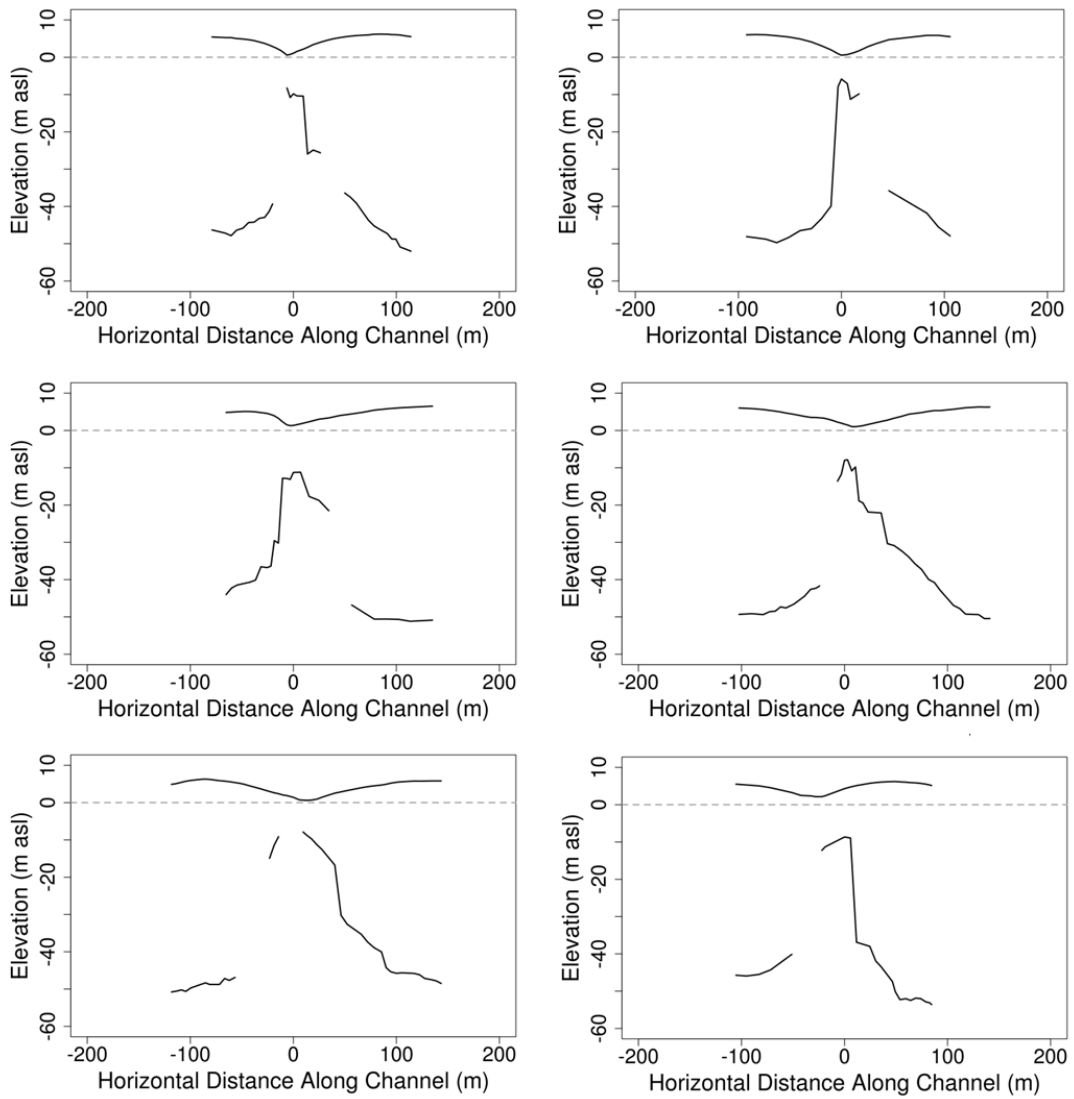


Figure A2 Cross-sectional ice thickness profiles from grid B in the channel, used in the calculation of metrics in Table 4.2 but not shown in Figure 4.4. Channel profiles run from the left (negative) to right (positive) where the left is defined in the downstream direction and zero corresponds to the centerline defined along the channel at the surface of the ice shelf. The dashed grey line indicates sea level (0 m asl).

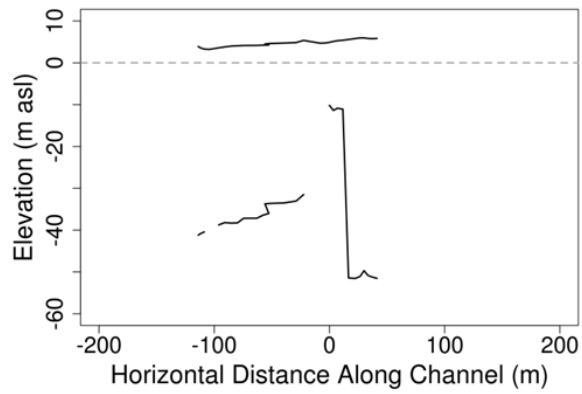


Figure A3 Cross-sectional ice thickness profile from grid C in the channel, used in the calculation of metrics in Table 4.2 but not shown in Figure 4.4. Channel profiles run from the left (negative) to right (positive) where the left is defined in the downstream direction and zero corresponds to the centerline defined along the channel at the surface of the ice shelf. The dashed grey line indicates sea level (0 m asl).

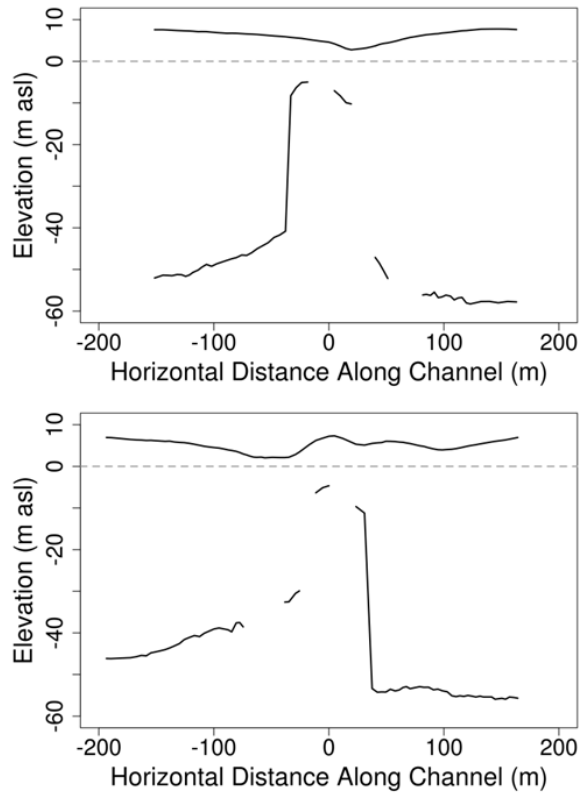


Figure A4 Cross-sectional ice thickness profiles from grid D in the channel, used in the calculation of metrics in Table 4.2 but not shown in Figure 4.4. Channel profiles run from the left (negative) to right (positive) where the left is defined in the downstream direction and zero corresponds to the centerline defined along the channel at the surface of the ice shelf. The dashed grey line indicates sea level (0 m asl).

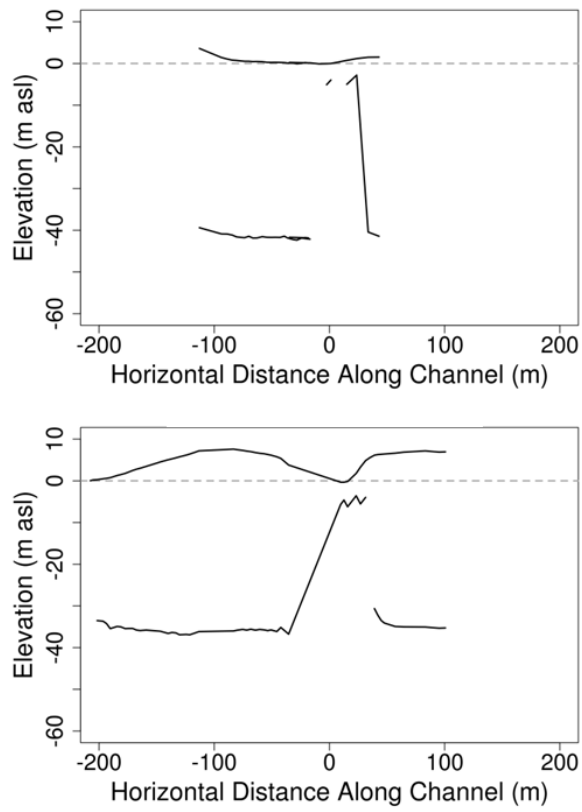


Figure A5 Cross-sectional ice thickness profiles from grid E (the fracture) used in the calculation of metrics in Table 4.2 but not shown in Figure 4.4. Fracture profiles run from north (negative) to south (positive) across the fracture; zero corresponds to the fracture centerline. The dashed grey line indicates sea level (0 m asl).